2012

Simulation of a Capacitive Micromachined Ultrasonic Transducer with a Parylene Membrane and Graphene Electrodes

David Sadat
University of Central Florida

STARS Citation

Showcase of Text, Archives, Research & Scholarship

SIMULATION OF A CAPACITIVE MICROMACHINED ULTRASONIC
TRANSDUCER WITH A PARYLENE MEMBRANE AND GRAPHENE
ELECTRODES

by

DAVID SADAT
B.S. University of Central Florida, 2009

A thesis submitted in partial fulfillment of the requirements
for the degree of Masters of Science in Mechanical Engineering
in the Department of Mechanical, Materials, and Aerospace Engineering
in the College of Engineering and Computer Science
at the University of Central Florida
Orlando, Florida

Spring Term
2012

ABSTRACT

Medical ultrasound technology accounts for over half of all imaging tests performed worldwide. In comparison to other methods, ultrasonic imaging is more portable and lower costing, and is becoming more accessible to remote regions where traditionally no medical imaging can be done. However, conventional ultrasonic imaging systems still rely on expensive PZT-based ultrasound probes that limit broader applications. In addition, the resolution of PZT based transducers is low due to the limitation in hand-fabrication methods of the piezoelectric ceramics.

Capacitive Micromachined Ultrasonic Transducers (CMUTs) appears as an alternative to the piezoelectric (PZT) ceramic based transducer for ultrasound medical imaging. CMUTs show better ultrasound transducer design for batch fabrication, higher axial resolution of images, lower fabrication costs of the elements, ease of fabricating large arrays of cells using MEMS fabrication, and the extremely important potential to monolithically integrate the 2D transducer arrays directly with IC circuits for real-time 3D imaging.

Currently most efforts on CMUTs are silicon based. Problems with current silicon-based CMUT designs include low pressure transmission and high-temperature fabrication processes. The pressure output from the silicon based CMUTs cells during transmission are too low when compared to commercially available PZT transducers, resulting in relatively blurry ultrasound images. The fabrication of the silicon-based cells, although easier than PZT transducers, still suffers from inevitable high temperature process and require specialized and expensive equipment. Manufacturing at an elevated temperature hinders the capability of fabricating

front end analog processing IC circuits, thus it is difficult to achieve true 3D/4D imaging.

Therefore novel low temperature fabrication with a low cost nature is needed.

A polymer (Parylene) based CMUTs transducer has been investigated recently at UCF
and aims to overcome limitations posted from the silicon based counterparts. This thesis
describes the numerical simulation work and proposed fabrication steps of the Parylene based
CMUT. The issue of transducer cost and pressure transmission is addressed by proposing the
use of low cost and low temperature Chemical Vapor Deposition (CVD) fabrication of Parylene-
C as the structural membrane plus graphene for the membrane electrodes. This study focuses
mainly on comparing traditional silicon-based CMUT designs against the Parylene-C/Graphene
CMUT based transducer, by using MEMS modules in COMSOL. For a fair comparison, single
CMUT cells are modeled and held at a constant diameter and the similar operational frequency
at the structural center. The numerical CMUT model is characterized for: collapse voltage,
membrane deflection profile, center frequency, peak output pressure transmission over the
membrane surface, and the sensitivity to the change in electrode surface charge. This study
took the unique approaches in defining sensitivity of the CMUT by calculating the membrane
response and the change in the electrode surface charge due to an incoming pressure wave.
Optimal design has been achieved based on the simulation results. In comparison to silicon
based CMUTs, the Parylene/Graphene based CMUT transducer produces 55% more in volume
displacement and more than 35% in pressure output. The thesis has also laid out the detailed
fabrication processes of the Parylene/Graphene based CMUT transducers. Parylene/Graphene

based ultrasonic transducers can find wide applications in both medical imaging and Non-

destructive evaluation (NDE).

TABLE OF CONTENTS

LIST OF FIGURES

LIST OF TABLES

LIST OF ACRONYMS/ABBREVIATIONS

CMUT   Capacitive Micromachined Ultrasonic Transducer

CVD   Chemical Vapor Deposition

PVD   Physical Vapor Deposition

Pa   Pascals (Units)

TGC   Time-Gain Control

CHAPTER ONE:
INTRODUCTION

Capacitive Micromachined Ultrasonic Transducers (CMUTs) are a relatively new and undeveloped technology in the ultrasound imaging field [1], [2]. The interest over the past few years is due to CMUTs exhibiting many benefits over the conventional PZT ceramic transducer, including: lower fabrication cost, better acoustic matching into the propagation medium, a wider fractional bandwidth, higher axial resolution for imaging relatively smaller targets [3], non-contact probe operation (no need for matching impedance layers), ease of fabricating large arrays, and the potential to monolithically integrate the transducers to IC circuits for signal processing prior to connecting to a computer via cable for 3D imaging [4]. There is much research in ultrasound towards real-time 3D volumetric imaging [5] [6], however ultrasound imaging in 3D is difficult due to current technological constraints, including both the transducer cell size miniaturization limits of piezoelectrics ceramics, and the overwhelming number of electrical interconnects that such an array of cells would require. The ultrasound probe can greatly benefit from the help of the closely integrated signal processing circuits to handle the overwhelming number of elements and interconnects required for 3D imaging. Aside from 3D medical imaging, there is interest in the CMUT for invasive procedures [7]. Due to the fact that the CMUT has evolved from micromachining techniques and utilize Microelectromechanical Systems (MEMS) technologies, it is therefore compatible with IC fabrication and can thus be implemented monolithically CMOS circuitry.

Although there are many benefits to the CMUT, there also numerous problems that hinder the performance relative to current PZT-based ultrasound technologies. These include: high-temperature and very specialized fabrication steps [8], and low transmission pressure output that results in "fuzzy" images [9].

Several attempts over the years have been made to combat these problems associated with performance, including a collapse-snapback bias voltage mode of operation [10], using dual electrodes inside of the CMUT membrane [11], and using a flexible polymer (SU-8) membrane [12]. All of these methods ultimately try to achieve a higher pressure output, each has their own flaw.

The objective of this study was to investigate the differences between traditional CMUTs fabricated from silicon or silicon nitride membranes versus CMUTs fabricated from polymer (parylene-C) membranes using the novel idea of ultra-thin but stiff graphene layers for the upper electrode. Parylene-C is conventionally used as a final layer to "seal" electronic devices from moisture, and there have also been studies that demonstrate parylene-C as a final sealant to the CMUT arrays to simply protect from the outside environment and as a biocompatible coating [13]. Very few studies have explored a polymer material for the membrane, and none have used parylene-C as membrane material. Typically CMUTs use an aluminum electrode deposited at a thickness of around 0.2 μm. However, in order to preserve the flexibility of the softer parylene-C membrane, the novel idea of using ultra-thin graphene layers (0.3 nm per layer) is investigated as a viable option in this study. Overall the fabrication

process for this newly proposed device is relatively easier to perform, conducted at room temperature, and less expensive in cost when compared to silicon nitride CMUT membranes or PZT-based transducers.

To study the CMUT, numerical simulation models were developed using the commercially available software COMSOL Multiphysics 4.2. A model was built that encompassed pressure acoustics of the surrounding medium (air or oil), MEMS Solid Mechanics for the micron-range mechanics of the cell structure, electrostatics to account for the voltage input and capacitance between the two electrodes, and a Moving Mesh to accurately calculate the position of the membrane relatively to a voltage input and surrounding medium conditions (i.e. fluid damping of the membrane in dynamic motion).

The model was solved to demonstrate various CMUT characteristics of interest, including: collapse voltage of the structure, deflection profile of the membrane, center frequency during operation, a frequency sweep of peak-to-peak output pressures over the surface of the CMUT membrane, and capacitance change (sensitivity) between the two electrodes. This study takes the unique approach in using Finite Element Analysis (FEA) simulation to investigating CMUT sensitivity by calculating the membrane response and capacitance change due to an incoming transient pressure wave. In dynamic analysis, the main difference between silicon/silicon nitride-based membrane and the Parylene-C/Graphene-based membrane was that the parylene-C material had a Young's Modulus of one order of magnitude lower than silicon, and the Parylene-C and Graphene material were modeled as

3

having a very high poisson's ratio relative to silicon. This leads to differences in maximum transient deflection of the membranes prior to substrate collapse.

For 7 MHz CMUT cells with a collapse voltage of 130V and an AC voltage of 15V biased at 80% of the collapse voltage, FEA calculations show that the Parylene-C/Graphene CMUT exhibits a larger pressure output of 376 kPa, while the traditional silicon membrane only exhibits 250 kPa of peak-to-peak pressure output. This is an increase of 20% in peak-to-peak output pressure. For the same CMUT cell biased at 60% of the collapse voltage with a superimposed AC voltage of 40V, the parylene-C/Graphene CMUT exhibits a much larger peak-to-peak pressure output of 654 kPa, while the Silicon membrane operating with the same exact parameters can only output 410 kPa. This shows a 59% increase in peak-to-peak output pressure.

CHAPTER TWO:
LITERATURE REVIEW

Ultrasound Background

Sound is defined as mechanical energy transmitted by pressure waves through a particular medium [14]. Sound carries energy that causes, for example, air molecules in the path of the pressure wave to be displaced or disturbed in a back and forth motion. There are different categories for sound, and all of these categories vary according to the frequency of the wave. These categories include infrasound below 20 Hz, the acoustic range between 20 Hz – 20 kHz, and ultrasound waves at above 20 kHz. Frequency is noted in units of Hertz (Hz), which is defined as the rate of occurrence of a certain event per unit of time. For ultrasound imaging, the frequency required is typically above 1 MHz. Figure 1 below illustrates the frequency criteria for various sound categories and their associated applications.
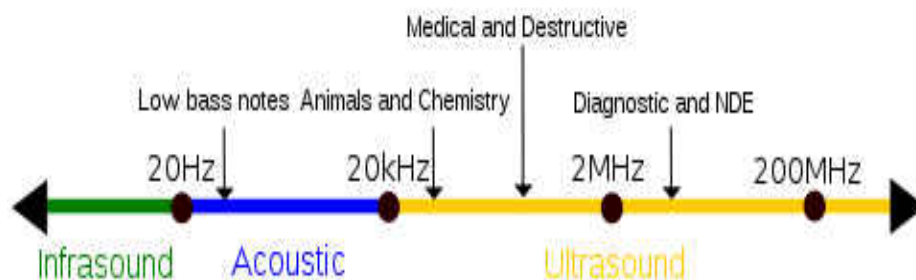
Figure 1: Sound category according to frequency [15]

The strength of the sound wave is quantified by the acoustic pressure [16], often noted in units of Pascals (Pa). In a wave at a given point, the pressure may oscillate between higher pressure regions and lower pressure regions. This is due to disturbance of surrounding molecules in the medium, and can be best visualized as a ripple pattern, shown in Figure 2. For ultrasound imaging, the transducer can typically achieve a maximum pressure output of 1 MPa [17].
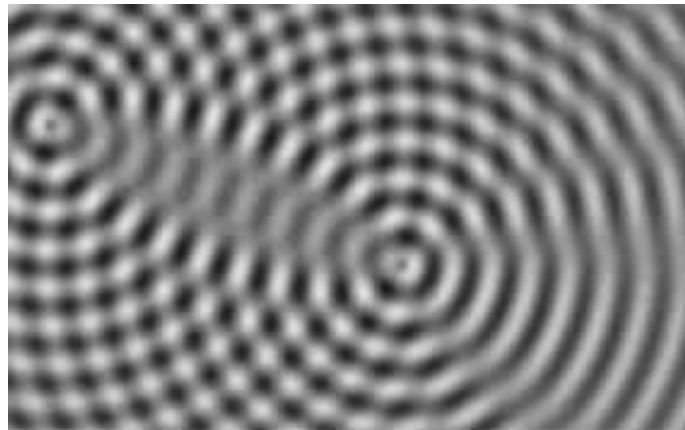
Figure 2: Pressure wave oscillating from a central point, generated in COMSOL Multiphysics

As the sound wave travels, the molecules in the medium are disturbed by vibrational energy. This produces the back-and-forth displacement of the molecules that squeezes and pulls on the nearby molecules. As illustrated in Figure 3, regions in which molecules are pushed together are called compression areas, and regions where molecules are less densely spaced apart are called rarefaction regions [17].
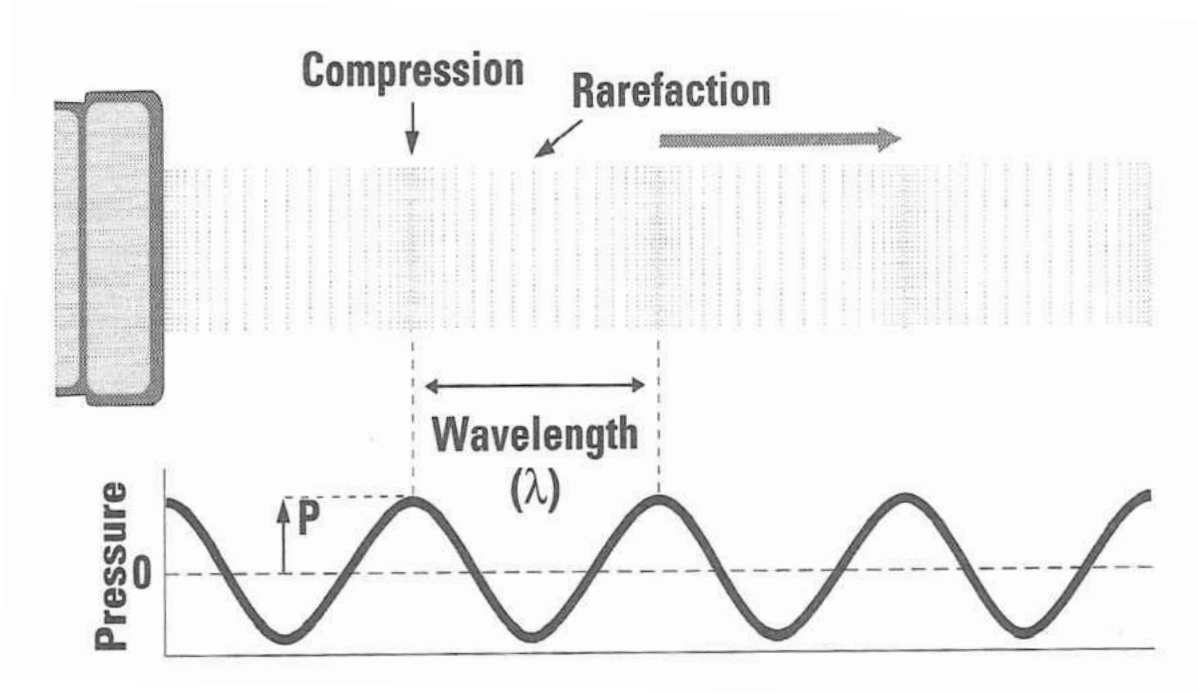
Figure 3: Compression and Rarefaction of a sound wave [17].

A particularly important characteristic of ultrasound is the attenuation of the pressure as the wave travels through the medium, for example the human body. One cause of attenuation is reflection and scattering at the interfaces in tissue, and another is absorption in which acoustic energy is converted to heat energy. During attenuation the amplitude and intensity of the wave is reduced as a function of distance. This quantity can be summarized by the attenuation coefficient, where the degree of pressure wave attenuation in a tissue is quantified in decibels per centimeters (dB/cm). Table 1 below demonstrates the attenuation coefficients for various human tissues at 1 MHz.

Table 1: Attenuation coefficients for various human tissues at 1 MHz [17]

Tissue	Attenuation at 1 MHz
Water	0.0002 (dB/cm)
Blood	0.18 (dB/cm)
Liver	0.5 (dB/cm)
Muscle	1.2 (dB/cm)
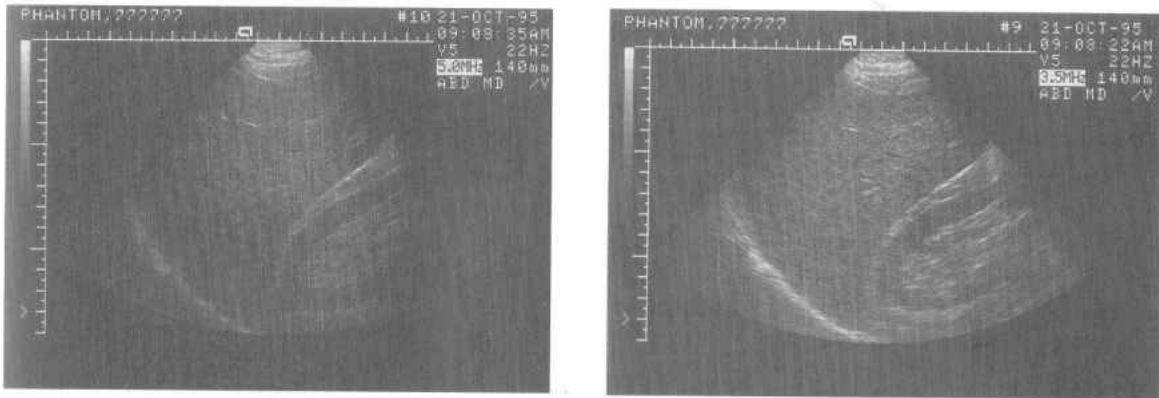
Figure 4: Liver imaged at (A) 5 MHz vs (B) 3 MHz [17]

Attenuation is largely dependent on the frequency of the wave, and in most cases attenuation is virtually proportional to the frequency, thus the higher the frequency of the ultrasound wave the larger the attenuation coefficient. Lower frequencies exhibit less attenuation, however at the cost of having a lower resolution. Likewise higher frequencies

exhibit more attenuation, yet at the benefit of having a better resolution. Figure 4 above demonstrates the consequence of high frequency imaging for relatively deep targets.

PZT-based Ultrasound Transducer

The advent of modern PZT-based ultrasound transducers can be traced back to numerous separate technological advances within the past century, including [18]: the discovery of piezoelectricity, vacuum tube amplifiers, Cathode Ray Tube (CRT) monitors, ferroelectrics, transistors, integrated circuits, microelectronic fabrication technologies, and microprocessors for advanced computing. Most current commercially available ultrasound technologies rely on transducers that exhibit the piezoelectric effect to generate sound waves and detect incoming signals. This piezoelectric effect was first discovered in the 1880s by the Curie brothers. It was noted that when a crystal material underwent a mechanical stress applied to its face, an electric charge resulted. Conversely in 1881 Gabriel Lippman discovered the opposite effect; if an electric signal was applied, the crystal would vibrate and produce ultrasound. Figure 5 below illustrates the piezoelectric concept.
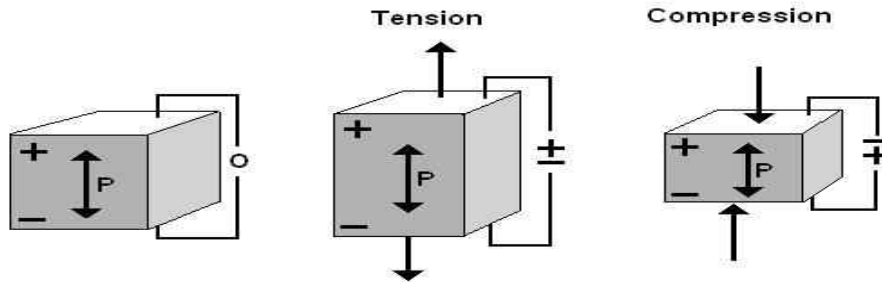
Figure 5: Piezoelectric effect on crystals [19]

Piezoelectricity came into greater use around the time of World War I as a means for detecting submarines using SONAR. Chilowsky and Langevin developed a quartz crystal based detector that was capable of detecting the distance of other ships based on the amount of time the signal had taken to echo back to the receiver [18], similar to echo-location that bats or dolphins use in nature.

During World War II, Russia, Japan, and the United States engaged in research in ferroelectrics as a means to improve upon the piezoelectric material properties. It was soon discovered that certain ceramic materials produced dielectric constants up to 100 times higher than previously-used piezoelectric crystals [18]. The significance was that this newer ceramic material had a much greater performance in terms of sensitivity to input voltage or an incoming wave, which would eventually be put to use as the current standard for ultrasound medical imaging transducers.

Figure 6: Modern Ultrasound Imaging station located at the UCF Medical School. Cart-based system (left) and portable laptop ultrasound probe (right).

In modern ultrasound probes the active element, a lead zirconate titanate (PZT) ceramic, is situated between the damping backing material and the matching layer. Figure 7 below shows a sketch of this concept. The piezoelectric ceramic has a center frequency around which it is most effective at converting electrical energy into acoustic energy via dynamic

motion, and vice versa. The center frequency is determined by the thickness of the element. Thinner elements have a higher center frequency, while thicker elements have lower center frequencies.
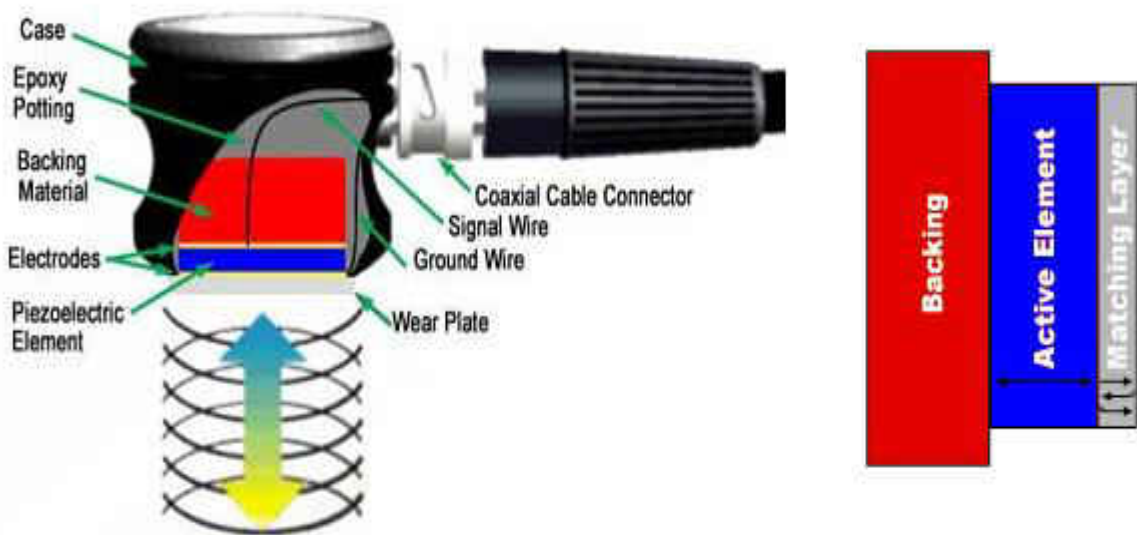
Figure 7: Piezoelectric probe (left) and the active element (right) with backing and matched layer [20]

The backing material on the probe serves the purpose of reducing the "vibration" of the PZT ceramic element, also known as ringing [21]. When the element is initially excited by a short pulse of electrical energy, it converts the electrical energy into acoustic energy in the form of dynamic motion of the ceramic or crystal. This motion of the element surface sends a pulse of sound into the air medium. After the initial pulse excitation, the element continues to

vibrate. In transducer design, it is most beneficial to have a probe that sends out as short of an ultrasound pulse as possible [22]. Hence, this is the major purpose for the damping backing on the ultrasound probe.

The matching layer in front of the piezoelectric element facilitates acoustic coupling from the element to the object's medium. In the case of medical ultrasound, some sort of gel is applied on a human patient instead. This matching layer facilitates acoustic coupling between the active element and the target of interest [22].

After a pulse strikes the target and produces an echo, the echo signals are received by the ultrasound probe and displayed on the monitor. For a 2D ultrasound image, the grayscale shading of a particular point is dictated by the intensity of the incoming wave. For example, bone reflects nearly most of the ultrasound pulse back towards the transducer, and thus corresponds to a very bright white color on screen. Another consideration in forming a 2D ultrasound image on-screen is the time required for an echo to travel back towards the transducer. This time duration for the echo to travel back determines the depth of the feature.
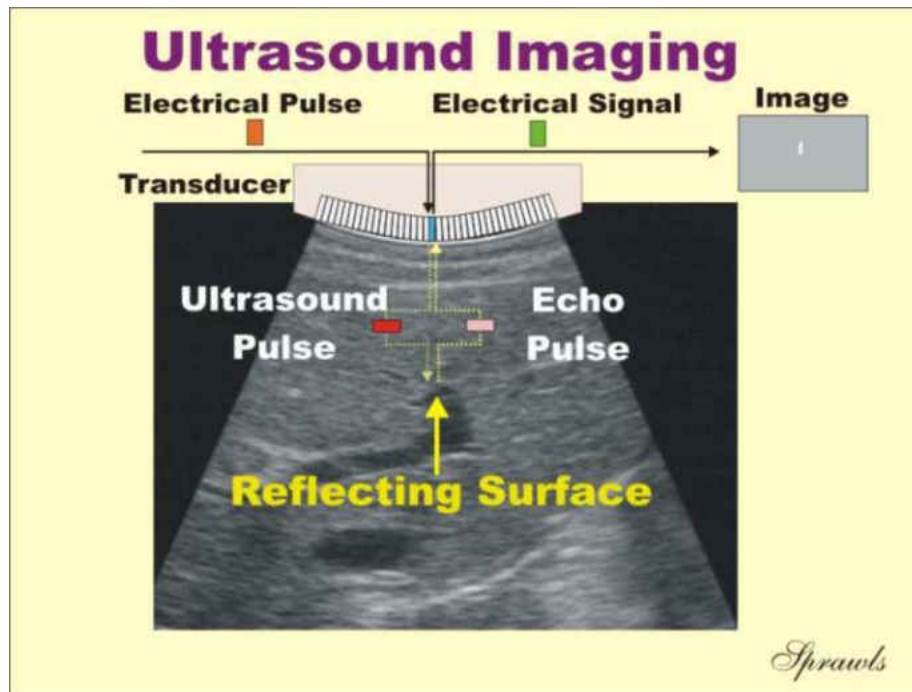
Figure 8: Ultrasound image grayscale shading is determined by the intensity of the wave that has bounced off from the reflected surface [23].

Most of the sound wave will strike a target and bounce back, yet some ultrasound intensity travels through the target and continues forward. For the latter wave, upon bouncing off of the next target and then traveling back towards the transducer the intensity of the incoming wave has been severely reduced. To compensate for this, the weaker echoes are amplified by raising the gain of the receiver [22]. The gain is the ratio of output signal amplitude to the input signal amplitude. Since the weaker echoes will be traveling from deeper depths inside the object, the wave will take a longer time to travel back towards the receiver. Using this information is beneficial because the receiver gain may be ramped up at a slope,

according to time. This is called Time Gain Control, or TGC. Figure 10 demonstrates the

concept.
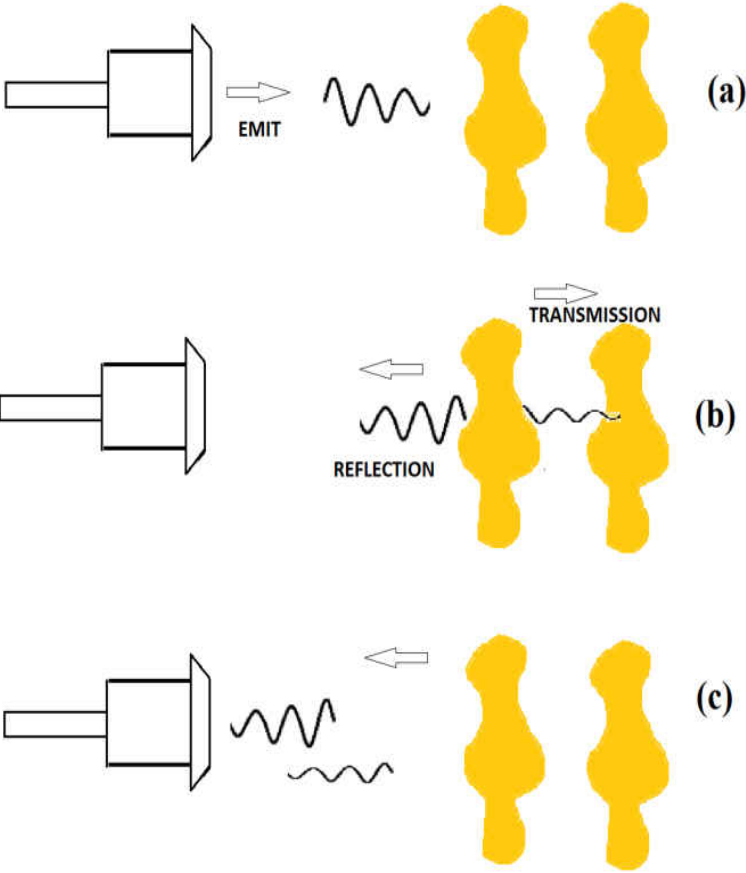
Figure 9: Ultrasound (a) launched from transducer, (b) reflected or transmitted through structure, and (c) both waves coming back together due to poor axial resolution.
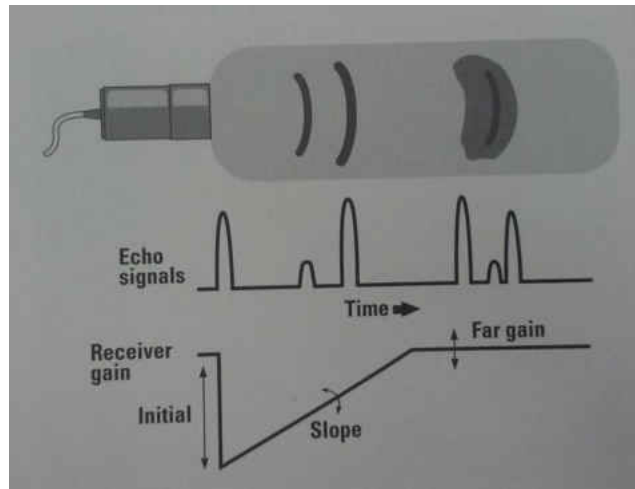
Figure 10: Time-gain control (TGC) of ultrasoun probe [17].
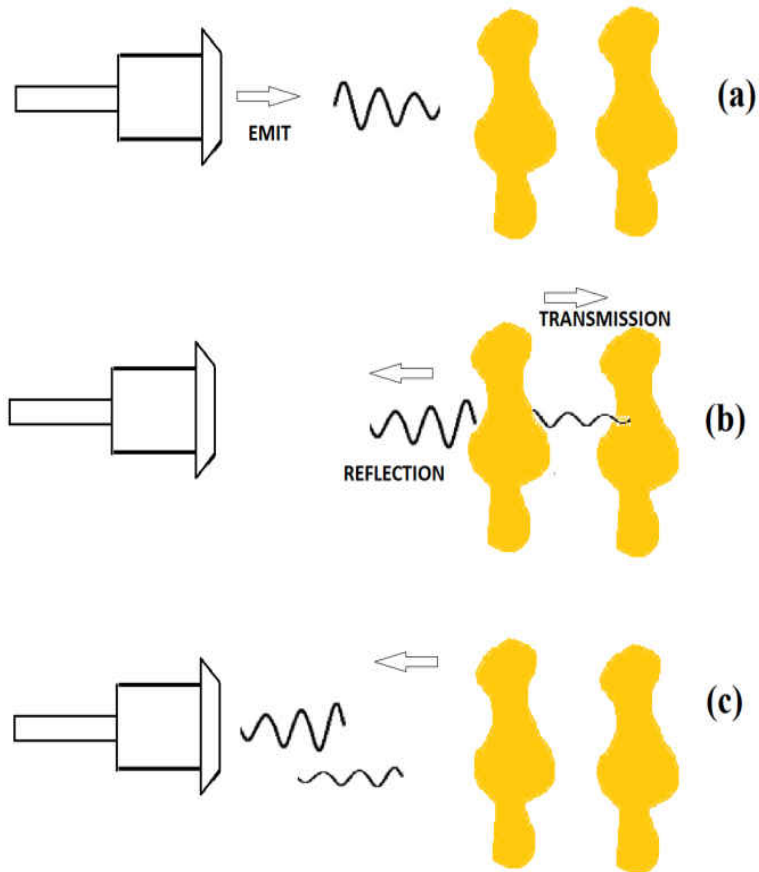
Figure 9 above demonstrates the differences between a shorter pulse versus a larger pulse. The reasoning behind using a shorter pulse is that a higher axial resolution may be obtained, where axial resolution is defined by the minimum spacing between ultrasound echoes that may be distinguished. Two features that are located in close proximity to each other might not be accurately distinguished if the time-length of the pulse is greater than the length between the two features. This is because the echo reflections bouncing off of both features will travel and reach the receiving probe simultaneously, thus there is absolutely no way the transducer can distinguish between the distance of one structure versus the other. Figure 9(c) demonstrates the how the length of the pulse determines the axial resolution, as both waves arrive at the transducer at the same time.

On the same note, the time-pulse duration in the piezoelectric-based ultrasound probe is also associated with bandwidth. A transducer that exhibits a longer pulse will, upon performing spectral analysis of the original time-amplitude signal, have a narrower bandwidth. Likewise a pulse with a shorter duration exhibits a relatively wider bandwidth, as shown in Figure 11.
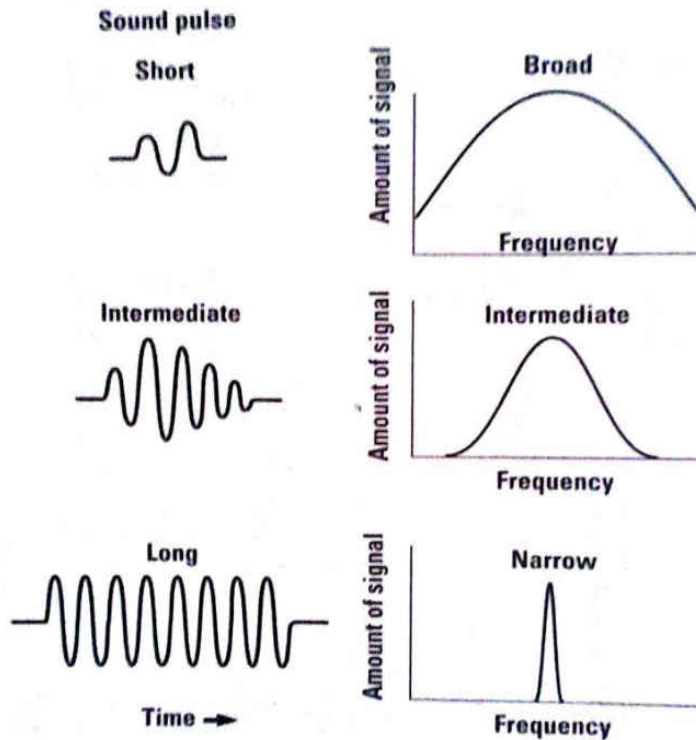
Figure 11: Time-transient sound pulse and the corresponding acoustic-frequency [17]

As mentioned previously it was noted that the backing material for the active element piezoelectric was used to reduce the ringing of the ceramic. It is normally desirable to design a probe that can operate efficiently over a larger range of frequencies. This is referred to as a broad bandwidth design [24]. The benefit to a broad bandwidth design is that the probe can be efficient in a wide variety of clinical applications.

Lastly, another merit of the piezoelectric probe operation is PZT's ability to transmit an amplitude of pressure from its surface, which is another way of describing the intensity of the sound wave. Aside from frequency contained in the sound wave, the intensity of the pressure

output amplitude is very important because it, upon bouncing off of a target at a certain depth, will directly determine the dynamic grayscale shading of the target [17]. This is due to the fact that there will be more pressure available to either bounce off the target or penetrate through the target to continue in deeper in the same axial direction. The transducer in receive mode acts as a sensor, and a higher original pressure output enables a larger sound wave to bounce off a target. Thus, there is more sensitivity to distinguish regions of the 2D ultrasound image with a different shade.

Figure 12: Image of relatively low pressure output (left) and higher pressure output (right) [17]

Problems with PZT-based Ultrasound Transducers

One major disadvantage of the PZT based ultrasound transducer is the acoustic impedance mismatch between the element and medium [14], as this mismatch is almost 20 times higher than that of soft tissue or air. Hence, if a matching layer or gel was not used to

facilitate the acoustic propagation between the probe and human, a large fraction of the ultrasound wave's power would be reflected at the PZT-tissue interface [17]. There would be less pressure transmitted into the target. This leads to less sound pressure to bounce off targets and ultimately less sensitivity for gray scale shading of that particular point.
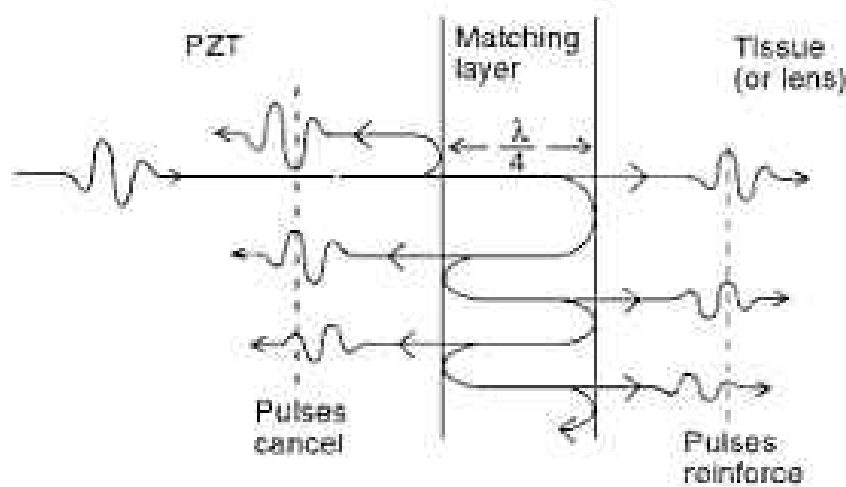
Figure 13: PZT with matching layer produces longer pulse [17]

A matching layer/gel is, therefore, commonly used when performing ultrasound imaging with PZT transducers. The main downside to the use of the matching layer is that the range of useful frequencies in which there is one hundred percent efficient conversion between electrical input and pressure output is extremely narrowed to one major frequency [25]. In order for the matching layer to achieve the acoustic matching as well as one hundred percent efficiency at a certain frequency, the matching layer should have a thickness equal to one

quarter the thickness of the wavelength. Also, the matching layer should have an impedance

equal to

$$\sqrt{Z_{PZT} * Z_{target}},$$

where Z_{PZT} is the impedance of the PZT material and Z_{target} is the impedance of the target. As

Figure 13 above demonstrates, sound pressure waves from the PZT element reverberate

repeatedly inside the matching layer. The repetition of waves inside the matching layer gives a

larger total pulse into the target, which facilitates acoustic matching between the active

element and the target.

Another major problem is the fabrication using PZT elements becomes costly and labor

intensive. This is because the element must be mechanically diced by hand. It becomes hard to

manufacture transducers with elements past 200 um, thus the resolution of the transducer

probe is limited to the lower end of the ultrasound medical imaging range.
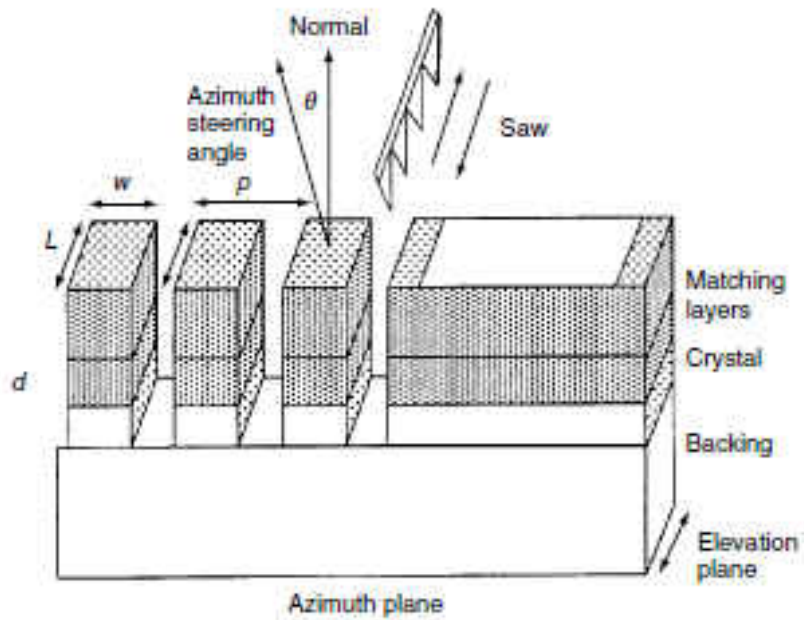
Figure 14: Mechanical dicing/saw of PZT elements [18]

Size constraints are a big limitation in manufacturing the PZT elements into 2D arrays, which are needed for 3D/4D imaging. Although conventional 1D transducer arrays may produce 3D images by being rotated and reconstructed via post-processing, a live image or an image that only requires one position in order to acquire a 3-dimensional image is not easily possible. Figure 15 below demonstrates the difference between linear scanning with a 1D array versus full 3D imaging with a 2D array.
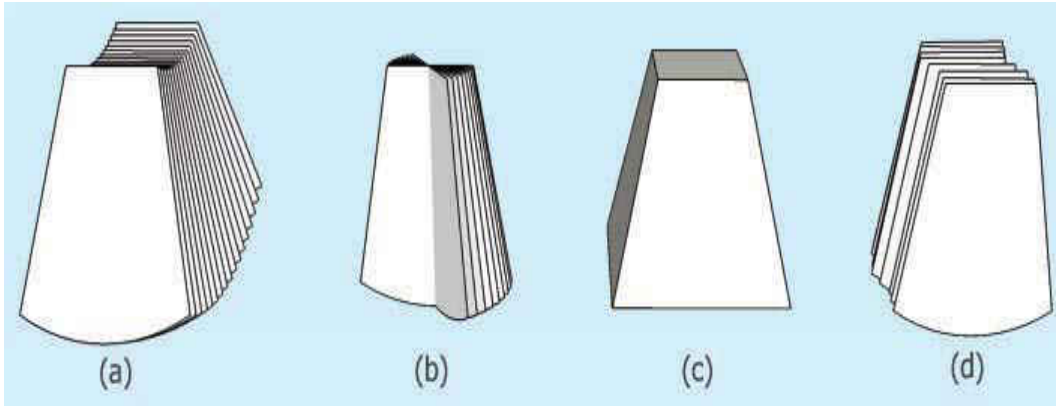
Figure 15: (a) Transducer rotated about an axis, (b) Transducer rotated about the axial, (c) 2D Array, and (d) Sliced linear scans

Ultrasound medical imaging systems are becoming more portable, less expensive, and more reliable. These advancements are being carried out in the form of improvements in enabling technologies; faster and smaller microprocessors, hand-held screens, and other related technologies. However, the PZT probe itself has not made much improvement itself. A typical ultrasound probe contains 128 elements, and each element has an electrical connection to measure the analog response of each element to an incoming wave. Commercially available probes do not normally have analog/digital conversions, hence all 128 elements must be individually connected to the ultrasound system. This makes the male connection from probe to computer extremely bulky, as shown in Figure 16. Due to the hand-manufacturing of the PZT probe, the cost for many ultrasound probes can range anywhere from $500-$3,000 USD.
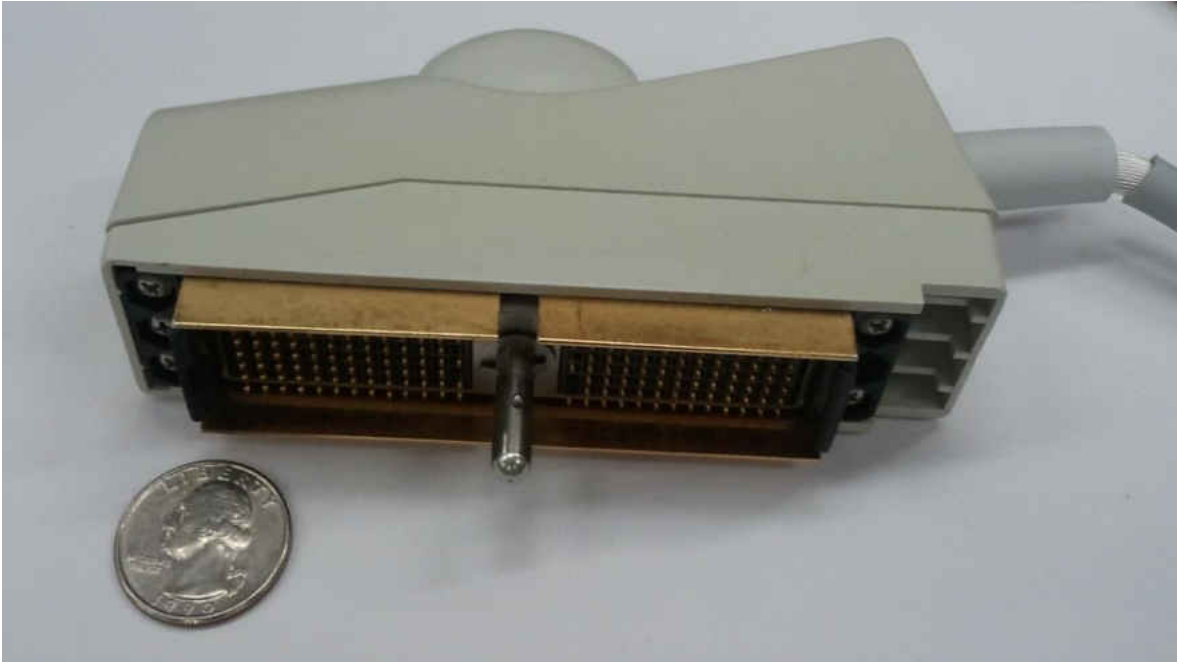
Figure 16: Conventional (bulky-sized) analog probe male connection into the ultrasound system, disassembled at UCF

A trend in medical ultrasound imaging is towards smaller and more portable devices. General Electric has recently developed the Vscan, which is a pocket or cell-phone sized ultrasound imaging system. It operates around the 2-4 MHz range, which is sufficient for mediclal imaging but not sufficient enough for specific applications. The probe directly connects to the system. The image quality is not comparable to traditional cart-based systems, and the battery life is only 1 hour long for a charge time of 1 hour.

Capacitive Micromachined Ultrasonic Transducer

The concept of the Capacitive Micromachined Ultrasonic Transducer (CMUT) is based on the electrostatic attraction force between charged capacitor plates [26]. Figure 17 below illustrates the model of a CMUT. If one plate is held stationary and the other is supplied a bias voltage, the free plate will displace due to the electrostatic force. This simple concept has found use in many applications, including: speakers/receivers [27], pressure sensors [28], pressure actuators [29], MEMS RF Switches [30], and micro fluidic pumps [31].
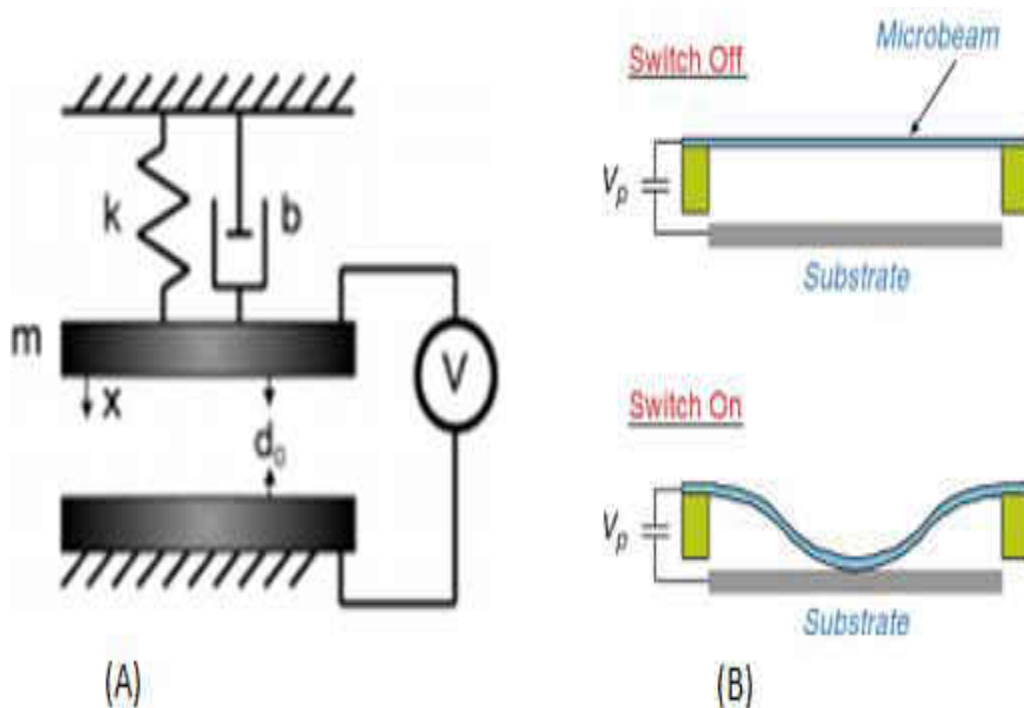
Figure 17: Parallel-plate actuator [32] (A) lumped parameter model and (B) example of a capacitive switch

The parallel plate method of operation is directly related to the sensing/receiving (Rx) mode of the CMUT, where the incoming ultrasound wave creates displacement to the statically biased membrane, thus producing a change of capacitance that results in a corresponding gray scale shaded image on screen. Capacitance, for the parallel plate electrodes, is defined as:

$$C = \frac{k\varepsilon_0 A}{d},$$

where k is the dielectric constant of the medium between the plates, ε_0 is the permittivity of space (8.854 x 10^{-12} F/m), A is the area of the electrodes, and d is the distance between the plates [33]. Thus, a smaller distance and larger area will create larger capacitance and higher change per deflection of the electrodes.

Pull-in voltage for the parallel plates, depending on the application, may be beneficial. In the case of CMUTs for ultrasound imaging, conventionally this phenomenon is typically avoided. Figure 18 demonstrates where voltage for ideal parallel plates occurs relative to the normalized gap height. Typically for a perfect parallel plate capacitor, the collapse distance of the movable plate is 1/3 of the total gap height [32].
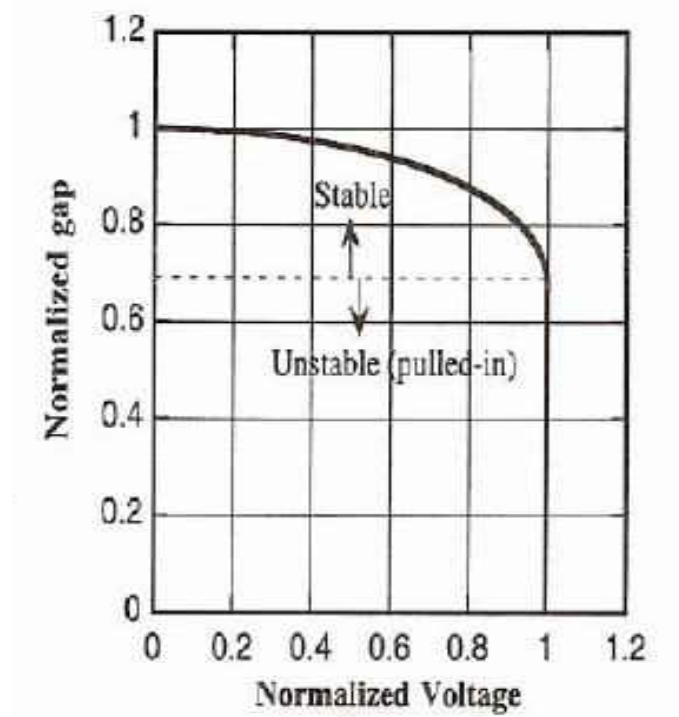
Figure 18: Stability vs instability gap distances of parallel plate capacitors [34].

An AC voltage supplied to this upper plate will cause the plate to vibrate, generating sound waves into the surrounding medium. This is known as the transmission (Tx) mode, where the volume displacement of the membrane causes a pressure output in the ultrasound range. [35]

Although parallel plate capacitors have been around in the form of speakers and receivers for audio applications for a similar amount of time as piezoelectrics, piezoelectric-based materials have been the transducer choice for the ultrasound probe. The reason for this is due to the fact that PZT ceramics traditionally provided a larger electro-mechanical coupling

coefficient over capacitance based devices [37]. In order to overcome this setback, the parallel plate capacitors have historically needed very small gap heights to exhibit very high electric fields required for ultrasound actuation and sensing, else the operation of these devices would be in the million volts per centimeter range [38]. With the advent of microelectromechanical systems (MEMS), the realization of micron and submicron gap heights is possible, thus enabling CMUTs to compete with piezoelectric ceramics.

Micromachined electrostatic transducers were first fabricated in the late 1980's and early 1990's. Soon after M. Haller and Khuri-Yakub introduced a capacitive-based transducer with more advanced fabrication technology and improved performance by 1993. Building from this newly improved CMUT with precisely controllable fabrication dimensions and submicron gap heights, more work has been conducted to further advance the CMUT technology, including: equivalent circuit modeling [39], experimental characterization techniques [40], pulse-echo testing of 16 element and 128 element transducer arrays [41], CMUT-produced ultrasound images [42], higher frequency cells [43], circular ring arrays for intravascular catheters [44], Finite Element Analysis for membrane visualization [45], monolithic integration onto IC circuits [46], and 2D arrays for 3D images [47].
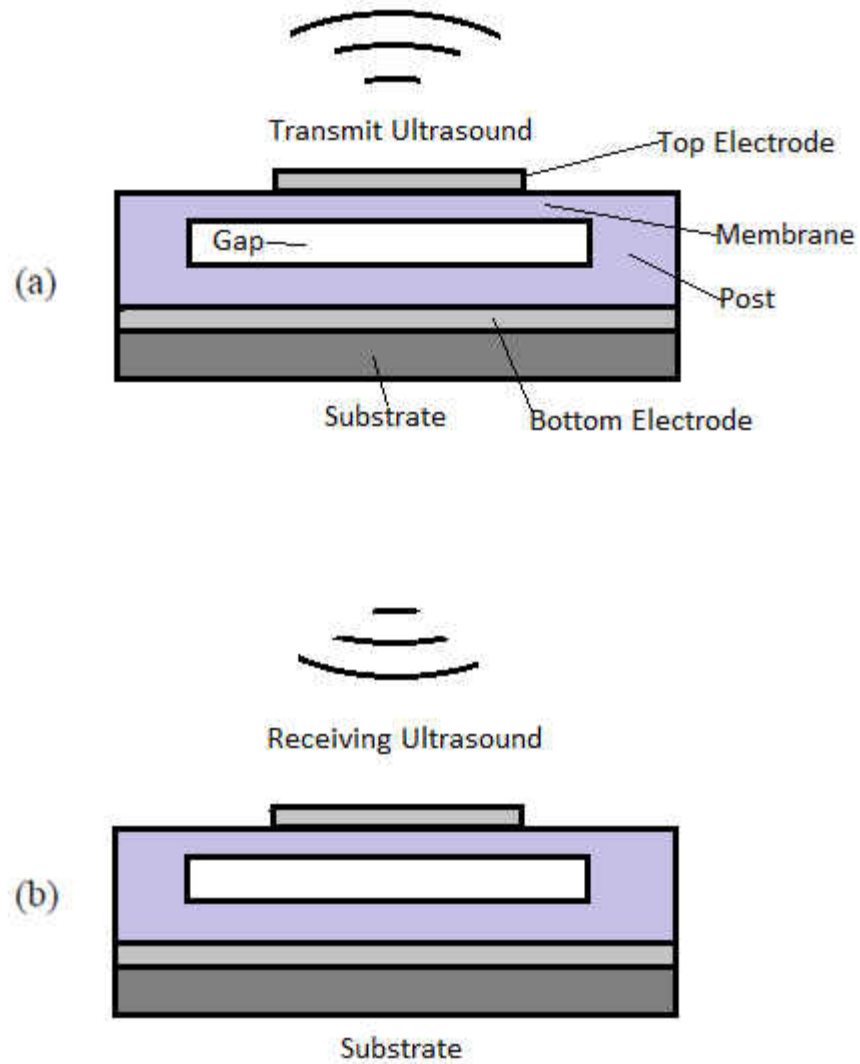
Figure 19: CMUT schematic of cells in (a) transmit mode and (b) receive mode

A major improvement the CMUT provides in ultrasound imaging is acoustic matching between the vibrating membrane and the target of interest. The characteristic impedance of piezoelectric ceramics is 33 MRayl, which is significantly higher than bodily tissues 1.6 MRayl, and thus produces acoustic mismatching [18]. The result of this acoustic mismatch translates

into very poor coupling efficiency between the membrane and air, thus leading to a low pressure output. The benefit of acoustic impedance matching provided by the CMUT is a wide bandwidth [48], and therefore an improved axial resolution of an image over PZT-based devices. Figure 20 below is an image of the thyroid gland [9] and demonstrates the comparison between a PZT-based image (left) and a CMUT (right). It is evident that the PZT image has sharper edges and features, however due to lower bandwidth and axial resolution it has a smaller range for dynamic gray scale shading. The CMUT has higher dynamic gray scale shading; however the transduction efficiency (pressure output) of the CMUT lacks in comparison to PZT, as the CMUT image is very fuzzy and not well defined.
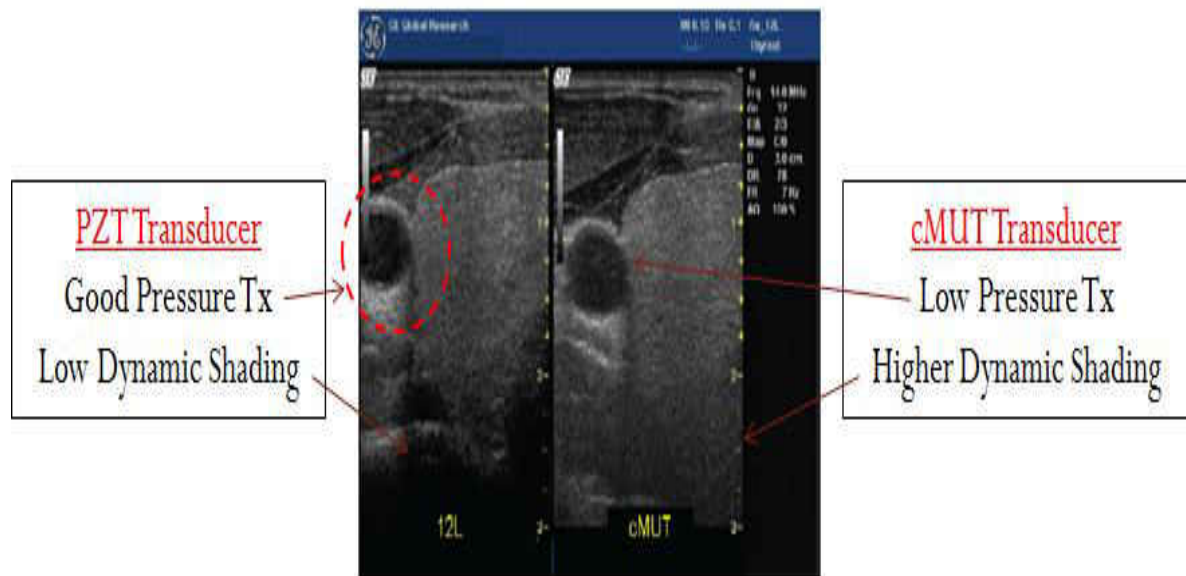
Figure 20: Thyroid gland ultrasound image using (left) PZT transducer and (right) CMUT transducer [9]

Current Problems/Issues with CMUTs

The biggest concern with enabling the CMUT cell to compete with the PZT ceramic for ultrasound imaging is the need for better transduction efficiency (pressure output) of the membrane (as demonstrated in Figure 20 above), and the need for a less expensive and lower temperature fabrication method for CMUT monolithic integration on IC analog signal processing circuitry for easier 3D imaging.

The root cause of the low transmission output problem is directly linked to the small gap height [49]. Many silicon-based membrane cells only have cavity heights within the submicron range, but most are as low as 0.2 μm [50], [51], [52]. The purpose of having such small gap heights is due to the fact that the collapse voltage is dependent upon the height distance between the two electrodes, and silicon or silicon nitride are such stiff materials (E ~200-250 GPa) that very large voltages would be needed to deflect the membrane with gap heights greater than the submicron range. Much analysis has been placed into the question of an appropriate gap height [49], and it has been noted that a gap in the submicron (0.2 μm) range can make for a low voltage silicon membrane operation; however a 2.0 μm gap is needed for the silicon-based CMUT to output more pressure. Several attempts thus far have been made at achieving this critical milestone of higher pressure output for the CMUT, including: the collapse-snapback operation mode, dual-electrode cells, and polymer-type membranes. All revolve around the concept of achieving a larger membrane deflection [53] profile to solve the transduction efficiency [54] issue with CMUTs.

Increasing Tx by Collapse-Snapback operation

Dr. Khuri-Yakub's group has proposed a method of collapse-snapback operations to exploit the full gap height for deflection [10]. This method utilizes the principal of electrostatic stability of two parallel plates, and can be seen in Figure 21. The device is operated beyond collapse and contact is made between the membrane and insulation-covered substrate. In return for operating the top electrode past the stability range, this larger deflection in conjunction with a dynamic membrane produces a higher pressure output.

The collapse-snapback operational regime does seem to produce a larger output pressure by utilizing the full range of the gap height; however the gap height tends to be well below the 1.0-2.0 µm range [55] and frequent membrane-substrate contact may compromise reliability. Stability of the transmitting mode by operating in the collapse-snapback region may also be an issue due to the fact that the membrane cannot be controlled past the stability range of parallel plate electrodes.

Ultimately, it has been shown that transmission and reception performance improvements due to collapse/snapback operations have come at the expense of increased dependence of capacitance on current bias voltage and voltage history (hysteresis) [56].
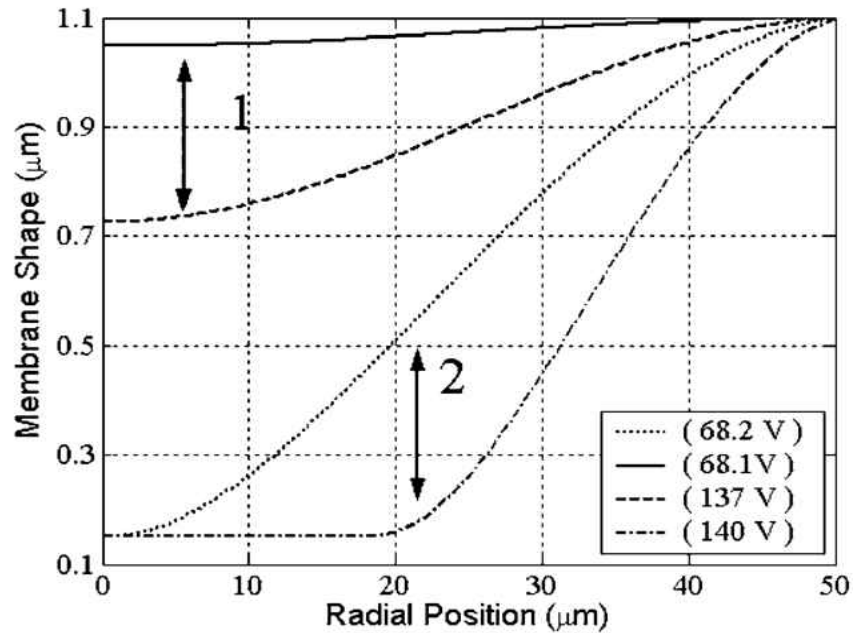
Figure 21: Radial deflection profiles of (1) normal operation of a CMUT and (2) Collapse-snapback mode [10]

Increasing Tx by Dual-Electrodes

Alternatively, to improve the operation of this device in Tx and Rx, other groups have introduced multiple electrodes and non-uniform membrane structures to enable the silicon nitride material to deflect more during sensor mode [11]. The novelty behind this design is that the center electrode is statically operated with a DC bias voltage during Rx mode for heightened sensitivity to incoming ultrasound waves, while the side electrodes are operated with an AC signal superimposed over a DC voltage to generate membrane vibrational motion. The membrane material between the electrodes allows more flexibility at the joints, and thus

promotes a "piston-shaped" deflection profile for Rx sensitivity and a larger volume deflection

for Tx pressure output. Granted this increases the sensitivity of the CMUT due to such a small

gap and a large deflection profile of 62.5% the original gap height, it also comes with the

unfortunate consequence of adding more mass and requiring more electrodes for each

membrane, essentially doubling the number of interconnects to be multiplexed by the

electronics [57]. Furthermore, due to the fact that the material is still the traditional Si_3N_4, the

gap height is still well below the height of 2.0 µm needed for better transduction of pressure

output. The schematic of the dual electrode CMUT is demonstrated below in Figure 5.
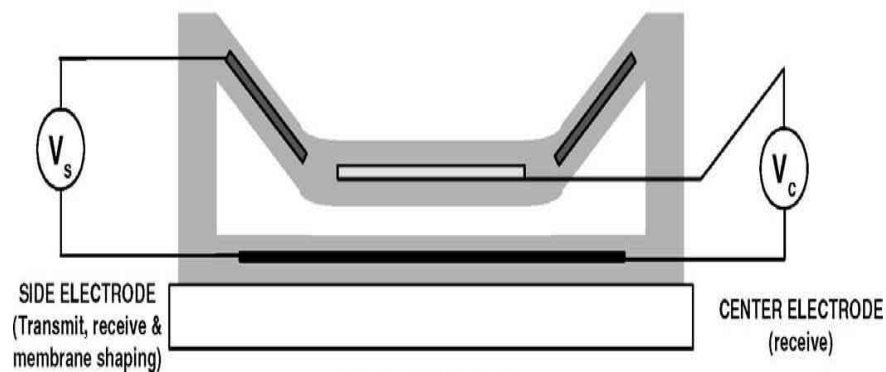
Figure 22: Dual electrode CMUT. Side bias (V_S) is used in Tx mode and Center bias (V_C) is used in Rx mode [11].

Increasing Tx by using Polymer Membranes

Polymer type CMUTs are slowly emerging as a viable alternative to silicon nitride membrane material due to its flexibility, excellent dielectric properties, durability, relative ease of fabrication, and cost savings as compared to silicon nitride. Although the high stiffness of silicon nitride allows for very high frequency operations (>10 MHz) [10], the drawback in current CMUTs is rooted in this very choice of material. Silicon nitride has a high Young's Modulus constant and thus requires very high voltages for operation. Polymer membranes have a lower Young's Modulus (<5 GPa) and need less electrostatic force to deflect the membrane, leading to lower voltage requirements. The idea is that large gap polymer membranes can deflect low enough [17] to the bottom electrode to generate sensitivity comparable to that of Si_3N_4 membranes, eliminating the need to fabricate devices with very low (0.2 μm) cavity heights. It has been shown [58] that Simulations with a polymer membrane demonstrated a maximum membrane deflection increase up to 67% when compared to nitride. Furthermore the benefit of a larger deflection and gap height is that higher pressure transmission can be achieved using polymer membranes while maintaining a similar sensitivity to Si_3N_4 CMUTs and their respective submicron gap heights.

The problem with current polymer CMUT research is that the operational frequency tends to be very low. DY Chiou et al. [12], [59]reported a polymer-based CMUT membrane fabricated with SU-8 membranes. The result was a CMUT cell with an operating frequency of only 1 MHz. Ming-Wei, et al. studied a CMUT called Sonic Paper [60]. The substrate was very

flexible, and the membrane was also made of polymer-type material. The membrane was 5 um

thick, while traditional CMUTs are only around 1 um thick. Although the polymer membrane

exhibited a very flexible deflection profile, the drawback to such a design was that the polymer

material was too flexible and only had a resonant frequency of 1[MHz]; meanwhile higher

frequency structures are required to operate for higher-end medical imaging applications.

Current CMUT Fabrication Methods

When designing CMUTs, a future concern towards CMUT-CMOS electronic circuit

integration is the fabrication temperature at which the hottest step will achieve. The highest

process temperature cannot exceed 400^oC in order to remain CMOS compatible. However, the

most common methods of current CMUT fabrication exceed this temperature, most notably

Low-Pressure Chemical Vapor Deposition (LPCVD) to deposit Si_3N_4 membrane material and

poly-silicon sacrificial material. Traditional CMUTs are fabricated by either surface

micromachining (sacrificial release) or by bulk micromachining (wafer bonding) processes.

Surface micromachining of silicon nitride for the membrane material is the most popular

method of membrane deposition in CMUT research. It is noted that the surface

micromachining by the LPCVD method produces the highest quality thin film membrane than

PECVD, yet requires a high fabrication temperature. However, depending upon processing

conditions in LPCVD the thin film membrane may be susceptible to large residual stresses.

Etching of the sacrificial material becomes a problem after the membrane has been sealed over

this material. Multiple steps must be added to "drill" smaller holes into the membrane to access the sacrificial layer. The consequence of smaller holes in the membrane either results in more CVD processing time to seal the holes, or a membrane with a lower structural resonating frequency.

Wafer bonding is an attractive alternative to silicon nitride LPCVD/PECVD micromachining techniques, due to simpler manufacturing steps, potential performance improvements, and ultimately cost benefits. Wafer bonded CMUTs exhibit the same mechanical and electrical properties consistently throughout the device, unlike that of surface micromachining techniques which are susceptible to possible changes, such as residual stress during fabrication, etc. Due to the direct bonding between membrane-post, the wafer bonding method completely skips the sacrificial structural layer that is required by surface micromachining techniques to facilitate membrane deposition. This saves a considerable amount of time, and adds to the benefit of not having holes drilled into the membrane. On the same note, the lack of sacrificial layers allows for a higher fill-factor of the membranes, essentially increasing the active element area of the transducer by reducing the width of the support post to 2 μm. Considering large scale manufacturing costs, wafer bonding is the most beneficial. Another added manufacturing benefit to the wafer bonding method is that a non-uniform (illustrated in Figure 23) membrane shape can easily be created. This type of membrane attempts to achieve a more piston-like deflection profile for the membrane, which leads to higher capacitance change (sensitivity) and higher volume displacement (pressure transmission).
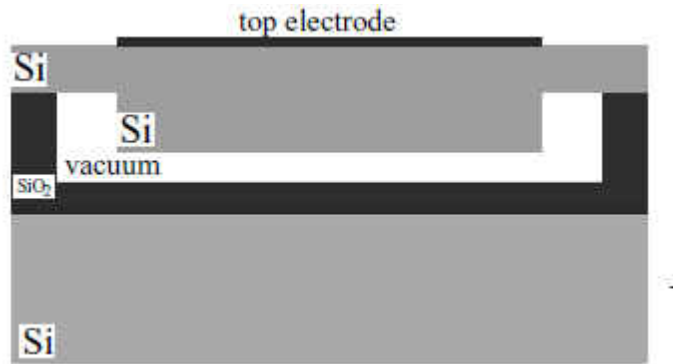
Figure 23: Non-uniform membrane for piston-like deflection profile

Processing turnaround time and number of steps for manufacturing the wafer bonded CMUT is significantly reduced by 50% for the wafer bonded CMUT. This ultimately leads to the wafer bonding technique showing a heightened difference in higher volume-manufacturing processing cost when compared against other fabrication methods.

Ultimately, the most reliable CMUT fabrication method for considering CMUT integrity and the fabrication onto analog processing integrated circuitry at low temperatures is a hybrid integration of the high temperature LPCVD CMUT transducer substrate connected onto the IC circuit's substrate. This approach uses electrical through-wafer interconnects as well as flip-chip bonding for connecting the two substrates. It appears that the need for low temperature fabrication steps has been eliminated by this method, however this method adds more steps and processing time to the CMUT fabrication.

Surface Micromachining (sacrificial release)

The CMUT process begins with a silicon wafer, which is doped to achieve high conduction to the surface. This doped region will serve as the ground electrode, as opposed to depositing a metal layer on top of the substrate. A very thin layer of LPCVD Si_3N_4 is deposited on top of the silicon substrate to form an etch stop for the proceeding sacrificial layer (polysilicon), and also to prevent a short circuit at collapse between the top and bottom electrodes. This insulation layer is required to be very thin, less than a micron, due to the fact that the capacitance of the etch-stop layer is in series with the active gap capacitance. Several hundred angstroms of silicon nitride is sufficient. Next, the deposition and patterning of the sacrificial layer, polysilicon, is performed in two steps to ensure that the channel used by the release of the sacrificial layer is thinner than the gap distance. A layer of polysilicon is deposited using LPCVD and regions of reduced channel height are defined by photolithography, as shown in Figure 24(a). Dry etch is used to completely remove all of the polysilicon in the region, and stops at the previously defined insulation layer of Si_3N_4. A second thin layer of poly-silicon is deposited, and is demonstrated in Figure 24 (b). The thickness of the second layer of poly-silicon determines the height of the cavity. To allow better control over thicknesses in poly-silicon LPCVD, a low temperature ($560^{o}C$) is preferred. A second photolithography step and dry etch is performed to define the membrane shape, the cavity, and the etch channels (Figure 24 (c)). The next step is to create the membrane by depositing Si_3N_4 by LPCVD at $785^{o}C$, as shown in Figure 24 (d). Silicon nitride membranes are prone to intrinsic stresses, and thus

the composition of gasses is crucial. To achieve a low stress silicon nitride film, the following is used: dichlorosilane ($SiCl_2H_2$) to ammonia (NH_3) at a ratio of 14:1. A lithography and dry etch step is performed to open small holes through the Si_3N_4 membrane (Figure 24 (e)). This allows exposure of the poly-silicon to a potassium hydroxide (KOH) bath. To release the membrane (Figure 24 (f)), the wafer is immersed into the KOH. It is noted that the KOH etch rate is determined by the temperature as well as geometric size of the membrane and cavity. The KOH should be above room temperature, else the etching rate of poly-silicon can take days to complete. The final membrane thickness is determined by the additional silicon nitride needed to seal the etching cavity (Figure 24 (g)). The silicon nitride deposition process is performed with LPCVD at a low pressure (200mTorr at 785^oC), thus cavity is essentially vacuum-sealed. Finally the top aluminum electrode is created by sputtering a thin layer of aluminum over the wafer and patterned by photolithography and wet etching (Figure 24 (h)).
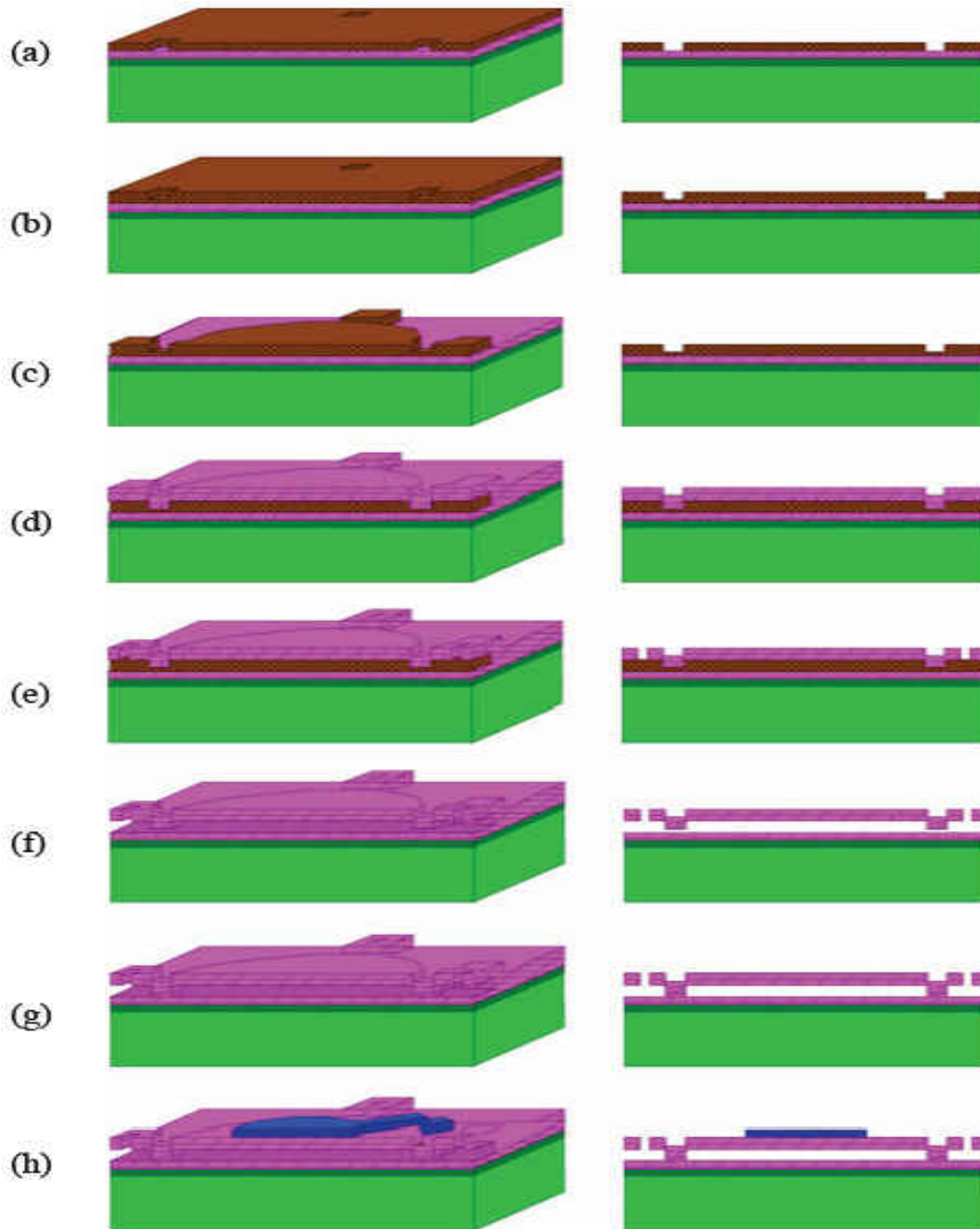
Figure 24: Surface micromachining (sacrificial release process) for a CMUT cell, (a) Substrate doping, etch-stop layer deposition (Si_3N_4 by LPCVD), first sacrificial layer (Si_3N_4 by LPCVD), (b) second sacrificial layer deposition, (c) patterning of cavity shape, (d) membrane deposition, (e) release holes, (f) sacrificial release in KOH, (g) seal etch holes, (h) sputtering aluminum for top electrode

Bulk Micromachining (wafer bonding)

Wafer-bonding is a method considered to be a bulk micromachining process. The three basic wafer bonding processes are: anodic bonding, fusion bonding, and adhesive bonding. Among these three techniques, silicon fusion bonding the most prevalent in many of today's MEMS applications. Wafer-bonding of CMUTs also uses silicon fusion bonding.

The fabrication process of a CMUT using the wafer-bonding method begins with two wafers: a prime quality silicon wafer and a silicon-on-insulator (SOI) wafer. As in the sacrificial released CMUT, a doped silicon wafer is used to create the bottom electrode. Oxide is thermally grown on the silicon wafer. The thickness of this thermally grown oxide determines the thickness of the CMUT cavity. The shape of the cavity is defined by a photolithography step. The oxide is wet etched using HF, as shown in Figure 25(a). To avoid short-circuiting between the top and bottom electrodes of the CMUT device upon membrane-surface contact, a layer of silicon dioxide is thermally grown (Figure 25(b)). The two wafers are brought into close contact, and Van der Waals forces and weak hydrogen bonds are formed (Figure 25(c)). The wafers are annealed at 1100°C to form a strong covalent bond. The buried oxide is removed using hydrofluoric acid (Figure 25(d)). The top electrodes are then sputtered on the wafer, and patterned by photolithography (Figure 25(e)). Finally, the elements are defined in the CMUT array by etching isolation trenches by photolithography and silicon etching (Figure 25(f)).
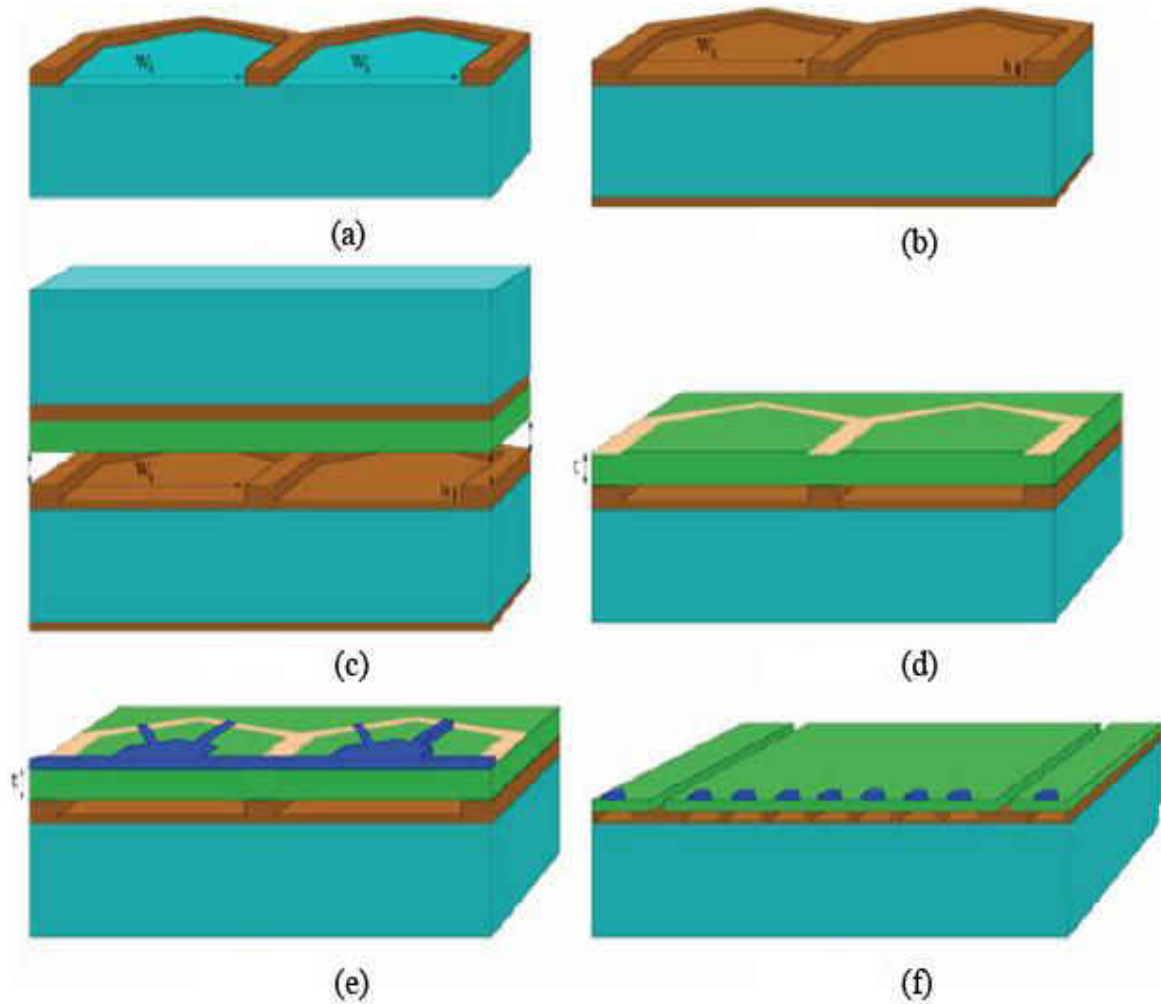
Figure 25: Bulk micromachining (silicon fusion bonding) process of a CMUT cell, (a) Thermal oxidation and cavity definition with photolithography and etch, (b) Insulation layer grown by thermal oxidation, (c) Direct bonding of silicon wafer to the SOI wafer, (d) release of the membranes by removal of the top silicon layer and the buried oxide layer, (e) sputtering of metal and patterning by photolithography, (f) CMUT array (element) defined by photolithography and etching of silicon.

Parylene-C Material

Parylene (poly-paraxylylene) is a polymer that has found an emerging use in MEMS fabrication due to its many benefits, including: biocompatibility, chemically inert film, completely homogeneous surface, excellent dielectric properties, conformal and pinhole-free deposition, room temperature fabrication, and low intrinsic thin film stress. Parylene deposition has traditionally been used as a protective moisture barrier for electronics, however parylene has been finding use as a structural material that can be micromachined into MEMS components. Many recent research areas have focused on parylene as choice material for applications, including an implantable MEMS intraocular pressure sensor [61], RF MEMS switch [62], an electrothermal valve [63], and surface micromachined membrane for sensor applications [64].
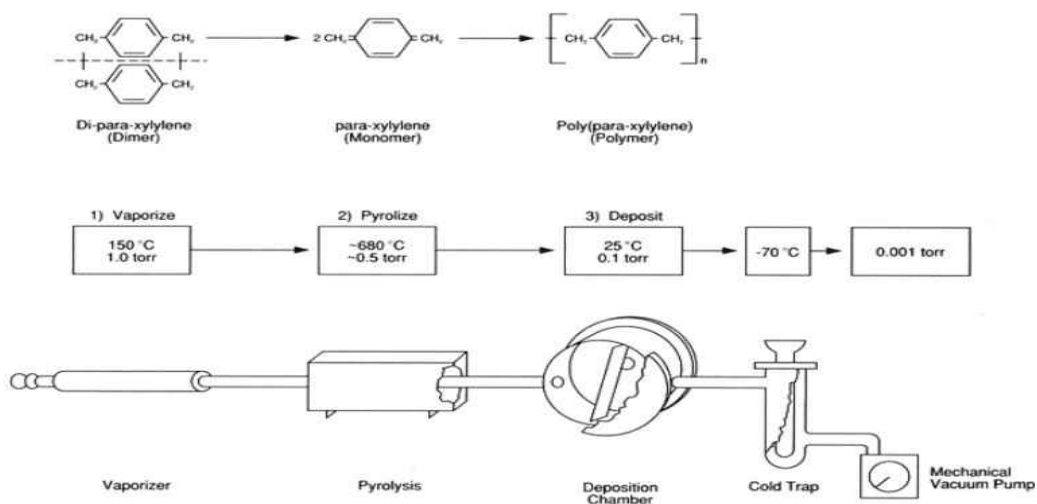
Figure 26: Parylene CVD Process

Figure 26 above demonstrates the CVD process for the Parylene Deposition System. The

parylene dimer is loaded into the vaporizer chamber at approximately 150°C and 1 torr,

depending upon the specific recipe. Once the dimer is vaporized, the vapors are pyrolized at

about 680°C to form a monomeric para-xylene. The monomer is then allowed to enter the

deposition chamber at room temperature, and the parylene polymerizes on the substrate. A

conformal layer is formed throughout the structure, as demonstrated in Figure 27 below.
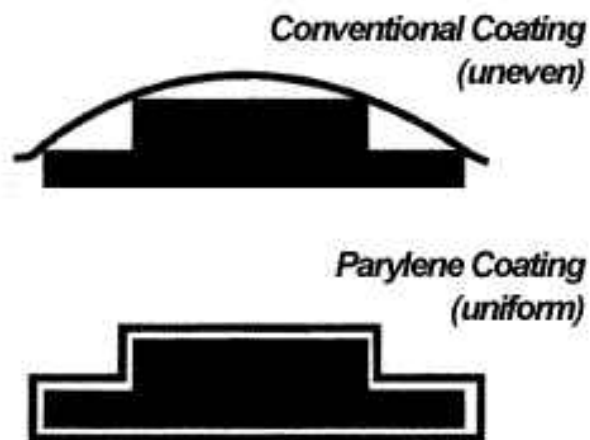
Figure 27: Conformal uniform coating of parylene onto surface features [65].

CHAPTER THREE:
PROPOSED PARYLENE-C/GRAPHENE FABRICATION

Overview of proposed fabrication

This thesis introduces a new fabrication process for manufacturing of a CMUT device, and the aim of this new procedure is to reduce the cost of the overall transducer while at the same time either retaining or improving upon operational benchmarks (pressure output, sensitivity, voltage consumption, and center frequency). The individual fabrication steps proposed here are derived from matured techniques and have been previously done on other MEMS microfabrication-type research, however the combination of these steps towards a CMUT device is the novel approach. Figure 28 below summarizes the fabrication process. Aluminum is deposited onto a substrate (Figure 28(2)) followed by an insulation layer to prevent short circuiting (Figure 28(3)). The SU-8 post is spun-on (Figure 28 (4)) and the parylene-coated graphene is transferred to the post (Figure 28(5,6)). Finally, electrical connections are made (Figure 28 (7)) prior to the entire transducer being sealed with parylene (Figure 28(8)).
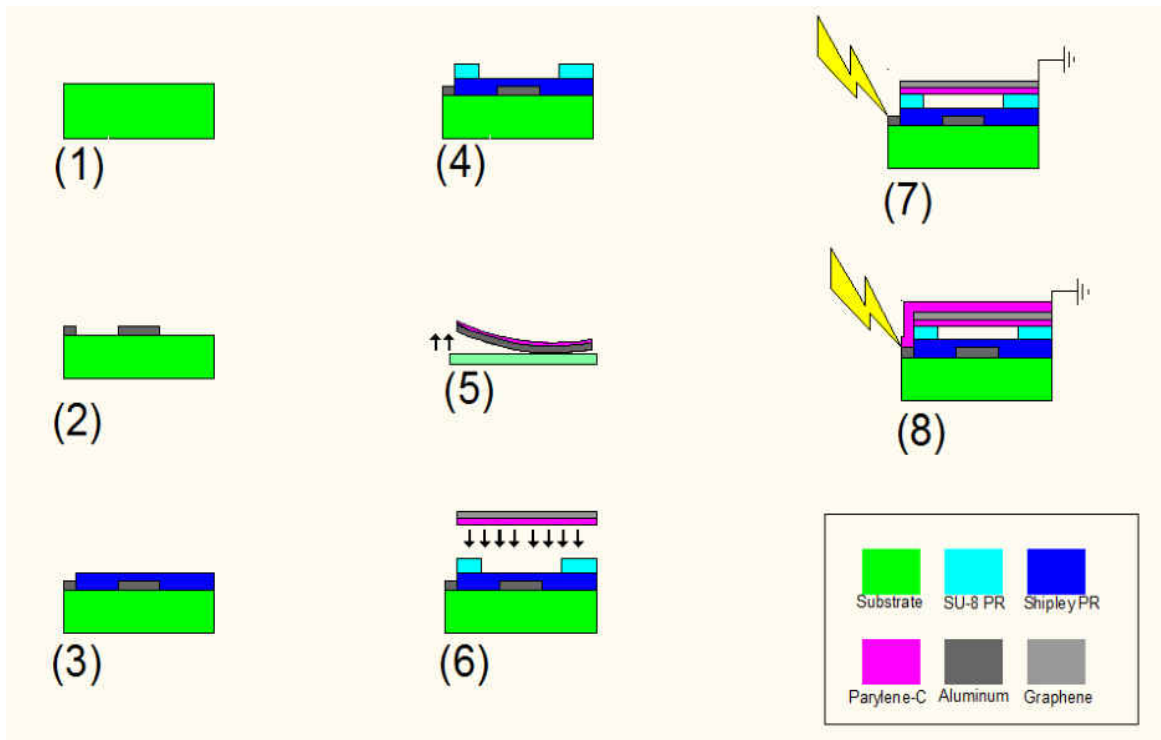
Figure 28: A substrate(1) is deposited with aluminum (2) as the ground electrode. An insulation layer is applied (3) and SU-8 support posts are spun-on (4). Graphene is grown via CVD and coated with Parylene-C (5) and transferred to bond with the SU-8 post (6). Electrical connections are made (7) prior to full transducer device sealing (8).

The parylene structured device may be fabricated not only on a silicon substrate, but also many other less expensive substrates such as glass. However, analog processing circuits will most likely be fabricated on silicon, thus this work will focus on silicon as the substrate.

The advantage of using Parylene-C as opposed to traditional materials such as silicon nitride is that the CVD method for Parylene is much less specialized than PECVD or LPCVD. Also, the graphene electrode may be grown separate from the CMUT cell, thus decreasing turn-

47

around time in manufacturing the probe, whereas silicon-based CMUTs require an almost finalized cell to be present prior to PVD of aluminum over the device surface.

Bottom Electrode

The fabrication of the bottom surface electrode for the CMUT cell follows commonly-used lift-off procedure of an aluminum material deposited onto patterned photoresist. The bottom electrodes are individually patterned into circular shapes and connected to neighboring electrodes by a thin line shape, so as to reduce parasitic capacitance as much as possible. Conventionally the bottom electrode serves as the ground, however in this approach the bottom will serve as the voltage input.
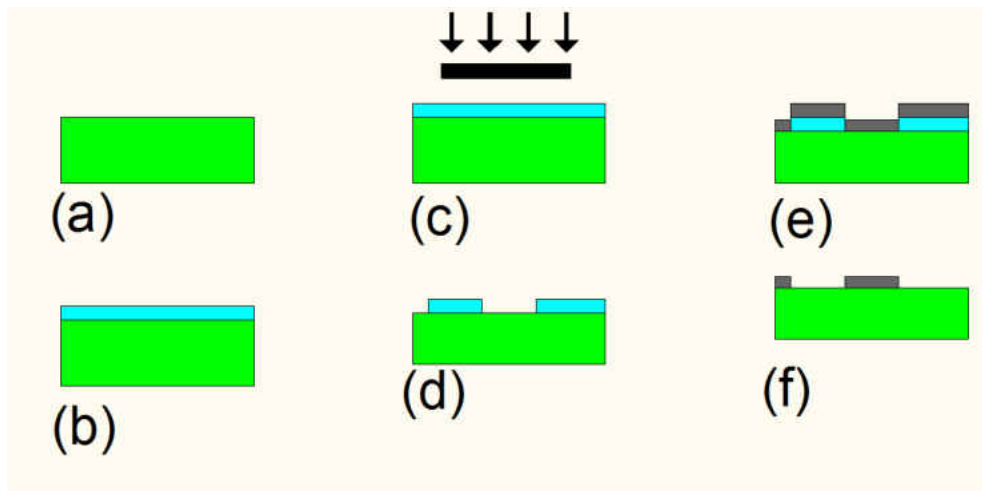
Figure 29: Aluminum lift-off to form bottom electrode

To prevent short circuiting, a very thin layer of insulator material is deposited onto the electrode. Photoresist is spun-on as the required short-circuit insulator and patterned to cover the electrodes, while ensuring an open space on the bond pad for the bottom electrode electrical connection.
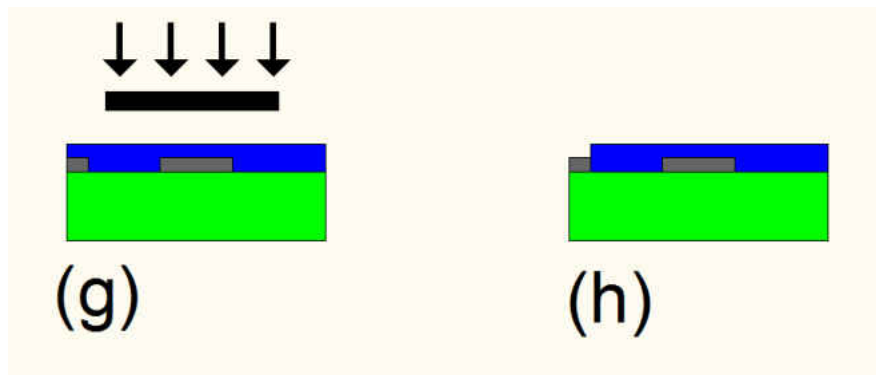
Figure 30: Insulation to prevent short circuiting

Support Post

A SU-8 epoxy-based negative-tone photoresist is used to create the support columns for the membrane. It has been used many times in applications that require fabrication/adhesion of SU-8 directly onto Parylene-C [66]. The photoresist is applied with a plastic pipette onto the center of the wafer, and the substrate is spin-coated at 4000 rpm for 30 seconds. The specimen

is then softbaked on a hotplate at 65°C for 5 minutes and 95°C for 15 minutes. After exposure under a mask aligner, the SU-8 is post-exposure baked to ensure crosslinking.
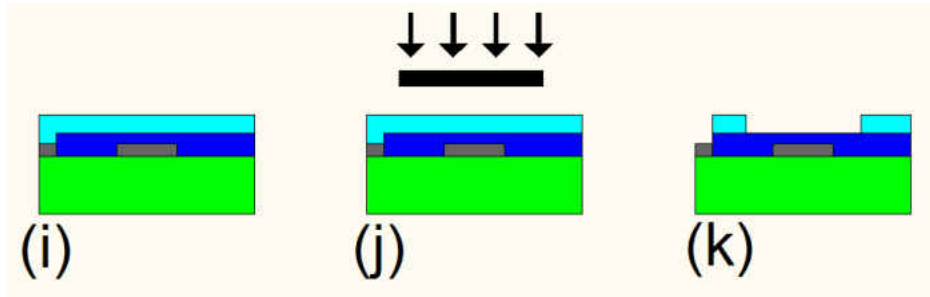
Figure 31: SU-8 support posts, fabricated by spin-on

Graphene CVD Growth

A method for patterned graphene has been previously introduced in literature [67], and is easily applied to the above steps. This method has the advantage of having a large area, which is needed to safely cover the region of the transducer. A 300 nm layer of patterned nickel is deposited onto the silicon wafer with SiO$_2$ previously grown. Next, inert argon gas is heated in the quartz tube CVD chamber at 1000°C, while gases of CH$_4$:H$_2$:Ar are passed through at 50:65:200 standard cubic centimeters per minute. Next, the substrate is rapidly cooled to room temperature at a rate of 10°C s^{-1} by supplying argon. The previous authors have noted that this cooling rate is critical in suppressing extra graphene layer growth, and also for effectively separating the graphene from the substrate in future steps.
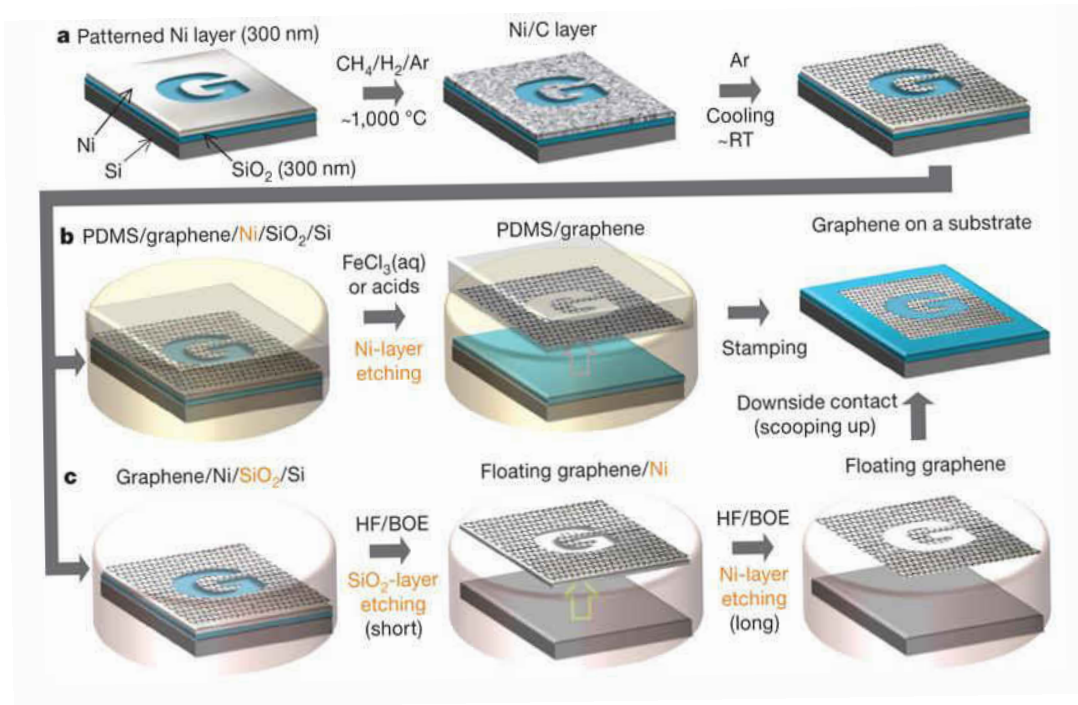
Figure 32: Graphene CVD growth process flow chart [67]

After graphene has been successfully grown onto the Si/SiO$_2$/Ni substrate, the nickel is etched and the graphene is transferred onto a PDMS substrate for further handling. The nickel may be etched away with a solution of FeCl$_3$. Although there are different methods of transferring the graphene layers, the option to use PDMS stamp as the new transferring substrate is quite convenient for steps that require further microfabrication/handling of the thin graphene film. The alternative step involved etching the SiO$_2$ layer in a buffered oxide etch (BOE) to separate the silicon substrate from the graphene/nickel. Then further BOE or

hydrogen fluoride solution is used to remove the nickel layer. Figure 32 above illustrates the

steps of graphene growth.

Graphene/Parylene Membrane

Parylene-C is deposited onto the graphene/PDMS specimen obtained from the previous

steps above. This produces the bottom portion of the membrane. The PDMS substrate is then

peeled off and the newly formed parylene/graphene membrane is bonded to the SU-8 support

posts, with the parylene coming into contact with the SU-8. The parylene layer is very thin in

this step, as this deposition only serves to adhere the graphene to the post. The graphene is

purposely left as thin as possible in order to minimize the distance between the top and bottom

electrodes.
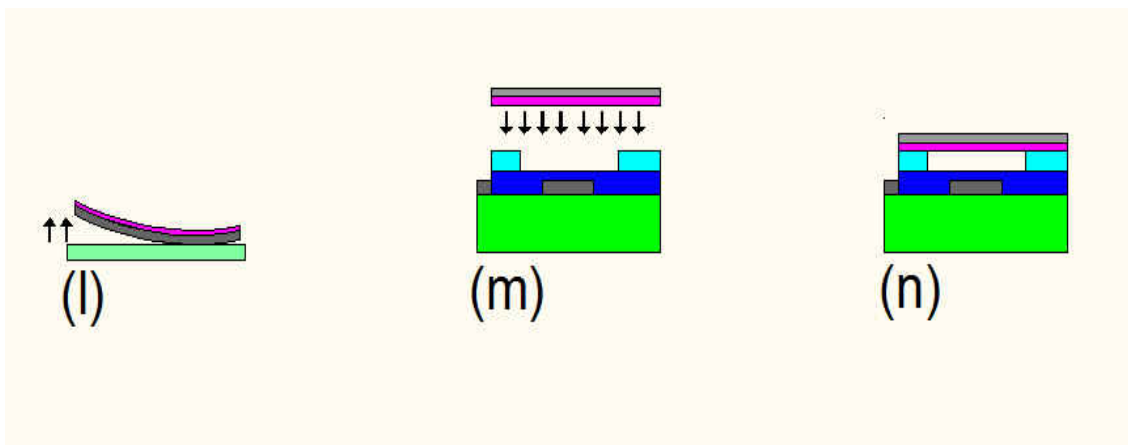
Figure 33: Graphene transfer onto SU-8 support post

To fully seal the device, on last layer of parylene is deposited onto the entire surface. Prior to this deposition, electrical connections are made. This step is needed to both to variably increase the thickness of the membrane as well as to fully seal the CMUT device from the outside environment.
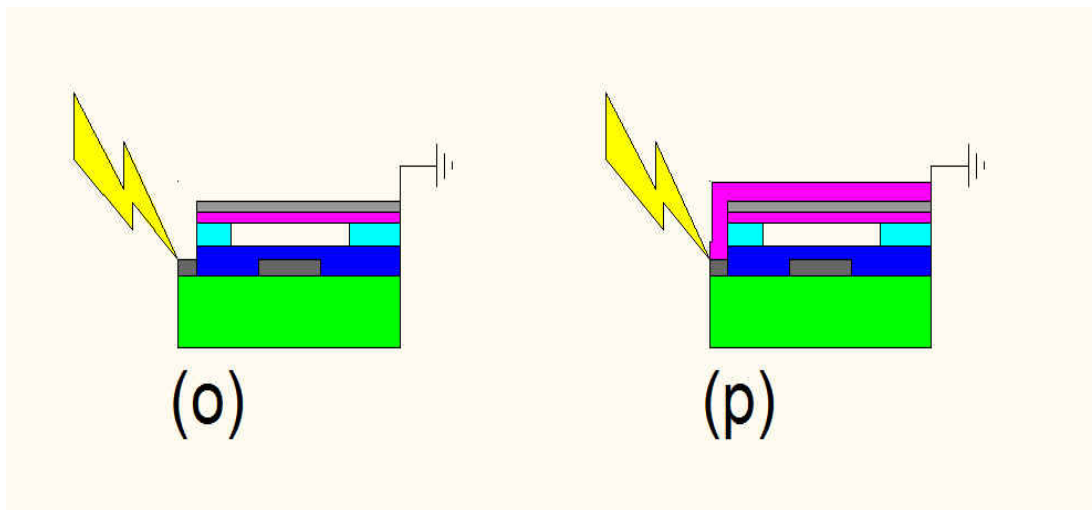
Figure 34: Electrical connections made (o) and CMUT device is fully sealed (p).

CHAPTER FOUR:
METHODOLOGY

Numerical Simulation vs Analytical Modeling

Simple analytical models provide insight into the basic idea of operational parameters by giving a "ball park" approximation of the expected results [68]. Although such calculations can be performed relatively quickly, the drawback is that these simplified models are often linear (i.e. piston-shaped deflection) or ignore very important boundary conditions necessary for full simulation of the CMUT device. For example, post (membrane support) dimensions and material properties are not taken into account when dealing with basic analytical or equivalent circuit equations, as analytical equations rely upon the fact that the membrane is either clamped [69] at the edge or the two parallel plates attract in a piston-shaped manner (i.e. pure up and down motion), as illustrated in Figure 35 below.
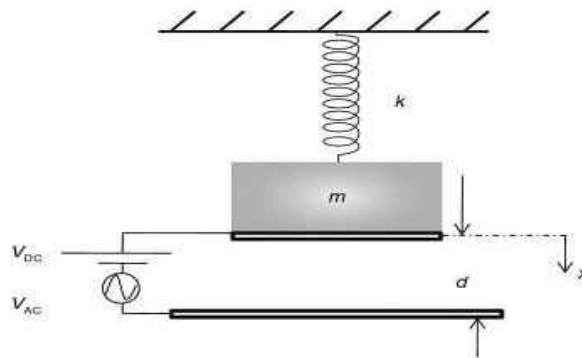
Figure 35: Parallel Plates with pure piston motion (pure up and down, no bending) [32].

Furthermore, complex CMUT designs, such as membrane notches [70] or uneven layers [71], can prove very difficult to account for in the simplified analytical models. For this reason numerical modeling provides a greater insight into operational parameters based on such complexities, and COMSOL Multiphysics is the tool capable of numerical simulations.

Governing Equations

The main challenge in accurately simulating a CMUT device is to account for the electrostatic-mechanical interaction in a certain environment (vacuum, air, water, etc.). In particular, there must be a coupling mechanism that accounts for all physics domains simultaneously. An iterative solving method must be employed due to the highly non-linearity of the coupling mechanism [68].

Both CMUTs (Parylene-C/Graphene and Silicon-based) are modeled as circular membrane cells and evaluated as axial symmetric 2D models in COMSOL Multiphysics. A 2D axial symmetric model serves as a very close approximation for the 3D case, and has the advantage of significantly faster computation time versus a full 3D model. A cross sectional view of the general 3D CMUT structure being approximated (regardless of the particular case of using graphene, carbon nanotube, aluminum electrode, etc) is illustrated in Figure 36.
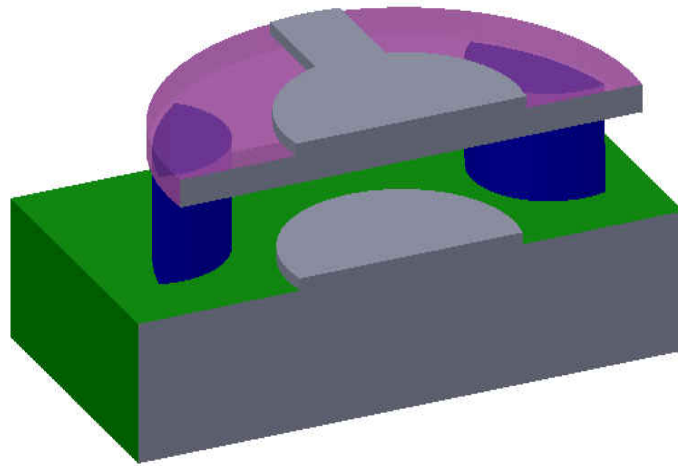
Figure 36: 3D CMUT structure

As for the generalized 2D axial symmetric schematic of the geometries being modeled in COMSOL, the geometric setup is illustrated below in Figure 37. The grounded electrode and the upper electrode can be patterned in order to reduce parasitic capacitance [57].
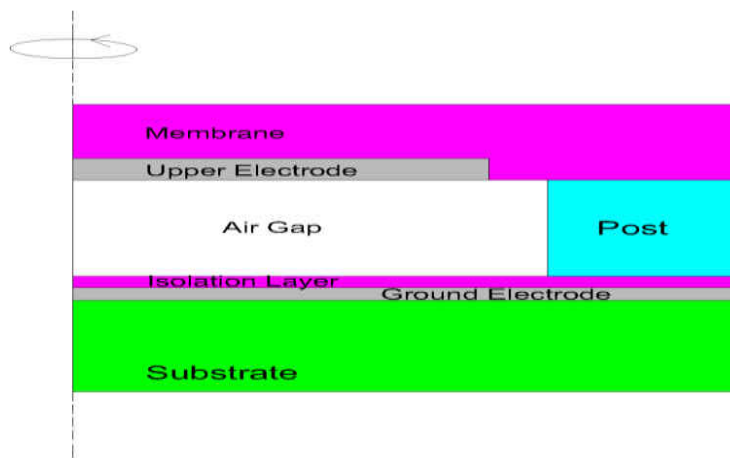
Figure 37: Axial Symmetric geometry to be modeled

Once fully revolved, the 2D axial symmetry of the model will be comparable to the CAD illustration below. Note that although the 2D approximation is very good, the axial symmetry neglects the patterning and separation of the support post that fully defines the actual 3D representation of the CMUT device in this research.
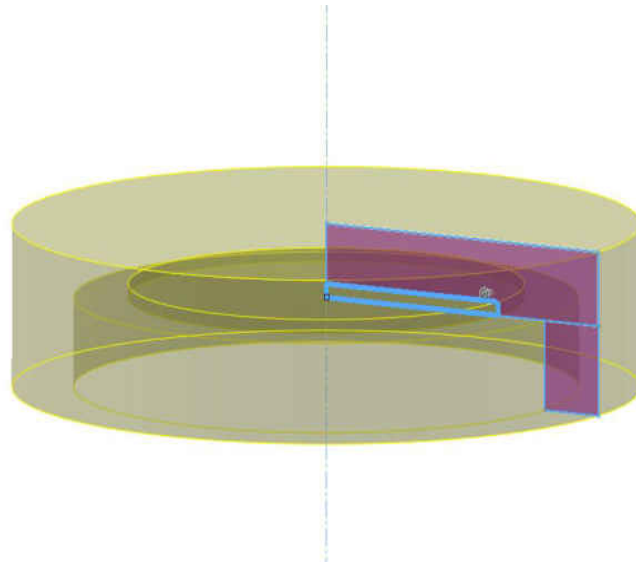
Figure 38: Axial Symmetric Model is revolved. The numerical solution assumes the 2D geometry will be revolved.

COMSOL utilizes Finite Element Analysis (FEA) to find a numerical solution to the Partial Differential Equation (PDE). The PDE's account for the material properties as constants in the equation. In the setup for the CMUT model, governing PDEs that represent the involved physics are chosen. These consist of: the mechanics of the structural field, the pressure of the acoustics field, and the electrostatic field. A 2D axial symmetric representation of the device is solved for, as mentioned previously. The geometry for the 2D CMUT representation is set up.

The boundary conditions for the static case are applied for each physical domain. These boundary conditions take into consideration the dependent variable in one of three forms: the Dirichlet boundary condition (dependent variable), the Neumann boundary condition (derivative of the dependent variable), or the relationship between the dependent variable and the derivative.

Mechanical Field

In COMSOL Multiphysics, the solid mechanics interface describes the motion and deformation of a solid object through a series of equations. Very important to the ability to couple multiple physics into the model is the consideration for the user (or from other physics domain) prescribed volume force, $\mathbf{f}_V$ (force/area).

Mechanical Field General Equations

At equilibrium, the sum of all the forces and moments on a solid body are zero. The stresses on each face of a solid body can be defined as the following stress vectors:

$$\boldsymbol{\sigma}_x = \sigma_{xx}\mathbf{e}_x + \sigma_{xy}\mathbf{e}_y + \sigma_{xz}\mathbf{e}_z$$

$$\boldsymbol{\sigma}_y = \sigma_{yx}\mathbf{e}_x + \sigma_{yy}\mathbf{e}_y + \sigma_{yz}\mathbf{e}_z$$

$$\boldsymbol{\sigma}_x = \sigma_{zx}\mathbf{e}_x + \sigma_{zy}\mathbf{e}_y + \sigma_{zz}\mathbf{e}_z.$$

The combination of these normal stress vectors, made up of normal stresses and shear stresses, the Cauchy stress tensor $[\boldsymbol{\sigma}]$ is obtained in the following manner:

$$[\boldsymbol{\sigma}] = \begin{bmatrix} \sigma_{xx} & \sigma_{xy} & \sigma_{xz} \\ \sigma_{yx} & \sigma_{yy} & \sigma_{yz} \\ \sigma_{zx} & \sigma_{zy} & \sigma_{zz} \end{bmatrix}.$$

Since the model has no translation or rotation, the equilibrium equation for the body at rest is represented in COMSOL Multiphysics as the following:

$$\mathbf{f}_V + \nabla[\boldsymbol{\sigma}] = 0$$

For the linear elastic material the total strain tensor is written in terms of the displacement gradient, as noted in the equation below.

$$\varepsilon = \frac{1}{2}[(\nabla\mathbf{u})^T + (\nabla\mathbf{u})]$$

The thin membrane of the CMUT exhibits large deflection, as governed by the theory of plates and shells. The theory states that a membrane that deflects approximately more than 20% of its own thickness exhibits what's referred to as a "large deflection" [72]. In the COMSOL GUI, the large deformation can be accounted for by including geometric nonlinearity within the linear elastic material.

Mechanical Field Boundary Conditions

In the Solid Mechanics physics domain for the COMSOL model, the air domain is deactivated from any calculation or consideration due to the fact that air is not a solid material. As for volume conditions, unlike silicon nitride membranes, parylene membranes do not have residual stresses to account for, although doing so can be properly achieved in COMSOL Multiphysics. Thus, no prestress is accounted for. The solid mechanics surface boundary conditions enable much of the multiphysics domain coupling. The surface area force, mainly from the electrostatic attraction between the parallel electrodes, is applied to the very bottom surface boundary of the membrane. The equation below shows the relationship between the stress and the user applied surface force, which is necessary for COMSOL to numerically compute the significance of the electrostatic to the structural mechanics of the CMUT device:

$$\sigma \cdot \mathbf{n} = \mathbf{F}_A,$$

where σ is the stress, $\mathbf{n}$ is the normal direction, and $\mathbf{F}_A$ (N/m^2)is the user defined surface area force. The figure below demonstrates the boundary that carries the electrostatic force surface load, along with all other boundary conditions required in the solid mechanics domain.
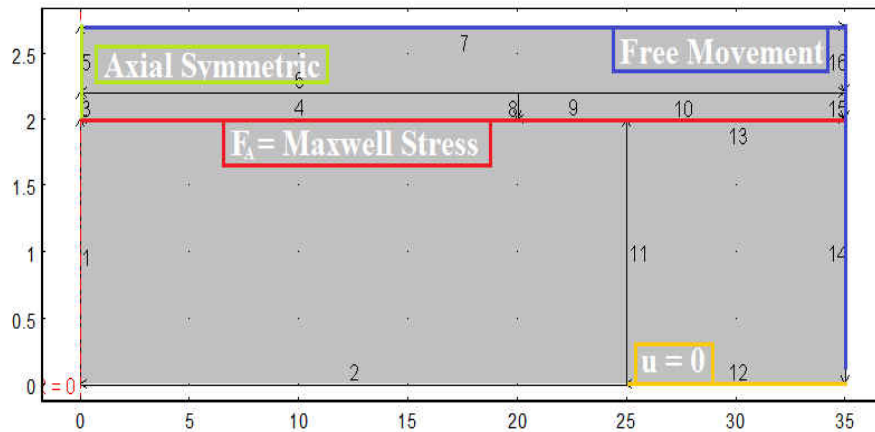
Figure 39: Boundary load of the electrostatic attraction between the parallel electrodes

An assumption made in modeling this work is that the connection of the post to the substrate is immovable, thus the boundary condition is fixed. This condition is satisfied by the equation $\mathbf{u} = 0$, where $\mathbf{u}$ is the displacement field consisting of both the vertical and horizontal motion components. Axial symmetry of the model is indicated in the solid mechanics domain. COMSOL assumes the boundary indicated for axial symmetry will be revolved around that axis.

Moving Mesh

The CMUT model calculates electrostatic fields with the aid of finite elements. In the case of electrostatic deflection, these finite elements remain in the same position as the membrane deflects. The membrane comes into contact and passes through the fixed mesh consisting of non-structural areas. The result of these two meshes superimposed and tangled over each other is numerical inaccuracy of the solution. To overcome this scenario, a mesh that

can update position as deformation occurs is required. The Arbitrary Lagrangian-Eulerian (ALE) is the method of choice, as this Moving Mesh can automatically account for the deformation of both the structure and the air without having to remesh for every iteration of input voltage [73].

It is necessary to set up boundary and domain conditions for the moving mesh. The assumption in modeling is that the bottom of the geometry will remain stationary (i.e., strict adhesion to the substrate). In the axial symmetric modeling, this is accounted for by setting the boundary constraint to $dr = 0$ and $dz = 0$, where dr and dz indicate mesh displacement. This ensures zero displacement of the mesh. Although by theory the bottom of the post will need a zero displacement condition, the constraint has already been met in the set-up of the solid mechanics domain. The structural volume is modeled as having a preset displacement of $dr = u$ and $dz = w$, where u and w are the displacements calculated from the solid mechanics domain to be coupled into the moving mesh. The air volume (or any other fluid medium) is modeled as having free displacement. Free displacement represents a "no constraint" condition. In the case of two volumes that share a boundary, it is necessary to define the intended boundary condition. In the case of the CMUT, the air gap shares a boundary with the bottom of the membrane. The required condition is that $dr = u$ and $dz = w$.
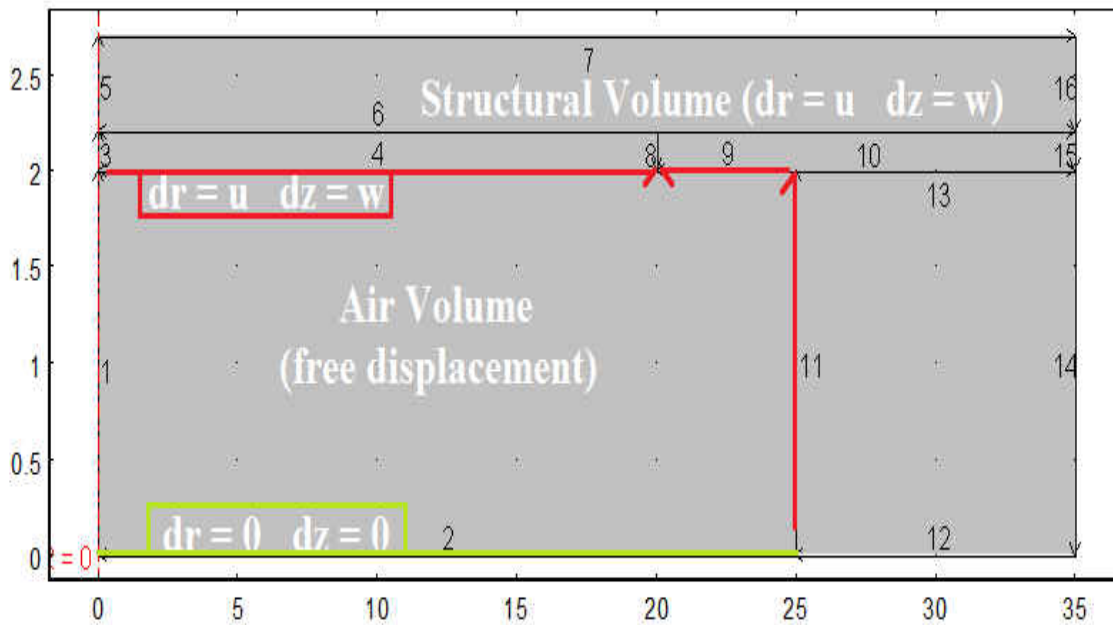
Figure 40: Moving Mesh boundary conditions

The meshing of the model is performed using a mapped mesh. The mapped mesh serves the purpose of extremely reducing the node size of the problem, and gaining control of mesh density at specified locations. The mapped mesh, as opposed to the free mesh, does not propagate freely throughout the model. Thus the user has much control over the quantity of elements in the model. The downside to the mapped mesh is the necessity for more mesh boundaries to be required, the mesh distribution on the boundary must match up to neighboring geometries correctly, and the geometry must match the shape of the element.

The advantage of 2D axial symmetric versus 3D modeling is the fact that the COMSOL numerical solver has less elements to solve for in the problem. In the case of an extremely thin (relative to neighboring geometries) graphene electrode, mapped meshing exceptionally simplifies the number of elements needed by adding in a suitable distribution, as opposed to a free mesh.
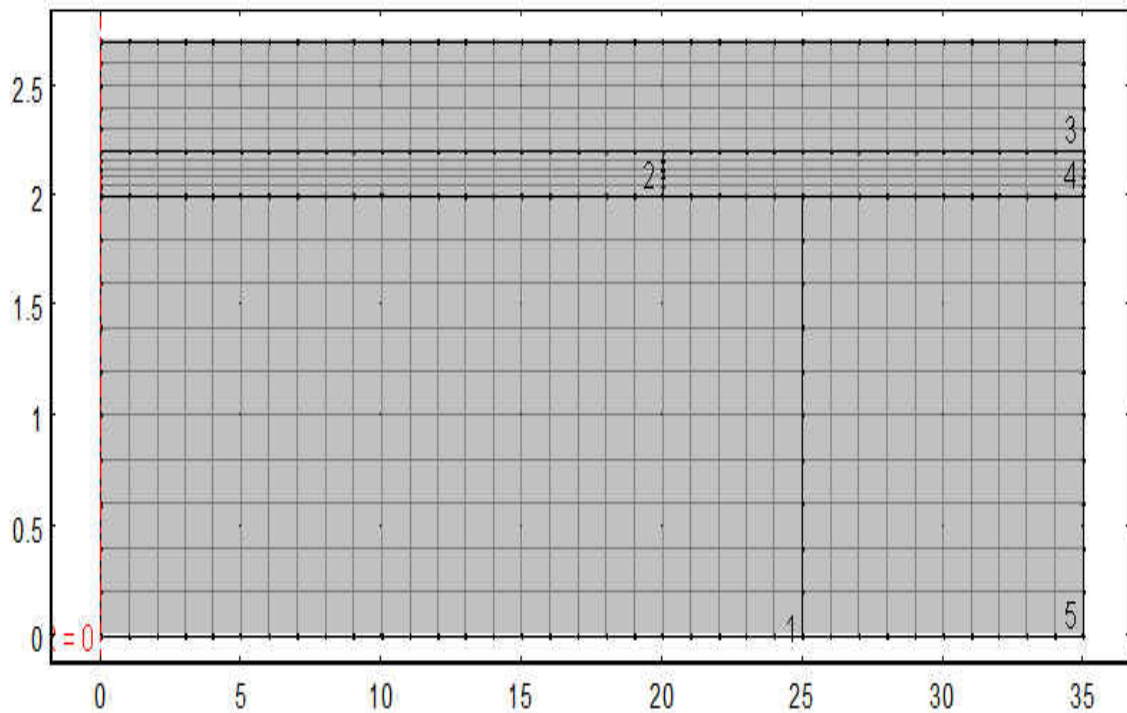
Figure 41: Mapped mesh of CMUT Parylene

Electrostatics Field

In COMSOL Multiphysics, electrostatics is considered and added into the physical model due to the voltage input requirement and capacitance change necessary to determine sensitivity and ultimately differentiate targeted structures to form an image.

Electrostatics Field General Equations

In the electromagnetic domain, the physics is governed by the following Maxwell equations in partial differential equation form:

$$\nabla \times \mathbf{H} = \mathbf{J} + \frac{\partial \mathbf{D}}{\partial t}$$

$$\nabla \times \mathbf{E} = -\frac{\partial \mathbf{B}}{\partial t}$$

$$\nabla \times \mathbf{D} = q_e$$

$$\nabla \times \mathbf{B} = 0$$

where $\mathbf{E}$ (V/m) is electric field intensity, $\mathbf{D}$ (C/m^2) is electric flux density, $\mathbf{H}$ (A/m) is magnetic field intensity, $\mathbf{B}$ is magnetic flux density, $\mathbf{J}$ (A/m^2) is current density, and q_e (C/m^3) is the space charge density. Additionally, for solvability the following constitutive equation is added:

$$\mathbf{D} = \varepsilon \mathbf{E} = \varepsilon_0 \mathbf{E} + \mathbf{P},$$

where $\mathbf{P}$ (C/m^2) is the electric polarization vector. Relating the electric flux density to the polarization and electric field intensity helps to introduce the variable for permittivity of vacuum ε_0 (). For the electrostatic case, physical quantities are not dependent on time, and thus the Maxwell equations can be reduced to the following:

$$\nabla \,\text{X}\, \mathbf{E} = \ 0$$

$$\nabla \,\text{X}\, \mathbf{D} = q_e$$

Due to the fact that the curl of the electric field intensity E equals zero in a static case, E can be represented by the electric scalar potential V_e in the following manner:

$$\mathbf{E} = \ -\nabla V_e.$$

By combining the constitutive equation with the electrostatic representation of Maxwell's equations, Gauss's law can be described in the following form:

$$-\nabla \cdot (\varepsilon_0 \nabla V_e - \mathbf{P}) = q_e$$

In the case of an in-plane 2D model, the COMSOL's electrostatic module assumes symmetry for solutions that vary in the x and y directions, and is constant in the z direction.

In a general CMUT model, or any parallel plate capacitor, the static voltage input causes a static deflection of the membrane. In numerical analysis this phenomenon can be modeled by various different methods (i.e. principal of virtual work, etc). COMSOL Multiphysics models this as a Maxwell stress tensor. The Maxwell stress tensor represents the net flow of

momentum across the surface at a point. To compute the force exerted on the boundary, the integral is taken across the structural membrane active in the electrostatic domain.   In calculating the necessary force, it is noted that the total magnetic force acting on a volume equals the integral of the force density with respect to the volume, as noted the equation below.

$$F = \int_V \mathbf{f} \, dV$$

Furthermore, Maxwell [source] has shown that the magnetic force density equals the divergence of a tensor, **T**. This tensor **T** is denoted as the Maxwell stress tensor. To effectively utilize this tensor as an approximation of the electric force to be coupled into the structural mechanics domain in COMSOL, the Maxwell stress tensor and a unit vector normal to the surface pointing outward from geometric volume, **n**, are multiplied. This relationship, noted as **T** $\cdot$ **n**, forms the magnetostatic stress exerted on the surface. In COMSOL notation, the force is calculated by integrating the Maxwell stress tensor over the surface of the membrane, and the equation is shown below.

$$\mathbf{n_1} T_2 = -\frac{1}{2} \mathbf{n_1} (\mathbf{E} \cdot \mathbf{D}) + (\mathbf{n_1} \cdot \mathbf{E}) \mathbf{D}^T$$

The capacitance of the CMUT system at a certain deflection can be calculated from the surface integral of the total surface charge, which is noted as electric flux density **D** (C/m^2). The

capacitance changes with more electrode area in a closer proximity to the ground. The simplified equation of capacitance is as follows:

$$C = \varepsilon_r \varepsilon_0 \frac{A}{d},$$

where C is the capacitance, ε_r is the dielectric constant of the material (or medium), ε_0 is the electric constant ($\varepsilon_0 \approx 8.854 \times 10^{12} \ \mathrm{Fm^{-1}}$), and d is the distance between the electrodes. In COMSOL, the capacitance of the system is derived by the surface integral of the electric energy density (W_e) in the following manner:

$$C_{ii} = 2 \int_\Omega W_e \ d\Omega,$$

where *i* indicates the port number to be used in the Terminal boundary condition. For the models developed in this work, the Terminal port boundary was not used. Instead, a post-processing of the electrostatic results is all that is necessary to determine the capacitance change with respect to membrane deflection.

Electrostatics Field Boundary Conditions

Important boundary conditions in the COMSOL electrostatics module to consider in this model are: continuity, zero charge, ground, and electric potential. When the geometric volumes interface with each other (i.e. Parylene membrane to air, etc.), COMSOL uses the following surface interface condition with respect to defining a general boundary equation when considering these boundary conditions:

$$\mathbf{n}_2(\mathbf{D}_1 - \mathbf{D}_2) = q_e \,,$$

and with no surface charge, the equation is rewritten in COMSOL Multiphysics as

$$\mathbf{n}_2(\mathbf{D}_1 - \mathbf{D}_2) = \mathbf{n}\left[(\varepsilon_0\,\nabla\,V_e - \mathbf{P})_1 - (\varepsilon_0\,\nabla\,V_e - \mathbf{P})_2\right] = 0,$$

where $\mathbf{D}_1$ and $\mathbf{D}_2$ indicate the different domains at the boundary of interest.

The ground node in COMSOL indicates that there is zero electric potential on the boundary's surface. This boundary condition in equation form can be written as V = 0. Similarly the electric potential equation simply accounts for the input voltage V = V_0, where V_0 is the user input voltage potential. Very important in the case of an electrode is to consider the electrical boundary conditions around the geometry. To effectively model the CMUT, the electrode boundary will be surrounded by an electrical voltage input, as noted below in Figure 42. This is justified due to the fact that the entire electrode receives an input voltage. The entire volume for the metal electrode is deactivated when considering the electrostatic module. This is due to the fact that there is no dielectric constant for metals.
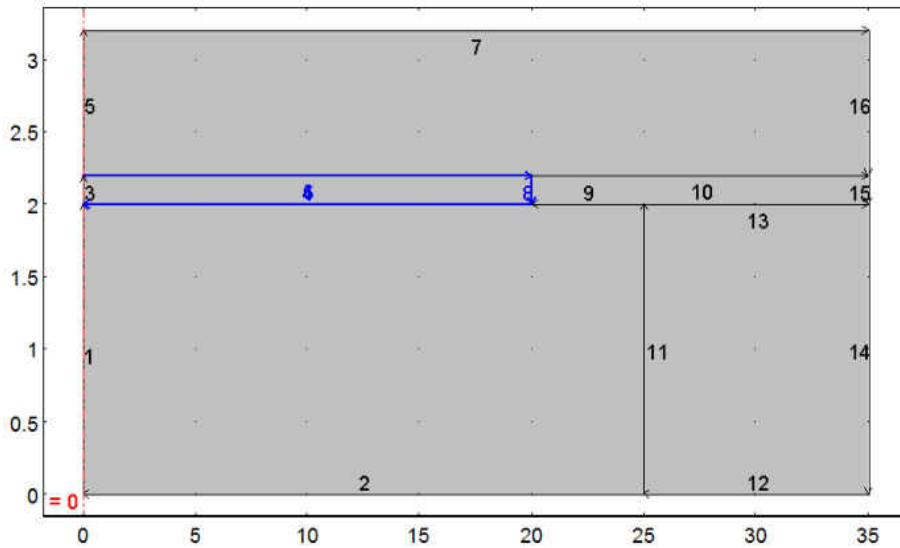
Figure 42: Electrode boundaries that have the requirement of V = V_0 for voltage input

For a boundary interface between two geometric domains active in the electrostatics module, it is required to consider the case for continuity between materials that have similar or different dielectric constants. The continuity condition is defined as

$$\mathbf{n} \cdot (\mathbf{D}_1 - \mathbf{D}_2) = 0,$$

where $\mathbf{D}_1$ and $\mathbf{D}_2$ indicate the different domains at the boundary of interest. For the portion of the model that does not have a boundary that can interface with two different geometries (i.e., top or side of model), the boundary condition of $\mathbf{n} \cdot \mathbf{D} = 0$ is used to indicate zero charge. Figure 43 below demonstrates the concept of applying the boundary condition of zero charge, and Figure 44 shows the ground potential boundary placement.
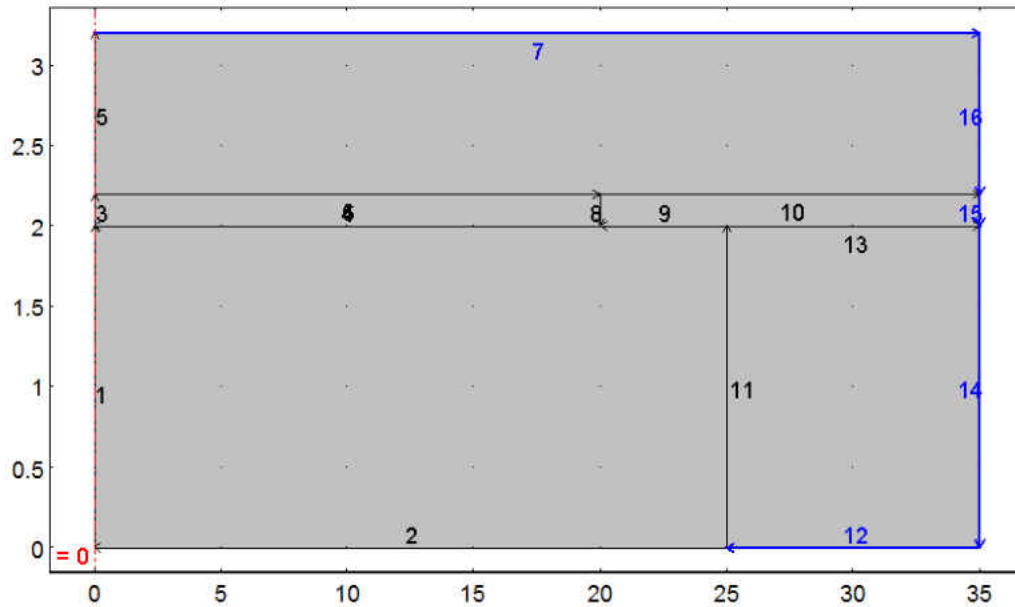
Figure 43: Necessary boundaries (highlighted in blue) to apply zero-charge due to boundary only having 1 interface material
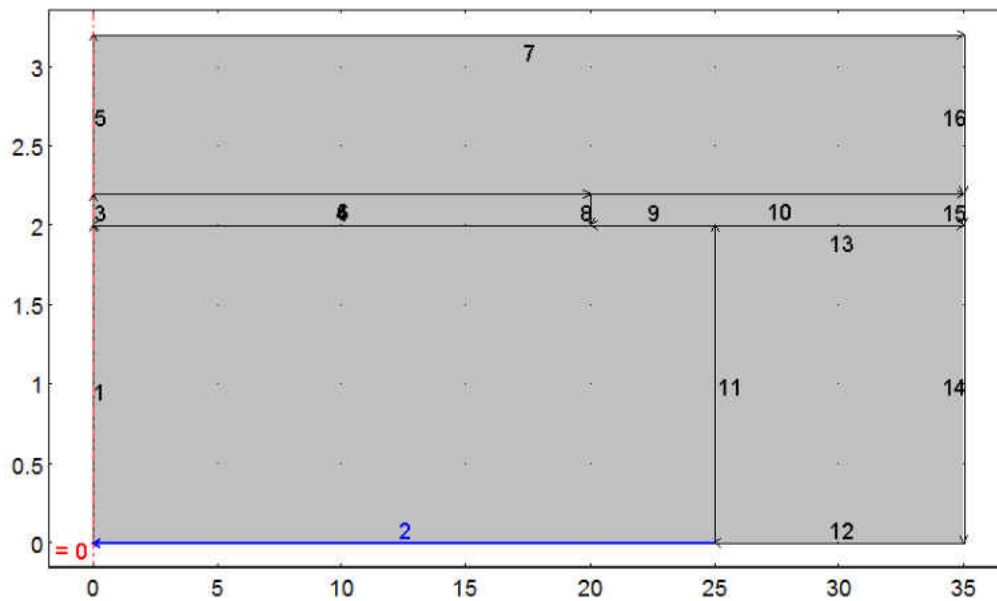
Figure 44: Ground electrical boundary condition

CHAPTER FIVE:
RESULTS

In this chapter, the novel Parylene-C/Graphene CMUT is compared to the Silicon/SiO2 CMUT in terms of flexibility, transmission output pressure, and receive sensitivity. To design the CMUT cell for the Parylene-C/Graphene membrane material, a parametric study of cell parameters and its effects on performance characterization is observed. First a cell composed of only Parylene-C as the membrane material is analyzed in a parametric study as a function of both changing cell diameter and membrane thickness. The second parametric study separately observes a CMUT cell composed entirely of grapheme layers as the only membrane material, and the parameters of interest are the CMUT performances due to changing cell diameter as well as a range of grapheme sheets (between 5-100 0.34nm thick layers). The last parametric study focuses on the combined effects of both the Parylene-C membrane and the thin sheets of grapheme electrode. The three parameters of interest in this combined case are the changing cell diameters, a range of membrane thicknesses, and a range of grapheme sheets as the upper electrode.

To ensure a fair comparison between traditional CMUTs (Silicon/SiO2) and our novel CMUT (Parylene-C/Graphene), the center frequency in vegetable oil was chosen to be a constant of about 7.1 MHz, the cell diameter was held constant at 30 μm, and the post width was defined as being 5 μm wide. Upon settling on an optimized Parylene-C/Graphene cell design, the Silicon/SiO2 membrane cells are compared the Parylene-C/Graphene CMUT by

studying static operation, dynamic operation, as well as characterizing in the frequency domain.

Studies performed include: DC collapse voltage, center frequency shift as a function of applied bias voltage, membrane deflection profile per DC static bias voltage, static volume deflection over the surface of the membrane with increasing DC voltage, capacitance change per static DC voltage increase, dynamic sensitivity of membrane and change in total electrode surface charge from an incoming pressure wave, and time-harmonic pressure output into the vegetable oil medium with different DC bias voltages and AC voltages.

<center>Parametric Study- Parylene-C</center>

Parylene-C as the only membrane was varied as a function of cell diameter and membrane thickness.   The upper electrode was placed on the bottom surface of the membrane, and a boundary condition was applied to indicate an input voltage, so as to avoid using a structural metal in this study.   Figure 45 below shows the center frequency of the Parylene-C cell structure (membrane and post) with the changing parameters.

Figure 45: CMUT cell center frequency parametric study of Parylene-C as the only membrane material, without any structural metal material acting as an upper electrode. The parameters consist of cell diameters (range of 10-30 μm) as well as Parylene-C membrane thickness (1-5 μm).

It is evident from Figure 45 above that as the cell diameter decreases, the stiffness and thus the center frequency of the cell structure increases. The degree of the frequency change as a function of cell diameter is most noted in the smaller diameter range.   There is approximately a 77% shift in center frequency between the cell diameters of 10 μm and 16 μm when focusing on a membrane thickness of 4 μm. Likewise, the degree of the frequency change as a function of cell diameter becomes much smaller as the diameter of the cell becomes larger. The shift in center frequency, when focused on a 4 μm parylene-C membrane thickness, is only 42%.

The parylene-C membrane thickness also contributes heavily to the shift in center frequency, and depending on the size of the cell diameter, can have a heavy influence in it change. For the extreme case of a parylene-C membrane cell having a diameter of 10 μm, the slope of the curve in Figure 45 as the thickness increases is more apparent than the in the other diameters on the same plot. Table 2 lists the slope of each diameter as well as the percentage (%) shift in center frequency for the plot in Figure 45.

Table 2: Slope corresponding to each diameter, according to the plot in Figure 45 of the parametric function of center frequency for various parylene-C membrane thicknesses and cell diameters. It is evident that the smaller the membrane diameter is, the larger the effect of center frequency change will be.

Diameter	Linear Slope
10 μm	12.73
16 μm	7.35
20 μm	5.31
24 μm	3.98
30 μm	2.74

An important point in using Figure 45 to determine desired cell parameters is the observation that as the thickness becomes larger, the effect of increasing the thickness as a means to increase the center frequency of the cell diminishes. This is evident in the parabolic-

shaped curves, and their gradual transition from higher slopes to lower slopes. All of the different sized diameters exhibited an eventual resistance to increased frequency with increasing membrane thickness, thus there exists an optimal thickness at which a desired frequency can be achieved without increasing the thickness and eventually collapse voltage.

The collapse voltage is also another important feature in CMUT cell design, and has also been parametrically solved for as a function of both a parylene-C membrane thickness and cell diameter, similar to the results in Figure 45. The plot for the collapse voltage is mapped out in Figure 46 below.
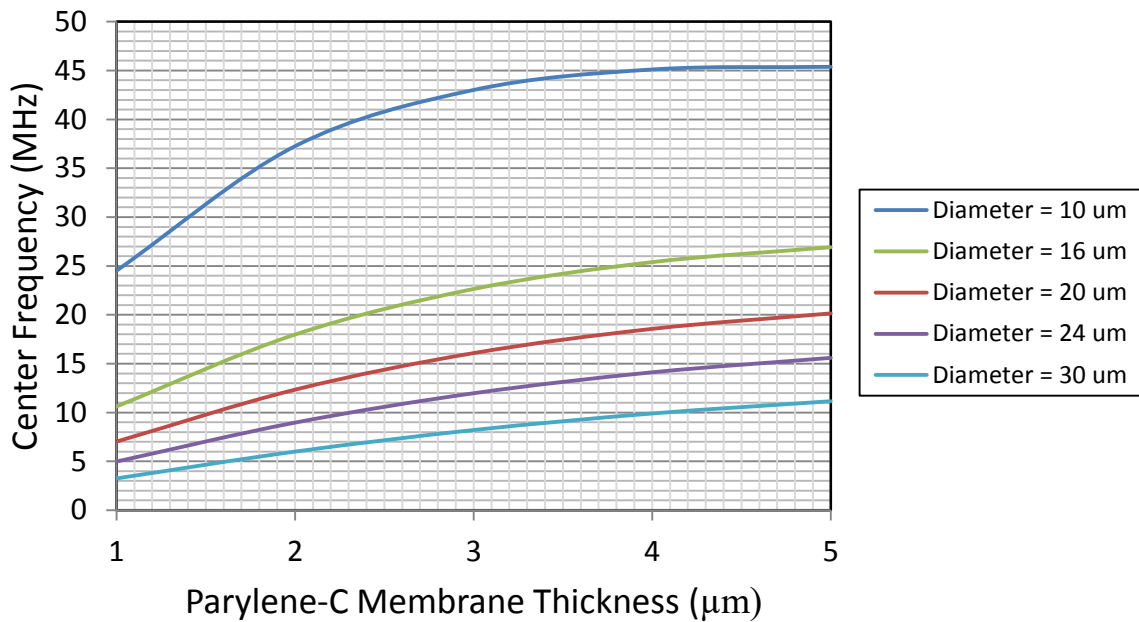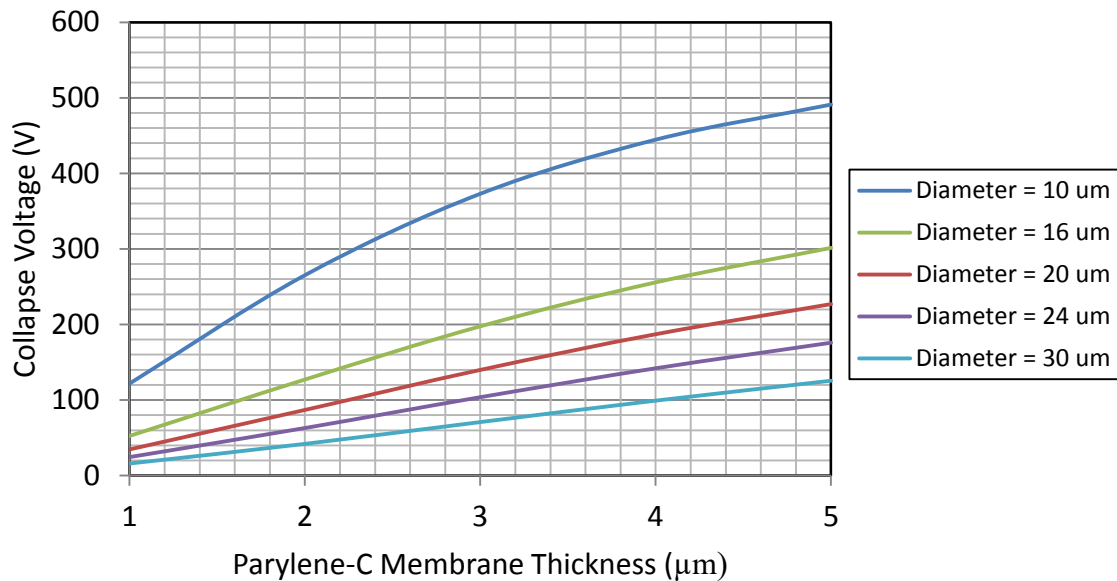

Figure 46: DC collapse voltage parametric study of Parylene-C as the only membrane material, without any structural metal material acting as an upper electrode. The parameters consist of cell diameters (range of 10-30 μm) as well as Parylene-C membrane thickness (1-5 μm).

Unlike the eventual zero slope that was seen in the curves of the center frequency in Figure 45, the collapse voltage in Figure 46 continues to increase almost at the same slope, for both lower thicknesses and higher thicknesses. This shows that there is an optimal point at which the increase in membrane thickness adds more voltage requirement than it adds center frequency/stiffness.

The collapse voltage for smaller diameters exhibits a parabolic relationship with increasing membrane thickness. As the diameter is increased, this severity of change is reduced and ultimately transitions from a parabolic relationship into a linear relationship for an increase in parylene-C membrane thickness.

Parametric Study- Graphene Sheets Only

To demonstrate the contribution of the grapheme layers to the overall Parylene-C/Graphene CMUT, a parametric study of a membrane consisting only of grapheme layers was conducted. The parameters to adjust in this study included only the number of grapheme layers (0.34nm each) and the cell diameter. Figure 47 below demonstrates the parametric relationship between the numbers of graphene sheets versus the cell diameter.
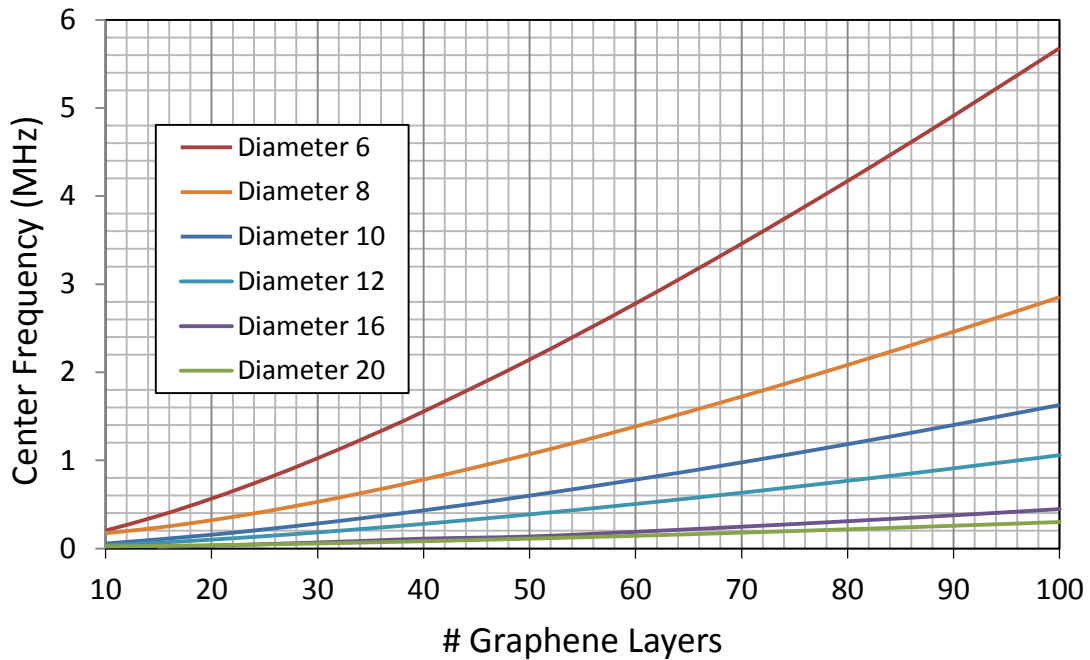
Figure 47: Center frequency parametrically solved for a CMUT consisting only of graphene sheets. The center frequency is solved as a function of the number of grapheme sheets and the diameter of the cell. The effects of increasing cell stiffness/frequency diminishes as the diameter of the cell becomes larger.

It is evident that as the diameter of the cell decreases, so does the effect of increasing the number of graphene sheets to gain a higher center frequency. This can be quantified by observing the slope of each diameter plotted in Figure 47. The smallest diameter (6 µm) has a slope relatively larger than the largest diameter (20 µm) cell. Although a smaller cell diameter would make a convenient choice, there are transducer limitations that are a trade-off and must be avoided, include an increase in parasitic capacitance and lower pressure output per cell.

Parametric Solving for Parylene-C/Graphene membrane

The complete observation of a parylene-C/graphene membrane CMUT has been

mapped out as a function of three parameters, including the number of graphene layers, the

diameter of the membrane, and the thickness of the parylene-C membrane. This 3D plot is

illustrated below in Figure 48. These parameters were solved for the total DC collapse voltage,

as well as the center frequency of the device. The importance of solving these parameters is to

map out the parameters for future redesign to a desired center frequency or collapse voltage.
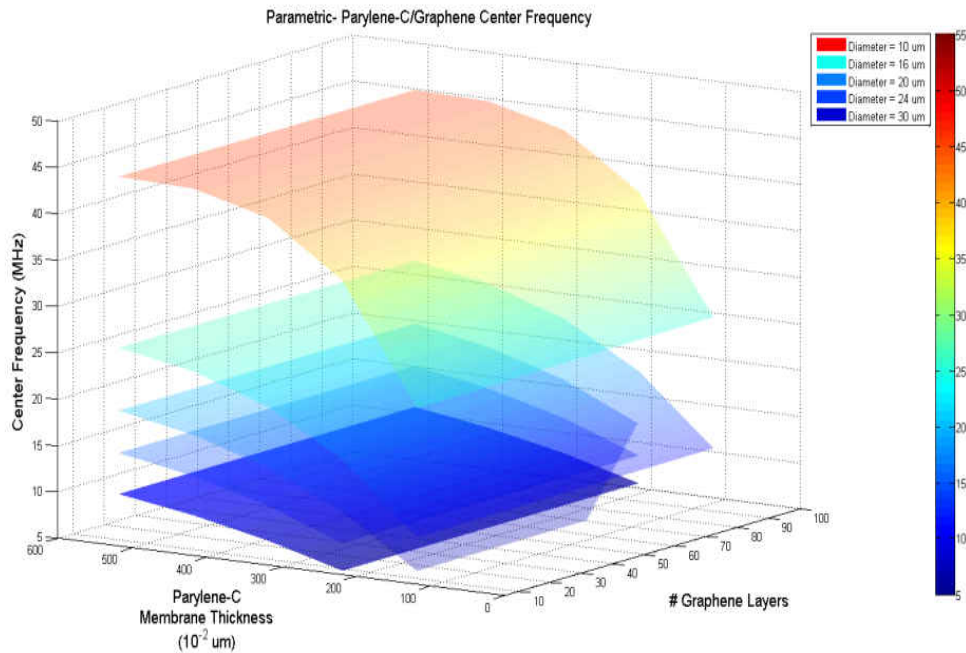
Figure 48: 3D Collapse voltage plot of Parylene-C/Graphene CMUT membrane. Voltage solved parametrically as a function of parylene-C membrane thickness, graphene layers, and cell diameter. The different plot layers indicate the effects of using different sized membrane diameters.

The center frequency plot in Figure 48 above and the collapse voltage plot below in Figure 49 bears resemblance to the individual plots of parylene-C membrane and the graphene membrane in terms of showing the same general trend. As either the cell diameter decreases or the parylene-C membrane thickness increases, so does the center frequency and collapse voltage (shown in Figure 49). Likewise only very small diameter cells exhibit any difference when the number of graphene sheets is altered.
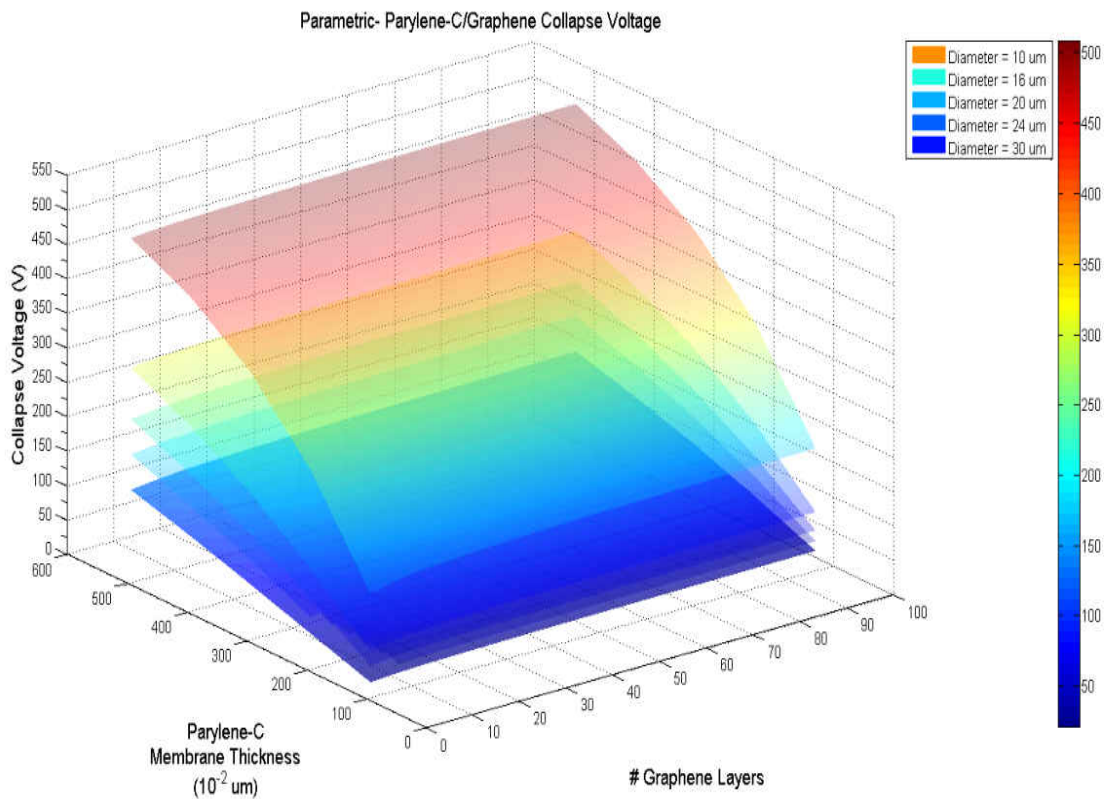
Figure 49: 3D Collapse voltage plot of Parylene-C/Graphene CMUT membrane. Voltage solved parametrically as a function of parylene-C membrane thickness, graphene layers, and cell diameter. The different plot layers indicate the effects of using different sized membrane diameters.

From the parametric results, Parylene-C/Graphene membrane CMUT cells with the following dimensions were chosen and are shown in Table 3 below along with the chosen parameters for the traditional silicon membrane with silicon dioxide posts. Figure 50 below illustrates the CMUT cell geometry to which these dimensions will be applied to.

Table 3: Design parameters for both the Parylene-C/Graphene membrane cell as well as the traditional Silicon/SiO$_2$ membrane CMUT cell.

	Parylene-C/Graphene	Silicon/SiO$_2$
Membrane thickness	4.0 µm	0.95 µm
# Graphene Sheets	30	___
Membrane Diameter	30 µm	30 µm
Gap Height	0.25 µm	0.25 µm
Post Width	5 µm	5 µm
Collapse Voltage	118 V	103 V
Center Frequency (in oil)	7.1 MHz	7.1 MHz
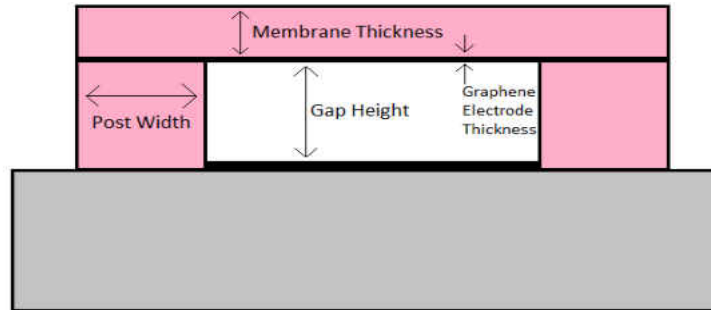
Figure 50: CMUT cell geometry with associated dimensions of interest

The main factors in conducting a fair study between the two different CMUT membrane materials is to obtain a structure that exhibits the same operating frequency as well as the same diameter. This allows for a fair comparison in investigating the capacitance change sensitivity, as well as the pressure output from the membrane. Both quantities rely heavily on the surface area of the membrane.

The final CMUT geometries are visible below in Figure 50 and Figure 51. The image gives an idea of how thick the parylene-C/graphene cell is relative to the Silicon/SiO$_2$ cell.
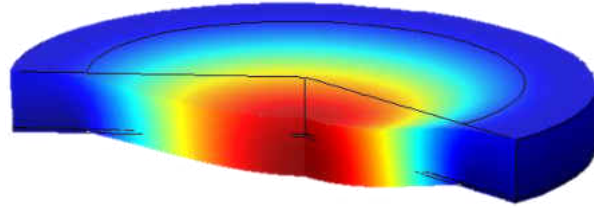
Figure 51: Parylene-C/Graphene CMUT cell with the dimensions described in Table 3. The parylene membrane is much thicker than the silicon membrane.
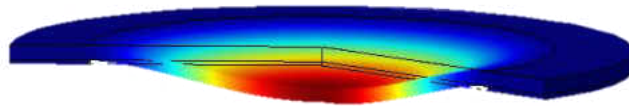
Figure 52: Silicon/SiO$_2$ CMUT cell with the dimensions described in Table 3. The thickness profile is much thinner than that of the Parylene-C/Graphene cell.

<u>Flexibility of the CMUT</u>

The static axial symmetric deflection for the CMUT cells at a DC bias voltage of 80% of the total collapse voltage is plotted and shown below in Figure 53., and the axial symmetric deflection profile of the Parylene-C/Graphene CMUT cell per bias voltage is shown in Figure 54.
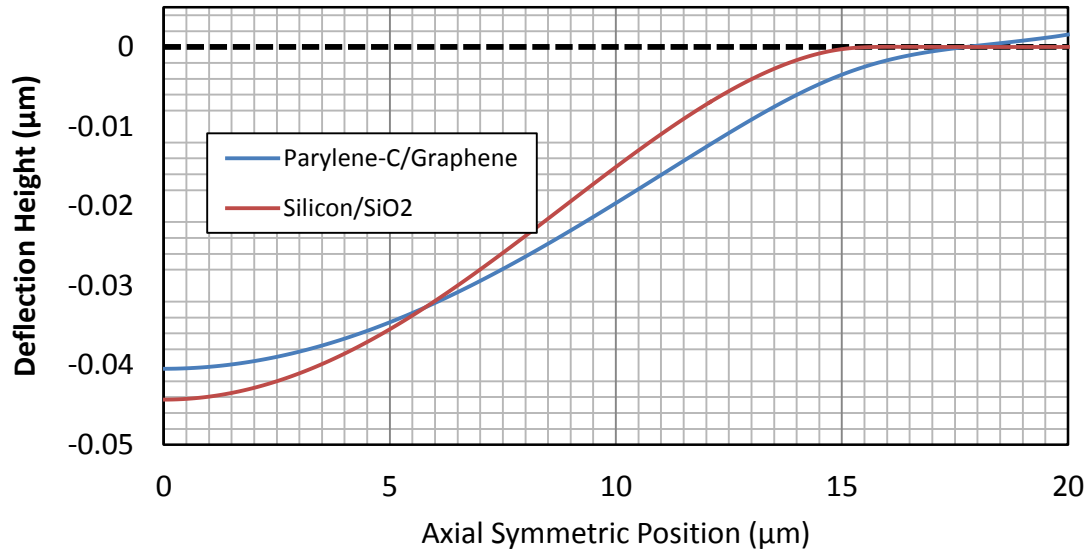
Figure 53: Axial symmetric deflection profile for the Parylene-C/Graphene CMUT cell and the Silicon/SiO$_2$ CMUT cell at 80% collapse voltage. The membrane radius is 15 μm, however the FEA data for the parylene-C membrane shows that the post is very flexible and thus adds extra deflection to the membrane overall.

The deflection height of zero means that the CMUT membrane is at the initial rest position. Finite Element Analysis provides insight into the shape of the membrane at different bias voltages. Figure 53 above shows that the post made of softer parylene-C polymer material exhibits much more flexibility, thus more overall deflection of the membrane. Note that the post begins at the axial symmetric radius position of 15 μm.
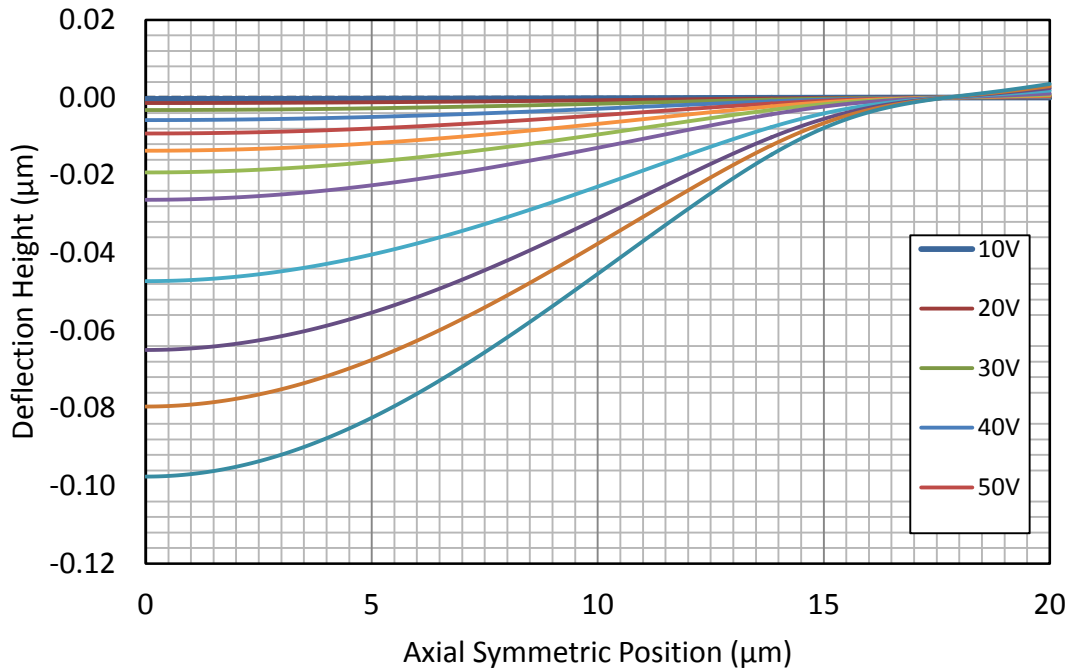
Figure 54: Axial symmetric membrane deflection profile for a Parylene-C/Graphene CMUT cell, with an increase in DC bias voltage.

It is difficult to make a certain conclusion about the flexibility of the CMUT cell simply based on the deflection profile plot of Figure 53. A better observation of flexibility may be observed from a plot of the volume displacement of the CMUT cell over the surface of the membrane. Figure 55 below demonstrates this point by plotting the static volume displacement as a function of bias voltage for both the Parylene-C/Graphene and the Silicon/SiO$_2$ CMUT cells.
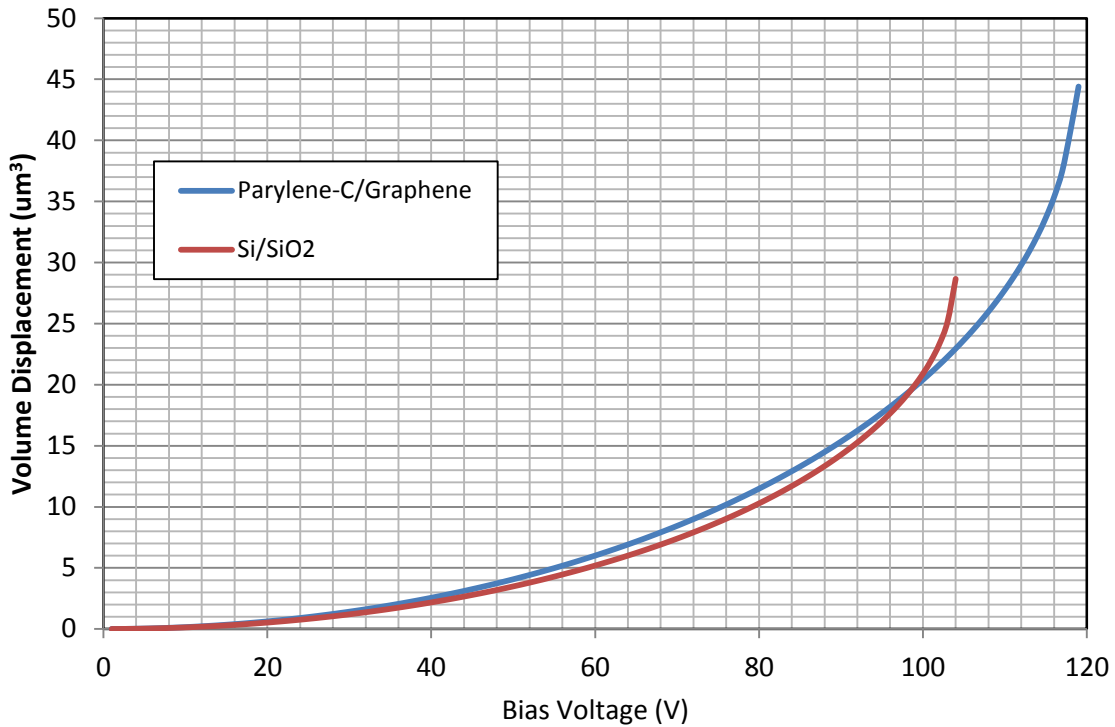
Figure 55: Plot of Static Volume Displacement as a function of applied DC Bias voltage for both the Parylene-C/Graphene CMUT and the Silicon/SiO$_2$ CMUT cell.

At final collapse voltage, the total volume displacement of the Parylene-C/Graphene cell was almost 45 μm^3, whereas the total volume displacement of the Silicon/SiO$_2$ CMUT cell was less than 30 μm^3. This represents an approximately 50% increase in volume displacement from the Silicon membrane cell to the Parylene-C/Graphene membrane cell. The plot in Figure 56 below normalizes the bias voltage to the form of percentage of collapse voltage.
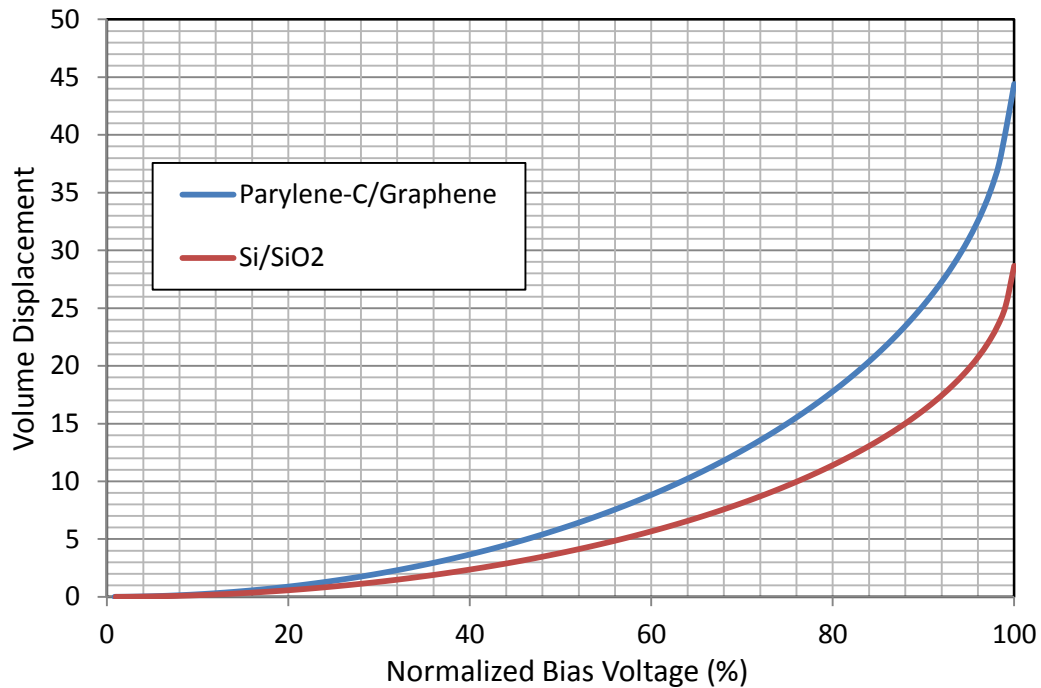
Figure 56: Normalized lot of Volume Displacement as a function of applied DC Bias voltage for both the Parylene-C/Graphene CMUT and the Silicon/SiO$_2$ CMUT cell. The bias voltage has been normalized to a percentage (%) of the total collapse voltage. This plot shows that the Parylene-C/Graphene CMUT cell has 55% more flexibility at 80% bias than does the Silicon/SiO$_2$ CMUT cell.

From the plot of Figure 56 above, it is clear that the Parylene-C/Graphene CMUT cell exhibits a constantly higher volume displacement of the membrane than does the Silicon/SiO$_2$ CMUT cell. At a bias voltage of 80%, the Parylene-C/Graphene cell exhibits a 55% increase in membrane volume displacement as compared to the Silicon/SiO$_2$ cell.

Sensitivity Analysis

A Gaussian point source wave was launched from a distance of 200 μm away from the surface of the membrane. The membranes were biased at 80% of collapse voltage, unless otherwise noted. The intensity of the wave was 5×10^{-5} m^3/s, with a frequency of 1 MHz and an impulse of 1 μs. The surface charge on the electrode was measured over the entire surface. As the wave strikes the membrane surface and causes the electrode to deflect closer to the bottom electrode, the surface charge over the electrode surface increases. This increase is ultimately characterized by a gray scale image shade on screen to form an ultrasound image. Figure 57 below shows the membrane's electrode response to an incoming wave for both CMUT materials.
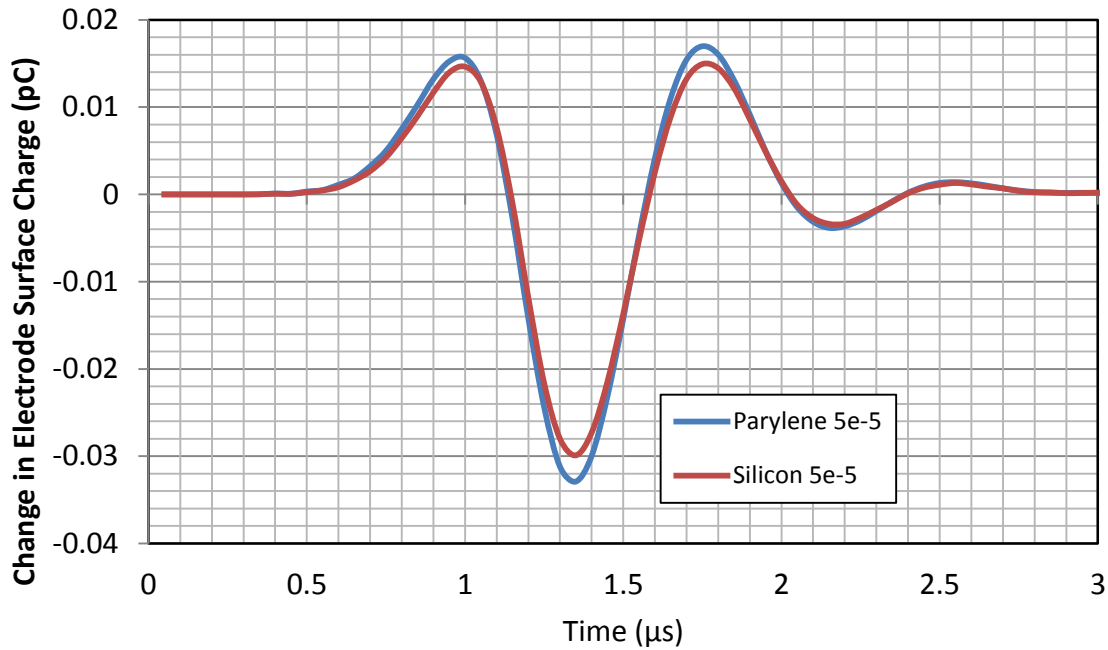
Figure 57: CMUT membrane sensitivity response to incoming pressure wave for the Parylene-C/Graphene CMUT and the Silicon/SiO$_2$ CMUT cell in oil. Cells biased at 80% of the collapse voltage. Change in surface charge over the electrode is recorded. Parylene-C/Graphene CMUT matches that of Silicon-based CMUT, and actually shows a 5% increase in initial response at around 1 μs.

The response of the Parylene-C/Graphene CMUT matches closely to that of the Silicon-based CMUT, and the initial response of the parylene-based cell shows a 7% increase in sensitivity over silicon at 1 μs. The change in surface charge over the electrode as time went by was used to calculate the response. The wave took a total time of about 0.5 μs to reach the membrane in the oil medium.
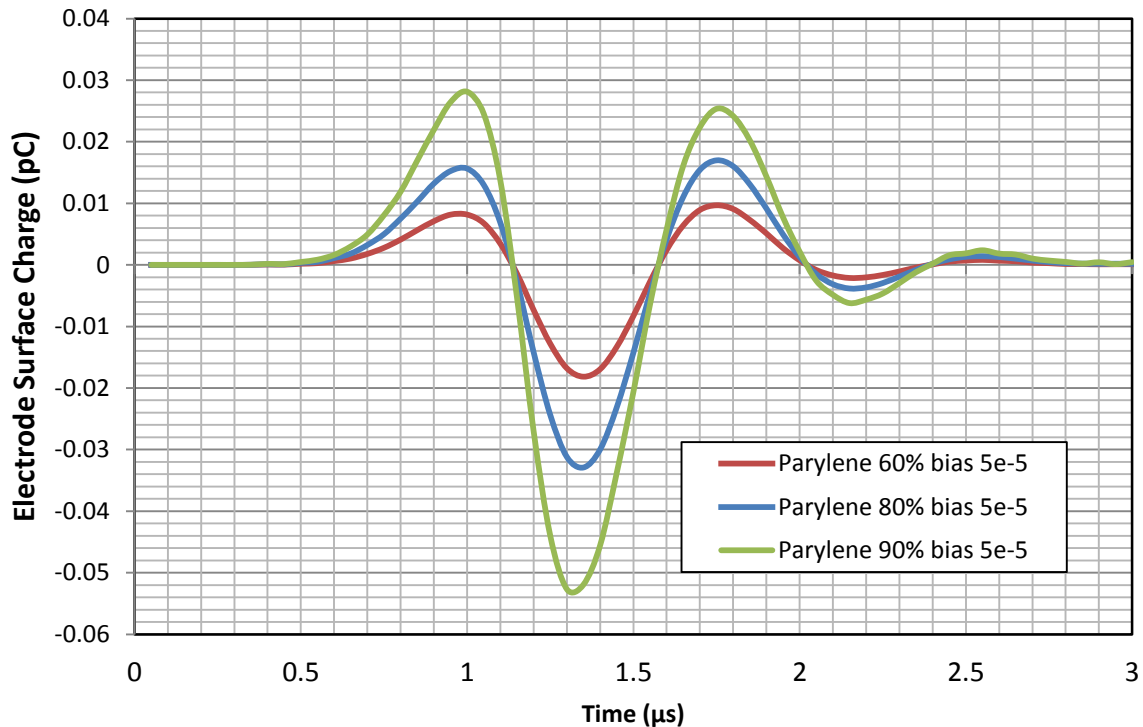
Figure 58: Sensitivity of Parylene-C/Graphene membrane in oil with different bias voltages to the same incoming pressure wave of intensity $5x10^{-5}$ m^3/s.

Normally CMUT cells are biased at 80-90% of their collapse voltages to exhibit the highest amount of sensitivity possible. Figure 58 above demonstrates the sensitivity of a Parylene-C/Graphene cell, and exactly why the membrane should be biased to the highest possible voltage. The higher bias DC voltage, as shown in the deflection profile above, leads to closer and closer distance between the membrane and bottom surface of the cell and more surface area of the membrane being in close proximity to the bottom electrode. Figure 59 demonstrates the relationship between silicon-based membrane response to bias voltages of

60%, 80%, and 90% of collapse. Increasing the bias from 60% to 80% leads to 30% higher sensitivity to an incoming wave. However increasing the bias voltage by only 10% from 80% to 90% yields 40% higher sensitivity to the incoming wave. This means that at higher DC bias voltages the receive sensitivity becomes much more responsive.
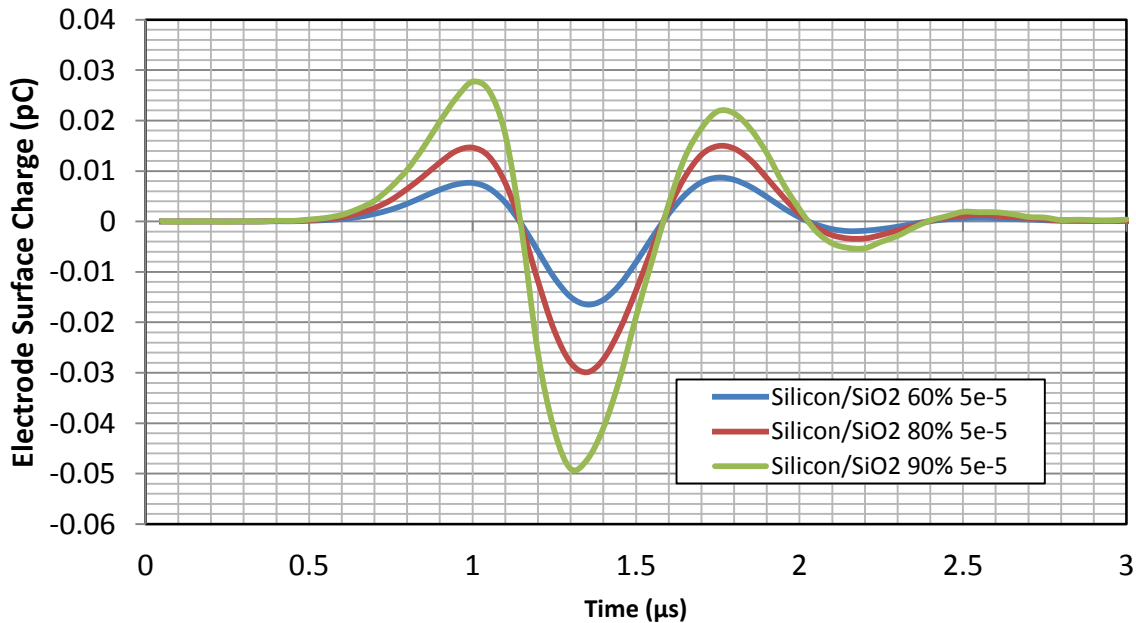
Figure 59: Sensitivity of Silicon/SiO$_2$ membrane with different bias voltages to the same incoming pressure wave of intensity 5x10^{-5} m^3/s..

Pressure output

During transmission pressure output operation of the CMUT cells, it is most beneficial to statically bias the cells at lower voltages. The membrane begins at a height farthest away from

the bottom of the CMUT surface and deflects downward with an AC voltage to achieve maximum membrane range of motion. Depending on the frequency at which this AC voltage is applied, there is an optimal range at which the cell exhibits a maximum pressure output. For the CMUT cell designs in this thesis, the membranes were biased at 60% of their collapse voltage, unless otherwise noted. In theory collapse of the CMUT in transient operation for an AC plus DC voltage would equal the static collapse voltage (103V for Silicon/SiO_2 and 118V for Parylene-C/Graphene), however in actuality transient dynamic motion of the CMUT implies that the maximum input voltage for a DC plus AC bias will be much lower due to the kinetic energy of the membrane as it is set in motion. For the case of a membrane biased at 60% of collapse voltage, a transient study was performed by giving an input voltage to the electrode, as noted in the equation below.

$$V(t) = V_{DC} + V_{AC} * \sin(2\pi f t)$$

It was determined from dynamic analysis that the Parylene-C/Graphene CMUT had a maximum of 52 Volts AC prior to collapse, whereas the Silicon/SiO_2 CMUT had a maximum of 46 Volts AC. For pressure transmission over the surface of the membrane, oil was used as the surrounding medium. Time-harmonic analysis was performed by conducting a frequency sweep of the maximum peak pressures. Figure 60 below shows the comparison of the Parylene-C/Graphene and the traditional Silicon/SiO_2 membrane cells. Both were biased to 60% of their collapse voltages and set to their maximum respective AC voltages.
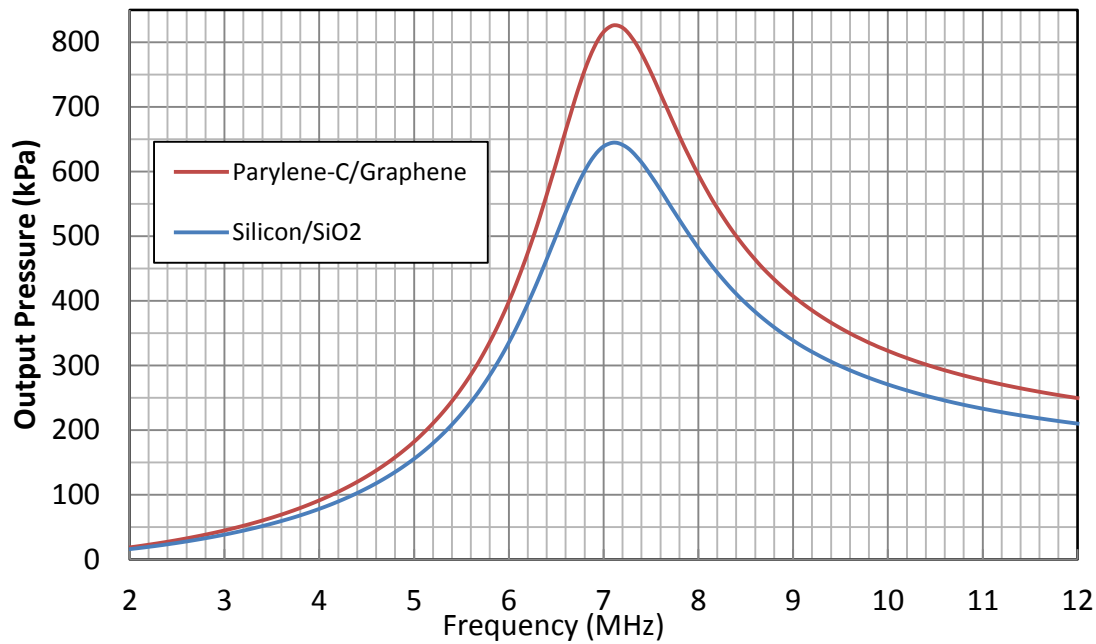
Figure 60: Frequency sweep of peak pressure output over the surface of the membrane. The cells were both biased to 60% of their collapse voltages, and set in motion by their maximum respective AC voltages.

The Parylene-C/Graphene membrane clearly exhibits higher peak output pressure over the membrane surface. The center frequency of both structures both equal to 7.1 MHz. This is where the CMUT is most efficient at converting mechanical motion into acoustic output. For the given DC and AC bias voltages, the Parylene-C/Graphene CMUT membrane exhibits a peak pressure over the membrane surface of almost 826 kPa. The Silicon/SiO$_2$ CMUT membrane only exhibits a peak output pressure over the membrane of about 644 kPa. This is an increase

of almost 30% higher transmission pressure for the Parylene-C/Graphene CMUT membrane, when compared to Silicon-based membrane.
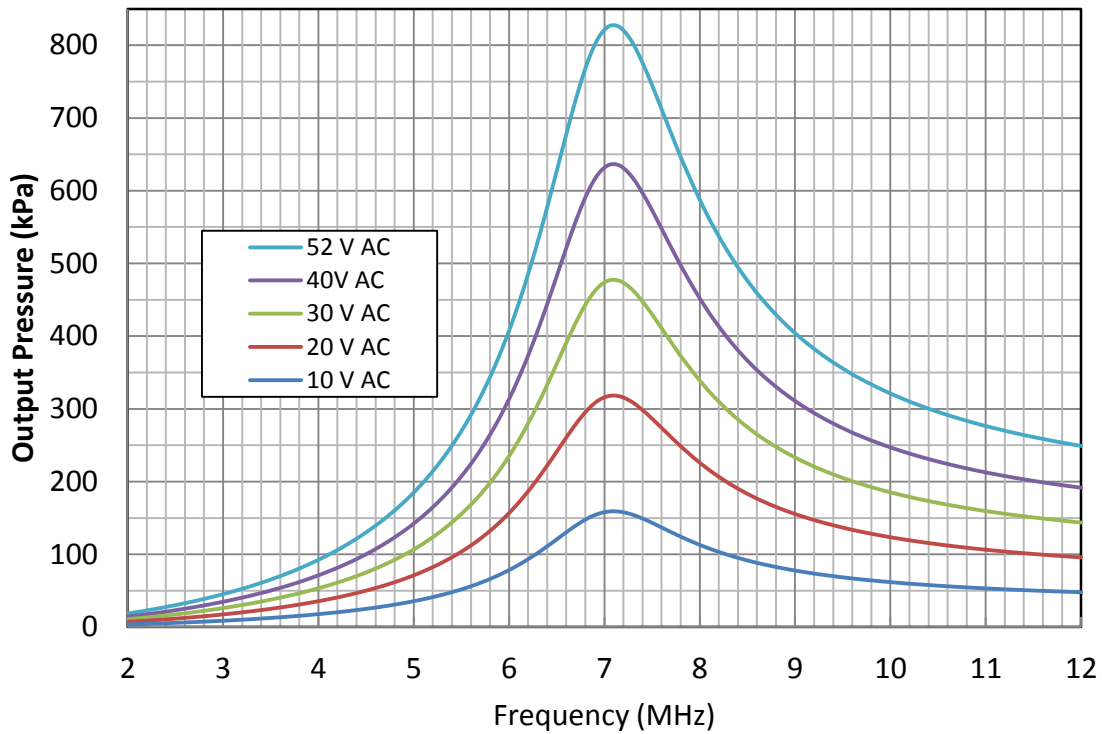
Figure 61: Peak Output Pressure over Parylene-C/Graphene Membrane at bias of 60% collapse voltage with increasing AC Voltage.

The output pressure is dependent upon both the DC bias voltage as well as the AC voltage superimposed. Lower AC voltages generate less dynamic range of motion of the membrane, thus leading to a lower pressure output. The plot in Figure 61 and Figure 62 demonstrates this point for both CMUT membranes.
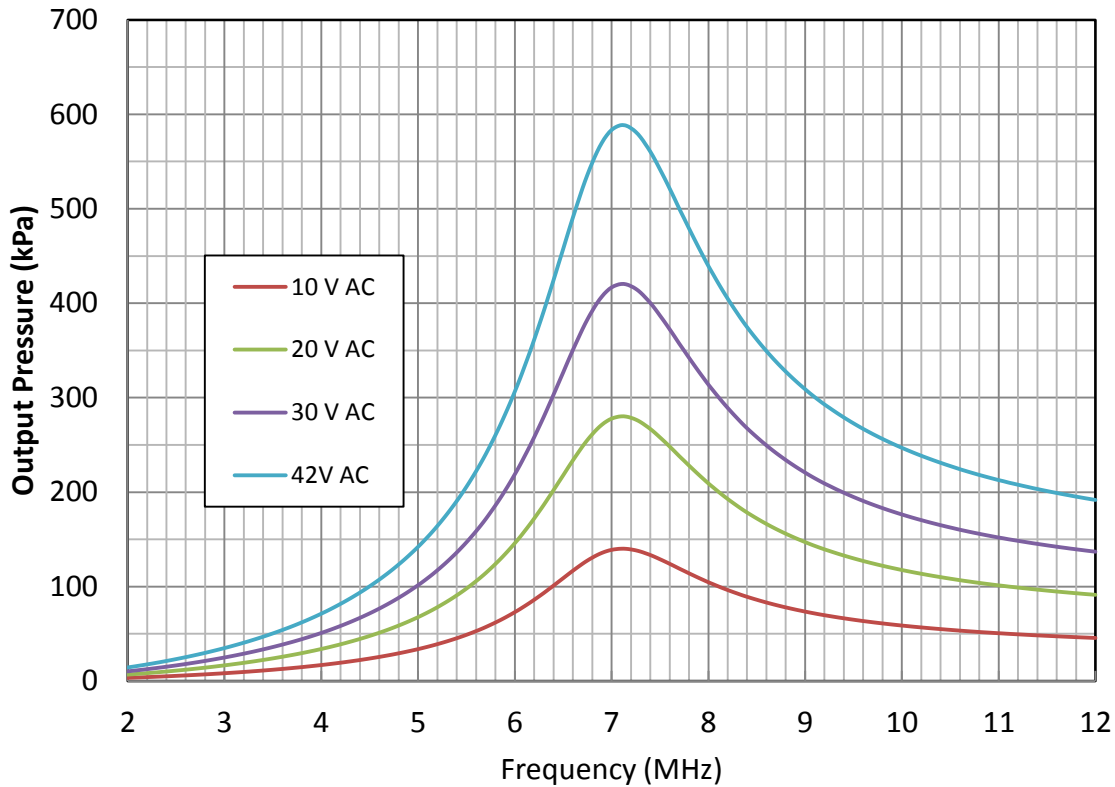
Figure 62: Peak Output Pressure over Si/SiO$_2$ Membrane at bias of 60% collapse voltage with increasing AC Voltage.

A comparison was made between the different CMUTs from the assumption of utilizing the maximum AC bias voltage prior to collapse. Another way to investigate which CMUT exhibits a higher pressure over the membrane surface is by examining the plots of Figure 61 and Figure 62 for the same AC of both cell structures, rather than their maximum possible AC amplitudes. It is evident that for the Parylene-C/Graphene membrane, there still exists a slightly larger peak pressure output over the membrane surface. In considering the case of a 60% DC bias voltage, the maximum peak pressure output for the Silicon/SiO$_2$ membrane with

an AC voltage of 10V, 20V, and 30V are 140 kPa, 280 kPa, and 420 kPa, respectively. Likewise, for the Parylene-C/Graphene CMUT with AC voltages of 10V, 20V, and 30V their respective peak output pressures over the membrane surface are 160 kPa, 320 kPa, and 478 kPa. All of these AC voltages represent an increase of 14% for the Parylene-C/Graphene CMUT cell.

Although the results above are primarily concerned with the pressure generated over the surface of the membrane, there exists a need to know how much the pressure amplitude will be once the wave leaves the membrane surface and travels into the medium. This pressure will eventually be the ultrasound wave that comes into contact with the surrounding ultrasound waves from the other cells to ultimately form a combined pressure wave. For that type of analysis, a 2D visual plot of the pressure field is created for a single axial symmetric CMUT cell operating in a vegetable oil environment. Both CMUT cells were biased at 60% of their respective collapse voltages, and their maximum possible AC voltages before collapse were applied. The frequency of interest was 7.1 MHz, as this was the frequency at which it was observed that maximum efficiency between electrical voltage bias and acoustic took place.
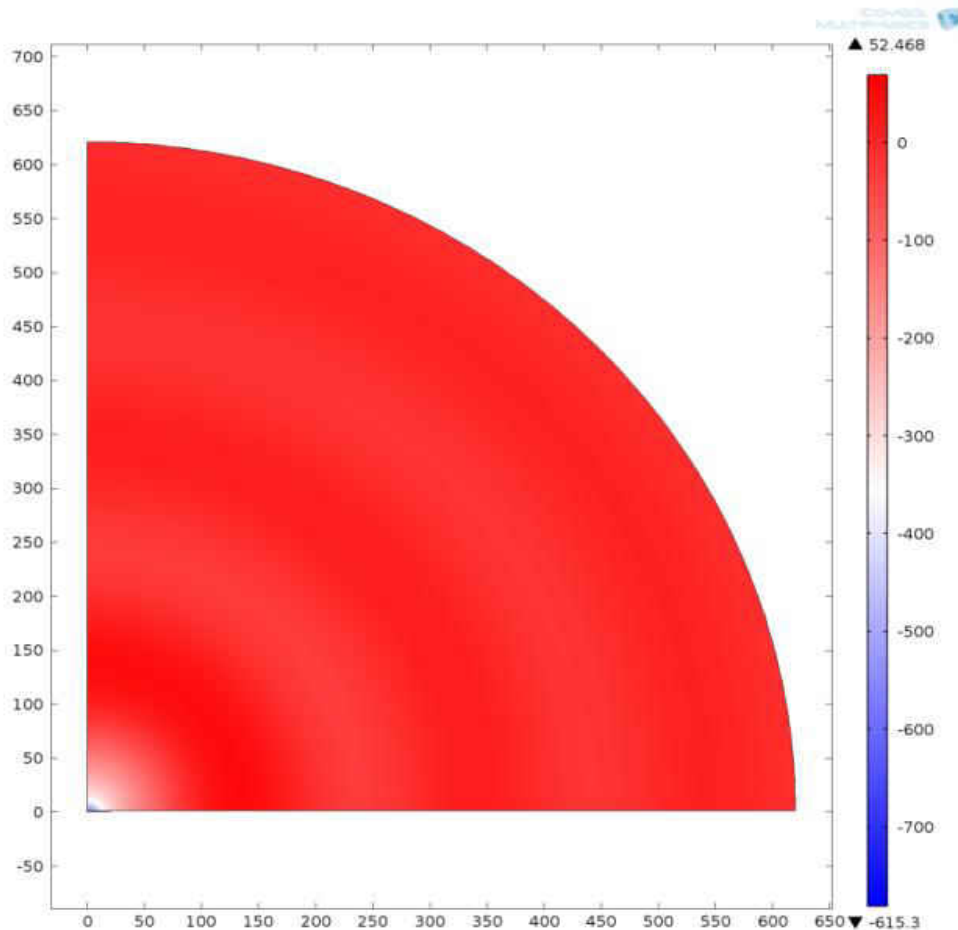
Figure 63: Silicon/SiO$_2$ transducer time-harmonic peak pressure output into the vegetable oil medium from a single source CMUT transducer. The pressure field is examined at a transducer center frequency of 7.1 MHz, as this was the designed frequency for the structure and exhibits the highest electrical-acoustic efficiency.

Figure 63 above illustrates the 2D plot of the peak pressure amplitude for the

Silicon/SiO$_2$ CMUT membrane. The CMUT cell is located at the (0,0) μm position on the plot,

and is primary source of the ultrasound wave being generated. The maximum wave amplitude

of the ultrasound that is generated into the vegetable oil medium is about 52 kPa.
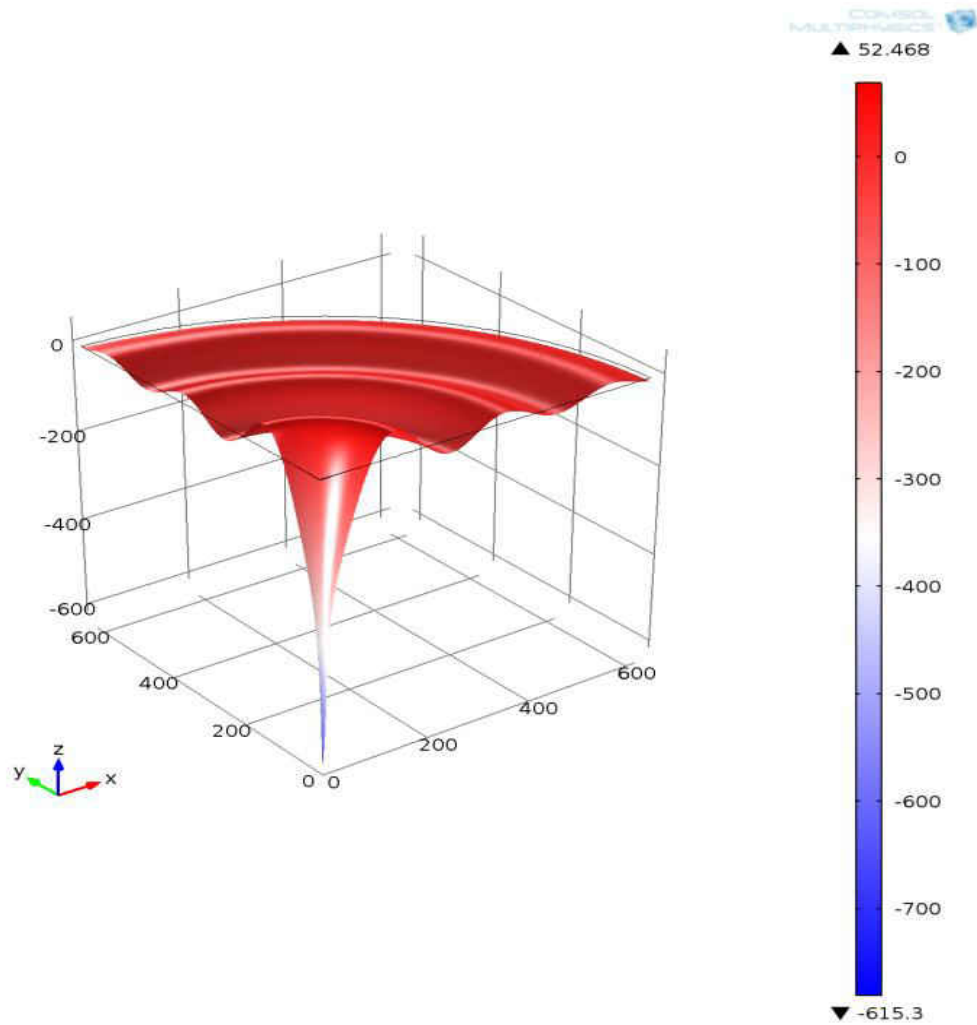
Figure 64: Silicon/SiO$_2$ 3D plot of the 2D surface plot from Figure 63. The relative differences between the pressure over the membrane (~615 kPa) and the pressure amplitude of the resulting wave into the vegetable oil medium (52 kPa) can be visualized.

Figure 64 above shows a 3D height plot for the same results as shown in Figure 63. In this 3D view, the relative size of the difference between the pressure output at the transducer face and the pressure amplitude that eventually radiates into the medium can be seen.
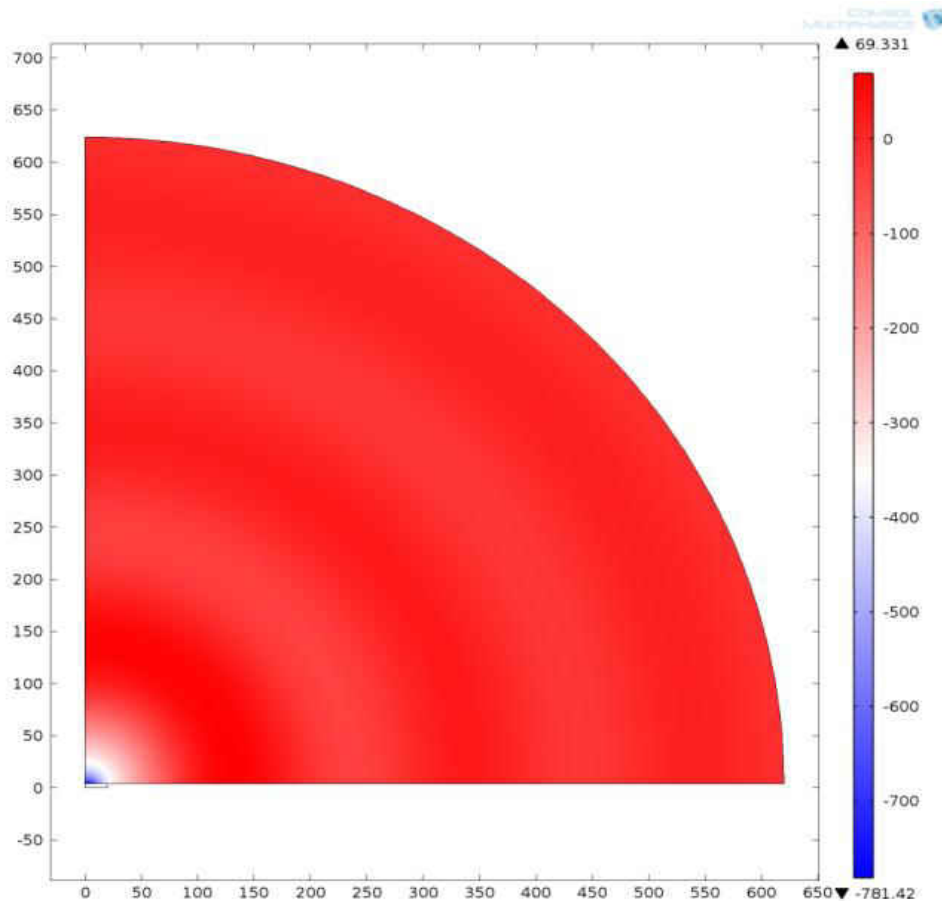
Figure 65: Parylene-C/Graphene transducer time-harmonic peak pressure output into the vegetable oil medium from a single source CMUT transducer. The pressure field is examined at a transducer center frequency of 7.1 MHz, as this was the designed frequency for the structure and exhibits the highest electrical-acoustic efficiency.

Figure 65 above illustrates the same 2D plot of the peak pressure amplitude as shown in Figure 63 above, however this plot is for the Parylene-C/Graphene CMUT membrane. The maximum wave amplitude of the ultrasound that is generated into the vegetable oil medium by this design is approximately 70 kPa. This shows an increase of 35% for the Parylene-C/Graphene CMUT when compared to the Silicon/SiO$_2$ CMUT membrane.
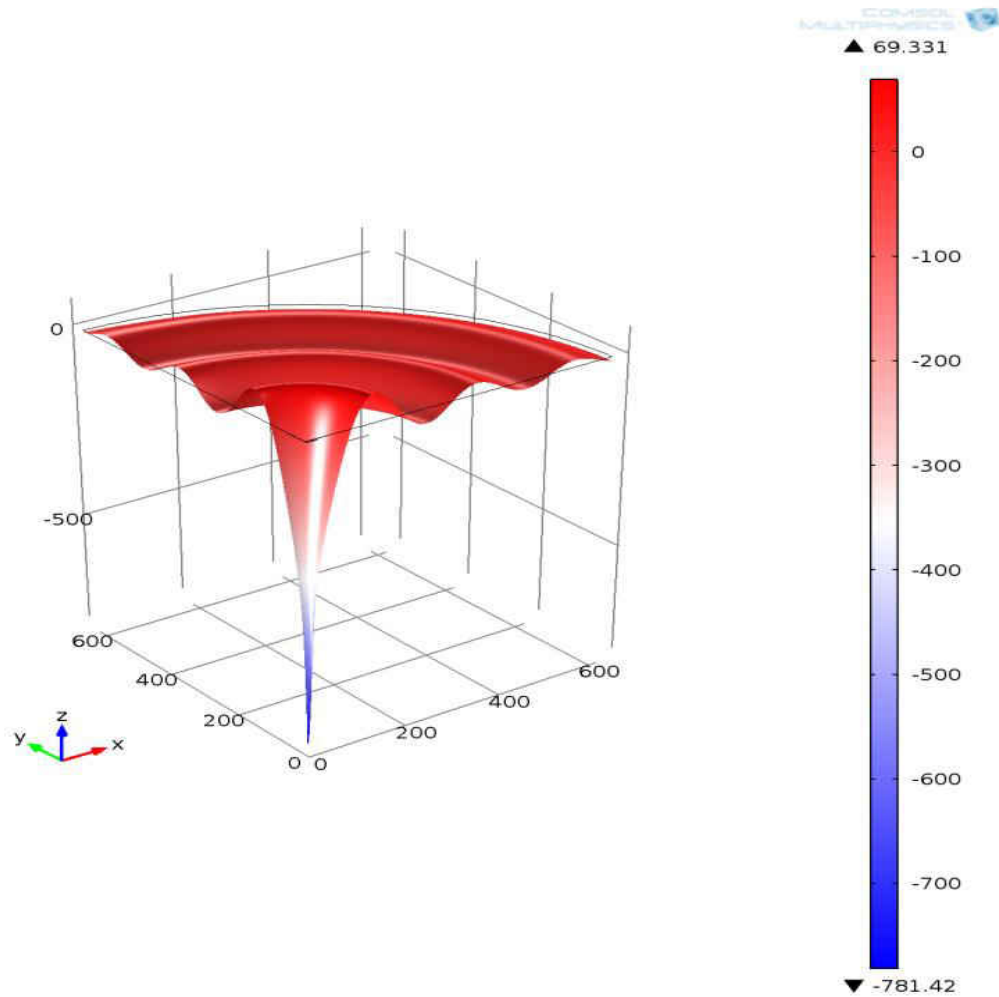
Figure 66: Parylene-C/Graphene 3D plot of the 2D surface plot from Figure 65. The relative differences between the pressure over the membrane (~615 kPa) and the pressure amplitude of the resulting wave into the vegetable oil medium (52 kPa) can be visualized.

Figure 66 above again shows a 3D height plot for the same results as shown in Figure 64.

In this 3D view, the relative size of the difference between the pressure output at the

100

transducer face and the pressure amplitude that eventually radiates into the vegetable oil

medium is illustrated for a Parylene-C/Graphene CMUT.

CHAPTER SIX:
CONCLUSION

A less expensive and slightly higher performing capacitive micromachined ultrasonic transducer has been proposed. This MEMS CMUT polymer-based device aims to reduce the current costs associated with commercial PZT ceramic-based ultrasound transducers, while at the same time improving upon the design of current CMUTs by increasing the transmission of pressure output from the individual cells. To characterize the CMUT performance, finite element analysis (FEA) was used by constructing an axial symmetric model in COMSOL Multiphysics. This cell considered the membrane material as well as the effects of fluid damping. The physics domains necessary to characterize the CMUT include: Pressure Acoustics, MEMS Solid Mechanics, Moving Mesh, and Electrostatics.

The goal of the simulation was to study the output pressure transmission of the silicon-based membrane and the Parylene-C/Graphene membrane. In order to conduct a fair comparison, a few parameters must be held constant. Normally the overall goal of current CMUT research is to increase pressure output and to a lesser extent to increase sensitivity to an incoming pressure wave. Thus, the diameters of the cell membranes were held constant for this study.

Both CMUT cells were tailored to have a center structural frequency of 7.1 MHz in oil, while the gap height was modeled as being vacuum sealed. To reduce collapse voltage while simultaneously providing more gap height for membrane motion, both membranes were suspended at 0.25 μm from the bottom surface. After a fair comparison was ensured, the models were statically deflected with an input voltage to study the membrane deflection profile. The Parylene-C/Graphene CMUT exhibited more deflection at the post than the silicon-based CMUT. This was because the post material was also a flexible polymer parylene-C material.

Volume displacement of the membrane was also confirmed to be higher in the Parylene-C/Graphene CMUT, as suspected from the membrane deflection profile. The Parylene-based membrane exhibited a volume displacement of 45 μm^3, which was a 50% increase from the silicon-based CMUT displacement of 30 μm^3.

It was further determined that the higher volume displacement of the Parylene-C/Graphene CMUT also translated to a higher peak pressure output over the membrane surface, a higher pressure amplitude of the CMUT generated sound wave into the medium, and a higher sensitivity due to an incoming wave. The Parylene-C/Graphene model exhibited a maximum peak pressure transmission output of 820 kPa over the membrane surface, while a similar characterization performed on Silicon/SiO_2 CMUT cells yielded 615 kPa. This shows a 30% increase in output pressure. Likewise, the generated ultrasound pressure amplitude into the surrounding oil medium was approximately 70 kPa for the parylene-based CMUT and 52

kPa for the silicon-based CMUT. This shows an increase of 35% for pressure amplitude. The sensitivity, although not nearly as effected by the ability of the parylene post to deflect as the transmission output is, still shows a 5% increase in sensitivity to an incoming pressure wave.

The next step for work on the CMUT includes microelectronic fabrication of the cells, along with full characterization to verify the Parylene-C/Graphene numerical simulation model against the actual device. An ultrasound probe consisting of these Parylene-C/Graphene cells is to be constructed and tested on an ultrasound medical imaging system against the current PZT transducer.

The future work for this device includes fabrication of 2D cells for 3D imaging. This will include fabricating the CMUT cells directly on top of the analog front end integrated circuits, and designing the hardware necessary to process the array's signals into a 3D ultrasound image.

LIST OF REFERENCES

1.   Ergun, A.S., et al. *A new detection method for capacitive micromachined ultrasonic transducers*. in *Ultrasonics Symposium, 1998. Proceedings., 1998 IEEE*. 1998.

2.   Hansen, S., et al. *Defect imaging by micromachined ultrasonic air transducers*. in *Ultrasonics Symposium, 1998. Proceedings., 1998 IEEE*. 1998.

3.   Mills, D.M. *Medical imaging with capacitive micromachined ultrasound transducer (cMUT) arrays*. in *Ultrasonics Symposium, 2004 IEEE*. 2004.

4.   Wygant, I.O., et al., *Integration of 2D CMUT arrays with front-end electronics for volumetric ultrasound imaging.* Ultrasonics, Ferroelectrics and Frequency Control, IEEE Transactions on, 2008. **55**(2): p. 327-342.

5.   Smith, S.W., H.G. Pavy, Jr., and O.T. von Ramm, *High-speed ultrasound volumetric imaging system. I. Transducer design and beam steering.* Ultrasonics, Ferroelectrics and Frequency Control, IEEE Transactions on, 1991. **38**(2): p. 100-108.

6.   Turnbull, D.H. and F.S. Foster, *Beam steering with pulsed two-dimensional transducer arrays.* Ultrasonics, Ferroelectrics and Frequency Control, IEEE Transactions on, 1991. **38**(4): p. 320-333.

7.   Xuefeng, Z., et al., *Fabrication of Flexible Transducer Arrays With Through-Wafer Electrical Interconnects Based on Trench Refilling With PDMS.* Microelectromechanical Systems, Journal of, 2008. **17**(2): p. 446-452.

8. Noble, R.A., et al. *Low-temperature micromachined cMUTs with fully-integrated analogue front-end electronics*. in *Ultrasonics Symposium, 2002. Proceedings. 2002 IEEE*. 2002.

9. Mills, D.M. and L.S. Smith. *Real-time in-vivo imaging with capacitive micromachined ultrasound transducer (cMUT) linear arrays*. in *Ultrasonics, 2003 IEEE Symposium on*. 2003.

10. Bayram, B., et al., *A new regime for operating capacitive micromachined ultrasonic transducers.* Ultrasonics, Ferroelectrics and Frequency Control, IEEE Transactions on, 2003. **50**(9): p. 1184-1190.

11. Guldiken, R.O., J. McLean, and F.L. Degertekin, *CMUTS with dual electrode structure for improved transmit and receive performance.* Ultrasonics, Ferroelectrics and Frequency Control, IEEE Transactions on, 2006. **53**(2): p. 483-491.

12. Chiou, D.Y., et al., *Characterization and optimization design of the polymer-based capacitive micro-arrayed ultrasonic transducer.* Japanese Journal of Applied Physics Part 1-Regular Papers Brief Communications & Review Papers, 2007. **46**(11): p. 7496-7503.

13. Zhuang, X. and et al., *Biocompatible coatings for CMUTs in a harsh, aqueous environment.* Journal of Micromechanics and Microengineering, 2007. **17**(5): p. 994.

14. Bushong, S.C. and B.R. Archer, *Diagnostic ultrasound : physics, biology, and instrumentation / Stewart C. Bushong, Benjamin R. Archer*1991, St. Louis: Mosby Year Book.

15. Wikipedia, *Ultrasound*. Available from: http://en.wikipedia.org/wiki/Ultrasound.

16.   Evans, D.H.P.D. and W.N. McDicken, *Doppler ultrasound : physics, instrumentation and signal processing / David H. Evans and W. Norman McDicken*. 2nd ed. ed2000, Chichester ; New York: John Wiley.

17.   Zagzebski, J.A., *Essentials of ultrasound physics / James A. Zagzebski*1996, St. Louis: Mosby.

18.   Szabó, T., *Diagnostic ultrasound imaging inside out*2004, Amsterdam: Elsevier Academic.

19.   Inc., B.P.-O., *An introduction to Piezoelectric Transducer Crystals.*

20.   ndt-ed.org, *Characteristics of Piezoelectric Transducers.*

21.   Galassi, C., et al., *Piezoelectric materials : advances in science, technology, and applications / edited by Carmen Galassi ... [et al.]*. NATO science series. Series 3, High technology ; vol. 762000, Dordrecht ; Boston: Kluwer Academic Publishers.

22.   Hoskins, P.R., *Diagnostic ultrasound : physics and equipment / Peter Hoskins ... [et al.]*2003, London: GMM.

23.   Sprawls, P., *Ultrasound Production and Interactions.*

24.   Brunke, S.S. and G.R. Lockwood, *Broad-bandwidth radiation patterns of sparse two-dimensional vernier arrays.* Ultrasonics, Ferroelectrics and Frequency Control, IEEE Transactions on, 1997. **44**(5): p. 1101-1109.

25.   Rose, J.L. and B.B.j.a. Goldberg, *Basic physics in diagnostic ultrasound / Joseph L. Rose, Barry B. Goldberg*. A Wiley medical publication1979, New York: Wiley.

26.   Korvink, J.G. and O. Paul, *MEMS : a practical guide to design, analysis, and applications / edited by Jan G. Korvink and Oliver Paul*2006, Norwich, NY : Heidelberg, Germany: W. Andrew Pub. ; Springer.

27.   Ganji, B.A. and B.Y. Majlis. *Slotted capacitive microphone with sputtered aluminum diaphragm and photoresist sacrificial layer*. in *Semiconductor Electronics (ICSE), 2010 IEEE International Conference on*. 2010.

28.   Palasagaram, J.N. and R. Ramadoss. *MEMS capacitive pressure sensor array fabricated using printed circuit processing techniques*. in *Industrial Electronics Society, 2005. IECON 2005. 31st Annual Conference of IEEE*. 2005.

29.   Kim, S., et al. *Ultrasonic electrostatic actuators on a flexible substrate*. in *Micro Electro Mechanical Systems (MEMS), 2012 IEEE 25th International Conference on*. 2012.

30.   Chih-Hsiang, K., I.L. Chiung, and H. Tsun-Che. *RF characteristics of dual-actuation CMOS-MEMS RF switches*. in *Electronic Components and Technology Conference, 2009. ECTC 2009. 59th*. 2009.

31.   Lastochkin, D., et al., *Electrokinetic micropump and micromixer design based on <equation>ac</equation> faradaic polarization.* Journal of Applied Physics, 2004. **96**(3): p. 1730-1733.

32.   Younis, M.I., *MEMS linear and nonlinear statics and dynamics [electronic resource] / Mohammad I. Younis*. Microsystems.2011, New York ; London: Springer.

33.   Jonassen, N., *Electrostatics / Niels Jonassen*1998, New York: Chapman & Hall.

34. Hsu, T.R., *MEMS and microsystems : design, manufacture, and nanoscale engineering / Tai-Ran Hsu*. 2nd ed. ed2008, Hoboken, N.J: John Wiley.

35. Ahmad, B. and R. Pratap, *Elasto-Electrostatic Analysis of Circular Microplates Used in Capacitive Micromachined Ultrasonic Transducers.* Ieee Sensors Journal, 2010. **10**(11): p. 1767-1773.

36. Oralkan, O.a.M.K., *Brief History of CMUTs.*

37. Cantrell, J.H., et al., *Broadband electrostatic acoustic transducer for ultrasonic measurements in liquids.* Review of Scientific Instruments, 1979. **50**(1): p. 31-33.

38. Hunt, F.V., *Electroacoustics; the analysis of transduction, and its historical background*1954, Cambridge: Harvard University Press.

39. Wygant, I.O., M. Kupnik, and B.T. Khuri-Yakub. *Analytically calculating membrane displacement and the equivalent circuit model of a circular CMUT cell*. in *Ultrasonics Symposium, 2008. IUS 2008. IEEE*. 2008.

40. Martinussen, H., et al., *CMUT characterization by interferometric and electric measurements.* Ultrasonics, Ferroelectrics and Frequency Control, IEEE Transactions on, 2009. **56**(12): p. 2711-2721.

41. Demirci, U., et al. *Capacitive micromachined ultrasonic transducer arrays for medical imaging: experimental results*. in *Ultrasonics Symposium, 2001 IEEE*. 2001.

42. Yeh, D.T., et al., *3-D ultrasound imaging using a forward-looking CMUT ring array for intravascular/intracardiac applications.* Ultrasonics, Ferroelectrics and Frequency Control, IEEE Transactions on, 2006. **53**(6): p. 1202-1211.

43.   Oralkan, O., et al. *High-frequency CMUT arrays for high-resolution medical imaging*. in *Ultrasonics Symposium, 2004 IEEE*. 2004.

44.   Zahorian, J., et al., *Monolithic CMUT-on-CMOS integration for intravascular ultrasound applications.* Ultrasonics, Ferroelectrics and Frequency Control, IEEE Transactions on, 2011. **58**(12): p. 2659-2667.

45.   Lohfink, A., et al. *Derivation of a 1D CMUT model from FEM results for linear and nonlinear equivalent circuit simulation*. in *Ultrasonics, 2003 IEEE Symposium on*. 2003.

46.   Gurun, G., P. Hasler, and F.L. Degertekin, *Front-end receiver electronics for high-frequency monolithic CMUT-on-CMOS imaging arrays.* Ultrasonics, Ferroelectrics and Frequency Control, IEEE Transactions on, 2011. **58**(8): p. 1658-1668.

47.   Cicek, I., A. Bozkurt, and M. Karaman, *Design of a front-end integrated circuit for 3D acoustic imaging using 2D CMUT arrays.* Ultrasonics, Ferroelectrics and Frequency Control, IEEE Transactions on, 2005. **52**(12): p. 2235-2241.

48.   Ergun, A.S., et al. *Broadband capacitive micromachined ultrasonic transducers ranging from 10 kHz to 60 MHz for imaging arrays and more*. in *Ultrasonics Symposium, 2002. Proceedings. 2002 IEEE*. 2002.

49.   Ahrens, O., et al., *Fabrication of gap-optimized CMUT.* Ultrasonics, Ferroelectrics and Frequency Control, IEEE Transactions on, 2002. **49**(9): p. 1321-1329.

50.   Bayram, C., et al. *Bandwidth improvement in a cMUT array with mixed sized elements*. in *Ultrasonics Symposium, 2005 IEEE*. 2005.

51.   Bayram, B., et al. *Dynamic analysis of CMUTs in different regimes of operation*. in *Ultrasonics, 2003 IEEE Symposium on*. 2003.

52.   Bayram, B., et al. *Dynamic FEM analysis of multiple cMUT cells in immersion [capacitive micromachined ultrasonic transducers]*. in *Ultrasonics Symposium, 2004 IEEE*. 2004.

53.   Park, K.K., et al. *Optimum design of circular CMUT membranes for high quality factor in air*. in *Ultrasonics Symposium, 2008. IUS 2008. IEEE*. 2008.

54.   Bayram, B., et al., *Capacitive micromachined ultrasonic transducer design for high power transmission.* Ultrasonics, Ferroelectrics and Frequency Control, IEEE Transactions on, 2005. **52**(2): p. 326-339.

55.   Oralkan, O., et al., *Experimental characterization of collapse-mode CMUT operation.* Ultrasonics, Ferroelectrics and Frequency Control, IEEE Transactions on, 2006. **53**(8): p. 1513-1523.

56.   Yongli, H., et al., *Comparison of conventional and collapsed region operation of capacitive micromachined ultrasonic transducers.* Ultrasonics, Ferroelectrics and Frequency Control, IEEE Transactions on, 2006. **53**(10): p. 1918-1933.

57.   Ching-Hsiang, C., et al. *A flexible capacitive micromachined ultrasonic transducer (CMUT) array with increased effective capacitance from concave bottom electrodes for ultrasonic imaging applications*. in *Ultrasonics Symposium (IUS), 2009 IEEE International*. 2009.

58.   Ming-Wei Chang, M., et al. *Polymer-based Capacitive Micromachined Ultrasonic Transducers (CMUT) for Micro Surgical Imaging Applications*. in *Nano/Micro Engineered and Molecular Systems, 2006. NEMS '06. 1st IEEE International Conference on*. 2006.

59.   Chiou, D.Y., et al., *Finite element modeling, characterization, and optimization design for the polymer-typed capacitive micro-arrayed ultrasonic transducer.* Microsystem Technologies-Micro-and Nanosystems-Information Storage and Processing Systems, 2008. **14**(6): p. 787-797.

60.   Ming-Wei, C., et al. *6F-6 A Novel Method for Fabricating Sonic Paper*. in *Ultrasonics Symposium, 2007. IEEE*. 2007.

61.   Chen, P.J., et al. *Implantable Unpowered Parylene MEMS Intraocular Pressure Sensor*. in *Microtechnologies in Medicine and Biology, 2006 International Conference on*. 2006.

62.   Xunjun, H., et al. *A laterally driven capacitive RF MEMS switch using parylene as dielectric layer*. in *Sensors, 2010 IEEE*. 2010.

63.   Po-Ying, L., et al., *A Parylene MEMS Electrothermal Valve.* Microelectromechanical Systems, Journal of, 2009. **18**(6): p. 1184-1197.

64.   Zhifang, F., et al., *Parylene surface-micromachined membranes for sensor applications.* Microelectromechanical Systems, Journal of, 2004. **13**(3): p. 484-490.

65.   Coating, C., *What is Parylene?*

66.   Chen, M.-H., Y.-J. Chuang, and F.-G. Tseng, *Self-masked high-aspect-ratio polymer nanopillars.* Nanotechnology, 2008. **19**(50): p. 505301.

67.   Kim, K.S., et al., *Large-scale pattern growth of graphene films for stretchable transparent electrodes.* Nature, 2009. **457**(7230): p. 706-710.

68.   Kaltenbacher, M., *Numerical simulation of mechatronic sensors and actuators / Manfred Kaltenbacher*2004, Berlin ; New York: Springer.

69.   Koymen, H., et al., *Parametric linear modeling of circular cMUT membranes in vacuum.* Ultrasonics, Ferroelectrics and Frequency Control, IEEE Transactions on, 2007. **54**(6): p. 1229-1239.

70.   Ronnekleiv, A., *CMUT array modeling through free acoustic CMUT modes and analysis of the fluid CMUT interface through Fourier transform methods.* Ultrasonics, Ferroelectrics and Frequency Control, IEEE Transactions on, 2005. **52**(12): p. 2173-2184.

71.   Yongli, H., et al. *Capacitive micromachined ultrasonic transducers (cmuts) with piston-shaped membranes.* in *Ultrasonics Symposium, 2005 IEEE*. 2005.

72.   Timoshenko, S., *Theory of plates and shells, by S. Timoshenko*. 1st ed. ed. Engineering Special Collection1940, New York, London: McGraw-Hill Book Company, inc.

73.   Benson, D.J. and M. Souli, *Arbitrary Lagrangian-Eulerian and fluid-structure interaction : numerical simulation / edited by Mhamed Souli, David J. Benson*2010, London : Hoboken, NJ: ISTE ; Wiley.